ANTINEUTRINO DETECTION AND NEUTRON DIRECTIONALITY STUDIES WITH THE miniTIMECUBE, THE WORLD'S SMALLEST NEUTRINO DETECTOR

A THESIS SUBMITTED TO THE GRADUATE DIVISION OF THE UNIVERSITY OF HAWAII AT MANOA IN PARTIAL FULFILLMENT OF THE REQUIREMENTS FOR THE DEGREE OF

DOCTORATE OF PHILOSOPHY

IN

PHYSICS

April 26, 2018

By

John Koblanski

Dissertation Committee:

Dr. John G. Learned, Chair Person

Dr. Veronica Bindi

Dr. Jason Kumar

Dr. Sven Vahsen

Dr. George Wilkens

Dedicated to my father

Acknowledgements

Firstly I would like to acknowledge my father who sadly passed away during the final stretch of my studies. His love and wisdom helped shape the man I have become. He was persistent that I finish my studies and do something different with my life and stop being a (fill in the blank..) stock broker! I am very pleased with my decision to listen to him, perhaps I always was listening in my own slow and stubborn round about way. I am sure he would be very proud right now.

I would like to thank my supervisor Dr. John Learned for sharing his deep wealth of physics knowledge and his general wisdom about how to deal with life. I don't think I could have found a better opportunity to gain experience on so many different aspects of project development as I did under his guidance. You are definitely a cool cat John! I would like to thank my committee for being there for me under many last minute arrangements. I would also like to thank my surrounding team of graduate students who did some incredible work with so few hands. The team in no particular order is:

UH Manoa: R. Dorrill, M.J. Duvall, J. Koblanski, J.G. Learned, V.A. Li,

L. Macchiarulo, S. Matsuno, J. Murillo, S. Negrashov, M. Rosen, M. Sakai, G.S. Varner, A.Druetzl

University of Maryland: W.F. McDonough, K. Engel, S.A. Wipperfurth

Ultralytics: G. Jocher, K. Nishimura

NGA: S.M. Usman

NIST: H.P. Mumm

Some special thanks as well to Serge Negrashov who assisted me with my challenges with the electronic hardware I was assigned to build, to Kurtis Nishimura who was always able to give good advice on just about any problem, and Glenn Jocher from who I learned much about analysis and programming techniques. And I would like to thank my partner Maja Pilgaard Schjervheim for being amazing, supportive, and adventurous. Thanks for not getting sick of me I am not quite sure how you do it. Special love to my unique and amazing family, we would be nowhere without each other!

I would also like to thank the University of Hawaii at Manoa physics department for taking a chance on me, teaching me so much, and whisking a Canadian from the cold and dropping him into paradise. It's all been lovely thank you!

Abstract

With neutrino detectors continuously becoming larger and more expensive every day it is vital that the next generation of scientists work against this tide to make smaller and smarter neutrino detectors where it is possible. Of course ultimately long distance neutrino detection requires large instruments, but near reactor detectors can be small and prove out techniques for later larger applications. In this spirit we present to you the miniTimeCube (mTC), a prototype for a small compact portable antineutrino detector with directional capability. While we did not achieve everything we had hoped on our first attempt, our group has a set a precedent in the field of a dozen competitors. We present a unique model for fitting neutron directionality which produces an agreement between the average truth and fitted directional vector of $cos(\theta) = .998$ +/-.002, an impressive result considering neutron directionality has never been achieved in a single hard volume target. We will discuss the detector construction, our simulations and reconstructions, our results from our neutrino experiment at the test reactor at NIST, and our neutron directionality test here at the University of Hawaii at Manoa.

Contents

List of Figures

List of Tables

Chapter 1

All About The Neutron

It is advantageous to explore some fundamental particle physics first, in particular that which pertains to neutrons and neutrinos (their properties and their historical discovery). I believe an early introduction will enrich the reader's appreciation for the particle experiments of the past, present and future. This introductory chapter discusses the discovery of the neutron, its current properties as we understand them within the standard model, and the historical experiments that led the way.

1.1 Discovery of the Neutron

In 1911, Earnest Rutherford theorized that the nucleus consisted of an electron cloud surrounding a dense pack of protons [1]. However, it was understood shortly after that electrons were being emitted from the nucleus

through beta radiation. This propelled Earnest Rutherford to rethink his initial proposition. In 1920, he proposed that the nucleus also contained neutral particles which consisted of electrons that were tightly bound to protons [10]. This is considered to be the first time the concept of the neutron has ever been proposed. There are problems with this theory however. For instance, if electrons inhabited the nucleus then we could calculate their typical energies using the Heisenberg Uncertainty Principle [11]. If we take the radius of the nucleus to be $\Delta x = 10^{-15}$ m, then:

$$\begin{aligned} \Delta p &= \frac{\hbar}{2\pi\Delta x} \\ &= 1.05 * 10^{-19} \text{ kgm/s} \end{aligned}$$

And then using the relativistic energy equation we get:

$$\begin{aligned} E &= \sqrt{m^2c^4 + p^2c^2} \\ &= 223 \text{ MeV} \end{aligned}$$

This is much greater than the typical beta decay energies which are less than 1MeV as seen in figure 1.3.

In 1932, James Chadwick discovered the neutron and published his findings in the paper he called "Possible Existence of a Neutron" [12]. He had been inspired by recent experiments with alpha radiation. In 1930, Herbert Becker and Walther Wilhelm George Bothe performed a scattering

experiment in which beryllium was bombarded with alpha particles from the radioactive source polonium and a neutral radiation was produced [13]. Their assumption at the time was that the radiation was gamma rays. Then Irene and Frederic Joliot-Curie showed that when you exposed a paraffin target with this same radiation, protons were ejected with energy about 5.3 MeV [14]. This was inconsistent with relativistic kinematics, as can be shown from a simple momentum and energy analysis which yields an energy for the gamma rays much greater than what is seen in emitted particles from the nucleus.

Chadwick along with Rutherford had decided then that the gamma rays could not be energetic enough to cause the protons to be ejected at 5.3MeV. Chadwick set up an experiment that was nearly identical to Curie and Joliot's and is shown in figure 1.1. A polonium source was used to bombard a beryllium target which then emits neutrons that strike the paraffin target. The paraffin target then emits protons that are counted with a Geiger counter. He found that the neutral particle had to be massive and determined its mass by colliding the neutrons with boron which had a known mass. Using conservation of energy he was able to set up an equation for the mass of the neutron:

$$\frac{1}{2}m_\alpha v_\alpha^2 + m_\alpha c^2 + m_B c^2 = \frac{1}{2}m_N v_N^2 + m_N c^2 + \frac{1}{2}m_n v_n^2 + m_n c^2 \qquad (1.1)$$

where B, N, n, and α, stands for the boron, nitrogen, neutron, and alpha particle respectively. The only unknowns in the equation were the velocity and the mass of the neutron (v_n and m_n respectively) for which Chadwick made an intelligent guess. He assumed that the neutron and proton had roughly equal mass and preformed collision experiments of the neutral particles with hydrogen and used the resultant proton velocity in equation 1.1. He determined the mass of the neutron to be 938. MeV/c^2 +/ − 1.38 MeV/c^2 which is quite impressive given that our current estimate of the neutrons mass is $m_{neutron} = 939.56563(28)$ MeV/c^2 [15].

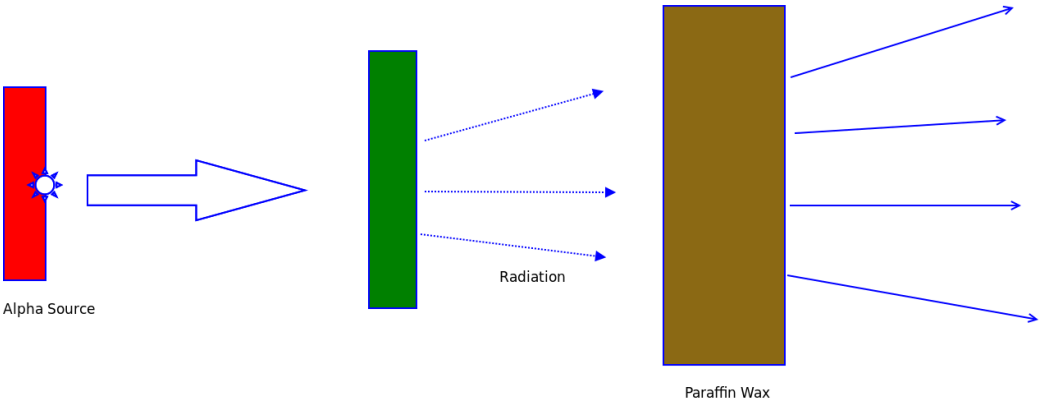

Figure 1.1: Diagram of Chadwick's experiment where polonium source was used to bombard a beryllium target which in turn emits radiation (neutrons) that strike the paraffin target which then emits protons. The protons are counted with a Geiger counter.

The discovery of the neutron ushered in a new era of physics. Many

models were subsequently proposed to describe the nucleus. Fermi had experimented with bombarding neutrons against heavy isotopes which produced new radioactive elements. Fermi (1938) received the Nobel Prize in Physics "for his demonstrations of the existence of new radioactive elements produced by neutron irradiation, and for his related discovery of nuclear reactions brought about by slow neutrons" [16] in 1938. Nuclear fission led the utilization of nuclear power and ultimately led to the development of the atomic bomb.

1.2 The Structure and Properties of the Neutron

The mass of the neutron can be determined in a variety of ways. One can examine beta decay (to be discussed in section 1.3) and deduce the momenta of the outgoing proton and electron. Or one can use mass spectrometry (not directly as the neutron has no charge) on deuterium as we know its mass as well as that of the proton.

While the neutron has no electric charge, it has a magnetic moment. In 1940 Luis Alvarez and Felix Bloch determined the magnetic moment of the neutron to be $\mu_n = 1.93(2)\mu_N$ [17], where μ_N is the magnetic magneton. The magnetic moment arises from the internal structure of the neutron which consists of a bound state of one up quark (charge +2/3 e) and two down quarks

(together make a charge of -2/3 e) [3]. A simple model can be made to account for the magnetic moment by treating the quarks as point-like particles and adding their individual intrinsic and orbital moments vectorially. However this model is too simple and a real treatment must incorporate relativity.

In 1964 Mirza A. B. Beg, Benjamin W. Lee, and Abraham Pais attempted to calculate the ratio of proton to neutron magnetic moments. They theoretically calculated the ratio to be $-3/2$ using early group theory principles and exploiting the similarities in structure of the neutron and proton [18]. The ratio is in fact 1.45989806(34) [19] and so there was approximately a 3% discrepancy. By and large this was considered a success for the standard model, however, a proper calculation from first principles is still ongoing. While various attempts have been successful, none have employed the proper mass of the quark which is much less than one third of the nucleon. The complications arise in the fact that most of the mass is tied up in the fields of the strong force.

The neutron is a spin 1/2 particle and as such it is a fermion with intrinsic angular momentum $\frac{1}{2}\hbar$ [3]. In 1949, Hughes and Burgy measured the angular distribution of the reflections of neutrons from a ferromagnetic mirror to be consistent with spin 1/2 [20]. In 1954, Sherwood, Stephenson, and Bernstein used a SternGerlach experiment with neutrons to separate the neutron spin states and also found them to be consistent with spin 1/2 [21].

The fact that the neutrons are spin 1/2 particles and thus obey the Pauli Exclusion Principle, allows for neutron stars to exist via degeneracy pressure.

Protons overcome their mutual electrical repulsion in a nucleus via the addition of neutrons. In fact the electrical repulsion between protons is stronger than the attractive strong force between them and thus any nucleus with greater than one proton must incorporate neutrons to be stable. A plot of the stability of nuclei is given in figure 1.2. The stable nuclei are shown in green while the unstable radionuclides are plotted in beige. A radionuclide tends to undergo fission, in which the nucleus fragments into smaller daughter nuclei, releasing energy and allowing for a higher energy per nucleon bond to be formed in the daughter nuclei. We see that for smaller nuclei stability is achieved with $N = Z$ where Z is the number of protons and N is the number of neutrons. For heavier nuclei, their stability tends towards a $N > Z$ profile. In 2007 an interesting article was published which added another dimension to attractive mechanism between these particles [22]. The article investigates the charge densities of the neutron and proton and finds that there is actually a charge distribution in the neutron that corresponds to a negative core, a positive middle region and an outer shell that is negative. This structure aids in the bonding between the two nucleons by way of a Van der Waals force.

While an electric dipole moment has actually never been measured in a

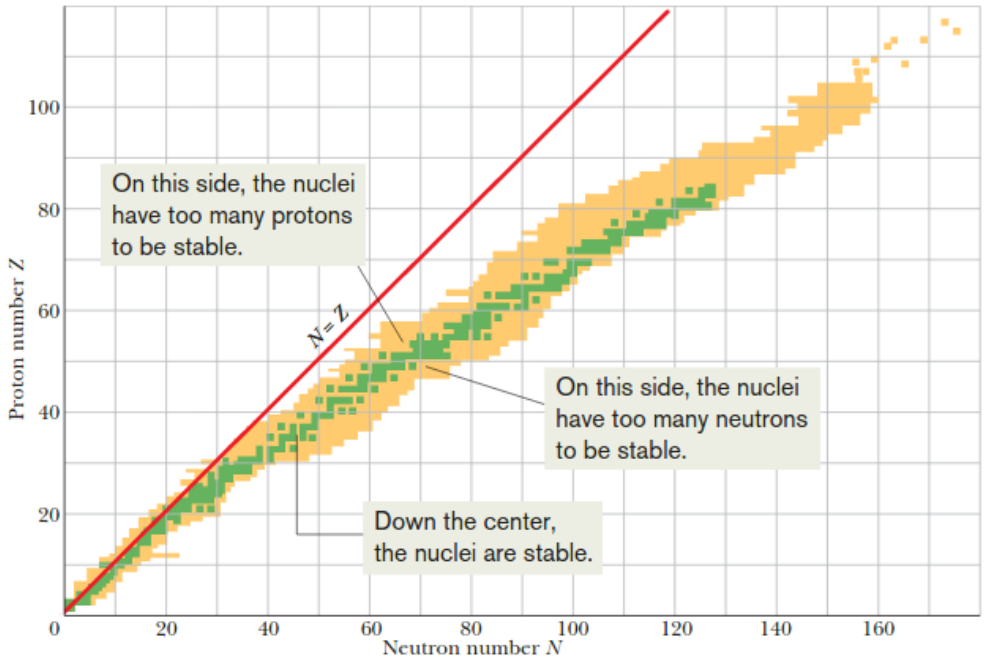

Figure 1.2: Here is a plot of the proton number Z vs the neutron number N for the known nuclei. The green shaded area shows the stable nuclides. We see that for smaller nuclei, stability is achieved with $N = Z$ where N is the number of protons and Z is the number of neutrons. Plot taken from [1]

lab, the standard model predicts that there should be a very small one that is beyond our ability at measure at this time [23]. There are currently multiple experiments trying to measure the neutron electric dipole moment.

1.3 Beta Decay

Under the Standard Model neutrons can only decay via the weak interaction where a heavier down quark is converted to a lighter down quark via the

emission of a W boson. The weak force is characterized by its long decay times and its mechanism for particles to exchange a W or a Z boson. A proton cannot spontaneously decay as it is the lightest baryon and so we would have a violation of the conservation of baryon number. Grand unification theories however indicates that the proton should have a half-life of about 10^{32} years (depending on the particular theory) although such time scales are difficult to examine experimentally and no such evidence of proton decay has thus far presented itself.

The free neutron has a mean lifetime of $881.5 \pm 1.5s$ and a half life of $611.0 \pm 1.0s$ [24]. However inside the nucleus the neutron is stable. Beta Decay involves the conversion of the neutron into a proton, an electron and an antineutrino as shown in figure 1.3. This Feynman diagram illustrates how the intermediate vector boson W is the principle player in the exchange process of converting a down quark into an up quark.

Beta decay has a sharp definitive energy signature which does not vary, however the kinetic energy provided by the disintegration energy:

$$Q = \Delta mc^2 \tag{1.2}$$

is divided varyingly amongst the positron and the neutrino as is shown in figure 1.4.

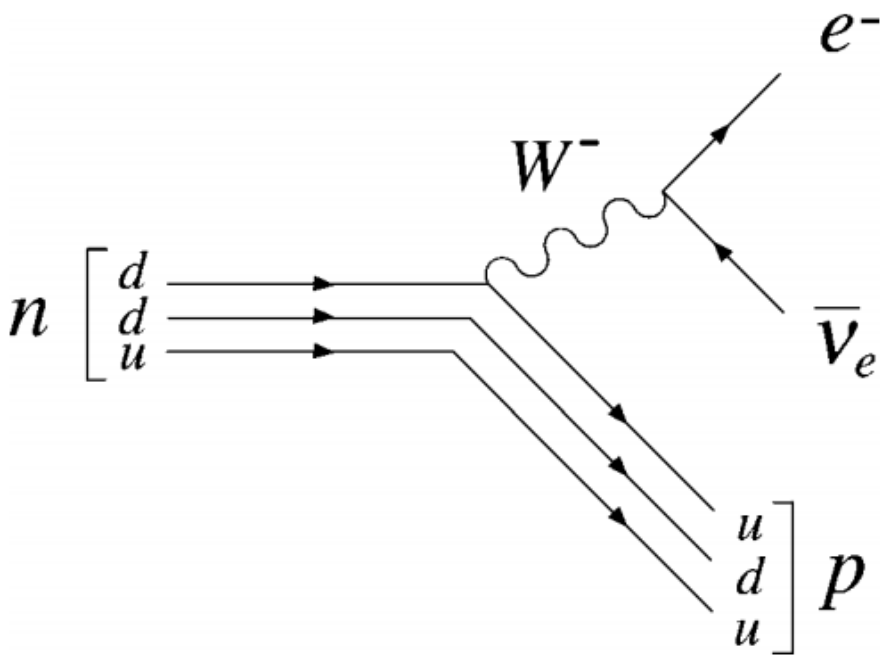

Figure 1.3: This Feynman diagram shows the beta decay process and how the intermediate vector boson W is the principle player in the exchange process of converting a down quark into an up quark. Drawing taken from [1]

The distribution in positron energy in Beta decay provided the earliest evidence for neutrinos. The variation in energies could only be explained by a yet undetected particle that carries away some momenta. As our detector was primarily built to observe neutrinos along with there directional information we will present a short discussion about neutrinos in the next section.

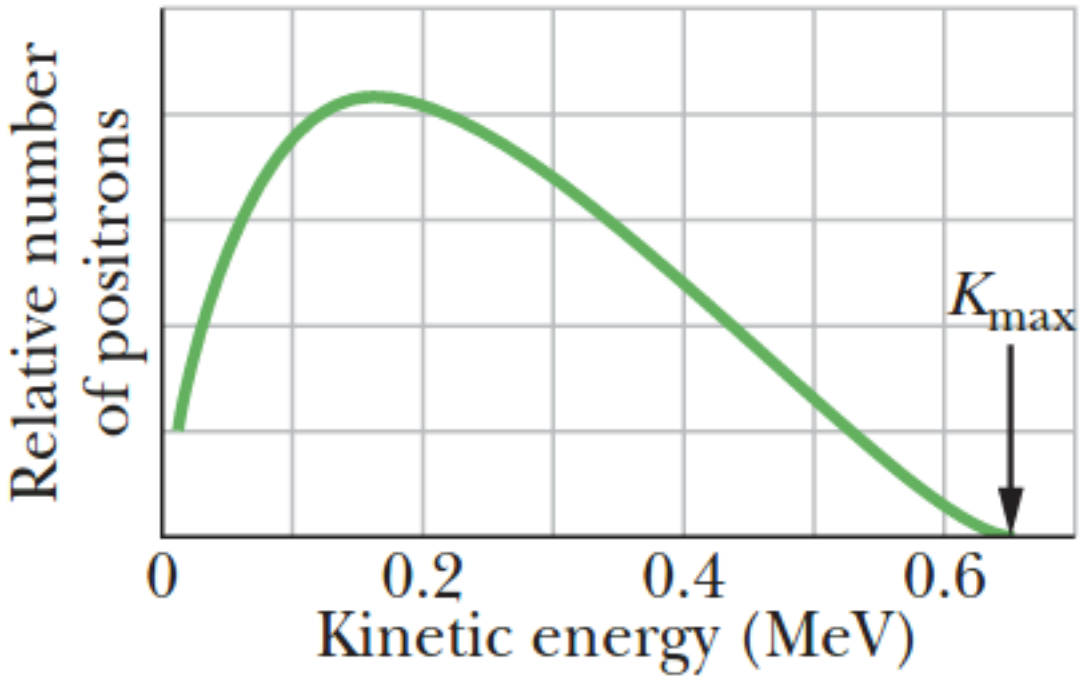

Figure 1.4: Here is a plot of the kinetic energy distribution of positrons in the beta decay of ^{64}Cuwhich takes a classic Poisson shape. The most probable energy for an emitted positron is approximately 0.15 MeVand we see that the kinetic energy is shared amongst the neutrino and the positron in different proportions for each event. The maximum energy possible for the positron is approximately 0.653 MeV. Image taken from [1].

Chapter 2

All About The Neutrino

As noted in the closing comments of the last section, our detector was originally built to detect neutrinos (specifically electron anti-neutrinos) along with their directional information. Therefore we present a summary chapter that discusses the evidence, nature, and mysteries of these particles.

2.1 The Case For Neutrinos

To explain the continuous energy spectra of beta decay, Wolfgang Pauli proposed in 1930 that there was a third particle emitted in the final products. He claimed this particle had to be neutral (he actually called this particle the neutron at the time). With this particle, momentum, spin and energy were conserved in beta decay. During this time Neils Bohr had a competing theory to explain the spectra by stating that energy was not conserved in

beta decay. When it was shown that the energies of the electrons from beta decay had an exact limit, Bohr's statistical approach to the energy conservation in beta decay fell apart.

Enrico Fermi was intrigued by Pauli's suggestion and he was able to combine Pauli's neutrino with Paul Dirac's positron in his 1934 paper [25]. In this theory the neutrino (to be exact it is the electron antineutrino) is one of the products of beta decay as shown in figure 1.3.

Wang Gangchang (1942) proposed an experiment to detect neutrinos in beta capture in 1942 [26]. Subsequently in 1956, Clyde Cowan, Frederick Reines, F. B. Harrison, H. W. Kruse, and A. D. McGuire published the first laboratory evidence of the electron anti-neutrino in the experiment later known as as the CowanReines neutrino experiment [27]. Their experiment used inverse beta decay to indirectly detect the electron anti-neutrino:

$$\bar{v}_e + p \rightarrow n + e^+ \tag{2.1}$$

They used the anti-neutrino flux from a reactor (ultimately they used Savannah River Plant in South Carolina as it had sufficient cosmic ray shielding) which amounted to 51013 neutrinos per second per square centimeter. The final design of their detector involved two water tanks where the protons interacted with the anti-neutrinos to create neutrons and positrons. The water

was doped with cadmium chloride which absorbs neutrons which promptly emit a gamma. The water tanks themselves were surrounded by liquid scintillator which gives off light through ionization when gammas pass through the material. The signal therefore was comprised of a prompt signal (the positron quickly annihilates with an electron to produce two gammas) and a delayed signal comprised of the light flash produced from the gamma emitted by the neutron absorption.

2.2 Neutrino Flavor

The muon neutrino was first discovered at the Brookhaven National Laboratory in 1962 by Leon Lederman, Melvin Schwartz and Jack Steinberger [2]. At the time, the Alternating Gradient Synchrotron (AGS) was the most powerful accelerator in the world. The AGS produced energetic protons that hit a tungsten target to produce a shower of pi mesons which subsequently travelled 70 feet to a 5000 ton steel wall. On route to the wall they decayed into muons and neutrinos and the neutrinos passed through the barrier while the muons were stopped. This new beam of pure neutrinos was shown to produce only muons as they slammed into aluminum plates, thereby proving that these neutrinos had a different flavor (muon flavor) than the electron neutrino. The group was awarded the Nobel prize in 1988 for their acheivement. An image from the experiment of the muon spark trails captured by photographic plates is given in figure 2.1.

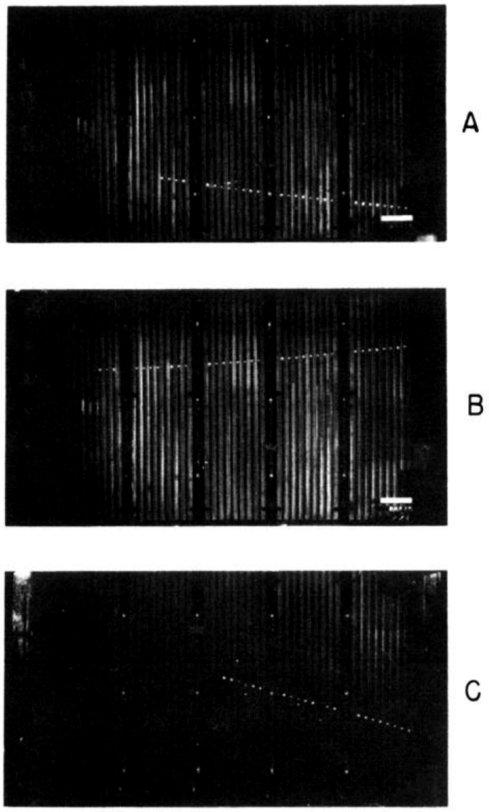

Figure 2.1: These are actual images from the Brookhaven experiment showing muon spark trails captured on photographic plates. Muon neutrinos incoming from the left interact to create muons which travel rightward. Shown are three different muon trails (the most energetic muon is shown in B). Image taken from [2].

When the tau particle was discovered in 1975 it became clear that a third flavor of neutrino was a real possibility. Evidence for its existence was apparent from missing energy and momentum in tau decays (much like the beta decay mystery that led to the discovery of the electron neutrino). In

2000, tau neutrinos were first directly observed by the DONUT collaboration at Fermilab [28].

As of today these are the only three neutrino flavors detected, consistent with the standard model of physics which states that there are 6 flavors of quarks and 6 flavors of leptons. We present them in figure 2.2 and figure 2.3.

Leptons (spin 1/2)

Generation	Flavor	Charge	Mass*	Lifetime	Principal Decays
first	e (electron)	-1	0.510999	∞	–
	ν_e (e neutrino)	0	0	∞	–
second	μ (muon)	-1	105.659	2.19703×10^{-6}	$e\nu_\mu\bar{\nu}_e$
	ν_μ (μ neutrino)	0	0	∞	–
third	τ (tau)	-1	1776.99	2.91×10^{-13}	$e\nu_\tau\bar{\nu}_e$, $\mu\nu_\tau\bar{\nu}_\mu$, $\pi^-\nu_\tau$
	ν_τ (τ neutrino)	0	0	∞	–

Figure 2.2: Shown here is a table displaying the three generations of the six flavors of leptons. Mass is given in units of MeV/c^2. Note that the masses are extremely small and are shown to be zero however we know that neutrinos do have a very small mass which we will discuss later in this chapter. Table image taken from [3].

2.2.1 Neutrino Oscillations

A neutrino which is created in a certain flavor can change into another flavor and the probability of this occurring varies periodically with energy and distance which we will quantify shortly. This behaviour was first predicted by Bruno Pontecorvo in 1957 [29]. In 1968, The Homestake experiment led by astrophysicist Ray Davis discovered a deficit in the solar neutrino flux predicted by the standard model [30]. He used a chlorine-based Cherenkov

Quarks (spin 1/2)

Generation	Flavor	Charge	Mass*
first	*d* (down)	−1/3	7
	u (up)	2/3	3
second	*s* (strange)	−1/3	120
	c (charm)	2/3	1200
third	*b* (bottom)	−1/3	4300
	t (top)	2/3	174000

Figure 2.3: Shown here is a table displaying the three generations of the six flavors of quarks. Mass is given in units of MeV/c^2. Image taken from [3].

detector and the results began the problem known as the 'Solar Neutrino Problem'.

In the 80s large detectors such as Kamiokande 2 have shown a deficit in the predicted ratio of muon neutrinos to electron neutrinos. The large size of the Cherenkov style detector helped to overcome the low flux of atmospheric neutrinos. Later the SuperKamiokande experiment provided precise measurement of atmospheric neutrino oscillation [31].

Nuclear reactors are a powerful anti-neutrino source. A wealth of experiments have attempted to study the oscillations of these anti-neutrinos as they propagate from the reactor. In 2012 Daya Bay was the first to discover in a short baseline reactor experiment that the phase angle θ_{13} [32], to be

discussed shortly, was not zero. This meant that the anti-neutrinos were changing flavor and this phenomenom presented itself in the form of a deficit of anti-neutrino flux from what was predicted theoretically.

The general structure of neutrino mixing can be described as such. Relating the flavor states in terms of the mass states and vice versa we can write:

$$\begin{aligned} |v_\alpha\rangle &= \sum_i \overline{U_{\alpha i}} |v_i\rangle \\ |v_i\rangle &= \sum_i U_{\alpha i} |v_\alpha\rangle \end{aligned} \tag{2.2}$$

Where the alphas represent the three different lepton flavors and the i's represent the mass states 1,2 and 3. U is called the PontecorvoMakiNakagawaSakata matrix or the PMNS matrix and the overline bar over the U represents the complex conjugate (for anti-neutrinos you would switch the complex conjugate symbol in the equations). As can be seen in (2.2), the first in the set of equations represents the flavor states as written in the eigenbasis of the mass states and vice versa for the second set. Writing this explicitly in matrix form we have:

$$\begin{bmatrix} v_e \\ v_\mu \\ v_\tau \end{bmatrix} = \begin{bmatrix} U_{e1} & U_{e2} & U_{e3} \\ U_{\mu 1} & U_{\mu 2} & U_{\mu 3} \\ U_{\tau 1} & U_{\tau 2} & U_{\tau 3} \end{bmatrix} \begin{bmatrix} v_1 \\ v_2 \\ v_3 \end{bmatrix} \tag{2.3}$$

And the matrix elements of U can be expressed as:

$$U = \begin{bmatrix} c_{12}c_{13} & s_{12}c_{13} & s_{13}e^{-i\delta} \\ -s_{12}c_{23} - c_{12}s_{23}s_{13}e^{i\delta} & c_{12}c_{23} - s_{12}s_{23}s_{13}e^{i\delta} & s_{23}c_{13} \\ s_{12}s_{23} - c_{12}c_{23}s_{13}e^{i\delta} & -c_{12}s_{23} - s_{12}c_{23}s_{13}e^{i\delta} & c_{23}c_{13} \end{bmatrix} \tag{2.4}$$

where $c_{ij} = cos(\theta_{ij})$ and $s_{ij} = sin(\theta_{ij})$. Two extra phase factors would need to be included if neutrinos are majorana particles (they are their own anti-particles) which to date has not been determined. The phase factor δ is related to charge-parity violation which we know is a signature of the weak interaction [3]. The $v_i's$ are mass eigenstates and they can be described by plane waves:

$$|v_i(t)\rangle = e^{-iE_i/t - p_i \cdot x_i}|v_i(0)\rangle \tag{2.5}$$

where E_i is the energy of the eigenstate i, t is the time of propagation, p_i is the momentum and x_i is the distance travelled. Here natural units have been employed with $c = 1$ and $\hbar = 1$. Physically, we can imagine a neutrino starting out as one flavor and being composed of a linear combination of mass eigenstates that individually propagate at different speeds. The mass eigenstates in turn are themselves linear combinations of flavor states. Thus, interference can cause a neutrino which started out in one flavor to convert into another as it propagates.

The probability of a neutrino changing flavor from α to β is:

$$P_{\alpha\to\beta} = \langle v_\beta(t)|v_\alpha(0)\rangle = |\sum_i U_{\alpha i}U_{\beta i}e^{-im_i^2 L/E}| \tag{2.6}$$

The probability oscillates with respect to the energy, distance of propagation, and while its not as apparent in this form, the mass-square difference of mass eigenstates.

As noted earlier in this chapter, reactor short baseline studies help to quantify the mixing parameter θ_{13} and are usually on the order of a few meters to a few km. One of the goals of our detector was to study this mixing parameter and we shall discuss our attempts in a later chapter.

Chapter 3

Introduction to the mTC

In this chapter we discuss the motivations for the miniTimeCube (mTC) and its specifications. Results from our data collection will be discussed in chapters 7 and 8.

3.1 Motivation

A number of mysteries remain in neutrino physics, such as the mass hierarchy problem and the issue of whether neutrinos are Majorana or Dirac fermions. At the same time our capabilities of detecting neutrinos has come to a turning point where bigger and more advanced detectors capable of absorbing greater and greater neutrino fluxes. However these projects are increasingly becoming more expensive and as such there is a need for making neutrinos studies capable on a smaller scale. Practical applications of a small compact

and directional neutrino/neutron portable detector would be the ability to locate the geospatial location of a nuclear reactor or special nuclear materials (SNR).

The main reaction we are trying to detect is inverse beta decay which was introduced back in chapter 2. A diagram showing the reaction is given in figure 3.1. The prompt signal is comprised of a positron-electron annihilation which culminates in the production of two 511keV gammas, and the delayed signal is the neutron capture on boron which releases a 470keV gamma 94 percent of the time. We will discuss this more in chapter 5. In addition to detecting neutrinos, precise neutron scattering can offer us information on neutrino direction, thereby enhancing our depth of understanding of the data obtained. In the diagram the first two bounces of the outgoing neutron creates the $\overrightarrow{P_2 - P_1}$. A simple kinematic analysis shows that the neutron carries most of the momentum of the antineutrino while the positron carries most of the energy, thus a sufficient number of statistics of these vectors can make an estimate as to the direction of the incoming antineutrino. Further, in the absence of IBD, in which we try to detect a neutron source, the scheme is still the same for neutron directionality where we gather vector statistics based on the $\overrightarrow{P_2 - P_1}$ vectors. Our goal is to be able to do all of this with a compact portable detector.

The miniTimeCube (mTC), shown in simulation in figure 3.2, represents a new step in this direction. The mTC is a compact (~ 2200 cm^3 active volume), densely instrumented, fast timing plastic-scintillator detector designed

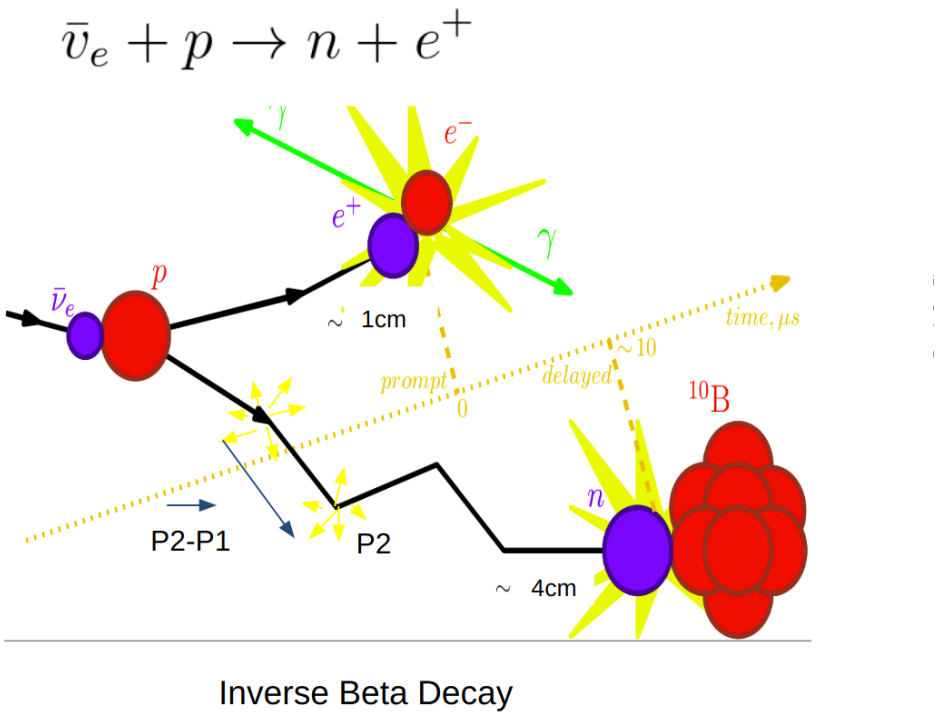

Figure 3.1: Diagram showing inverse beta decay. The positron travels an average of 1cm while the neutron travels an average of 4cm. The positron-electron annihilation represents our prompt signal and the neutron capture.

as a proof-of-concept for future reactor antineutrino detectors and neutron directional detectors [4].

A small compact and portable neutrino/neutron detector would have the advantage of being able to study neutrinos at short baselines, the reactor anti-neutrino anomaly [33], as well as have practical benefits in monitoring reactor fuels and providing nuclear security. The mTC is an advancement of the CCD-based detector concept which had problems with scalability to large detection volumes [34, 35]. The mTC employs state of the art scintillating

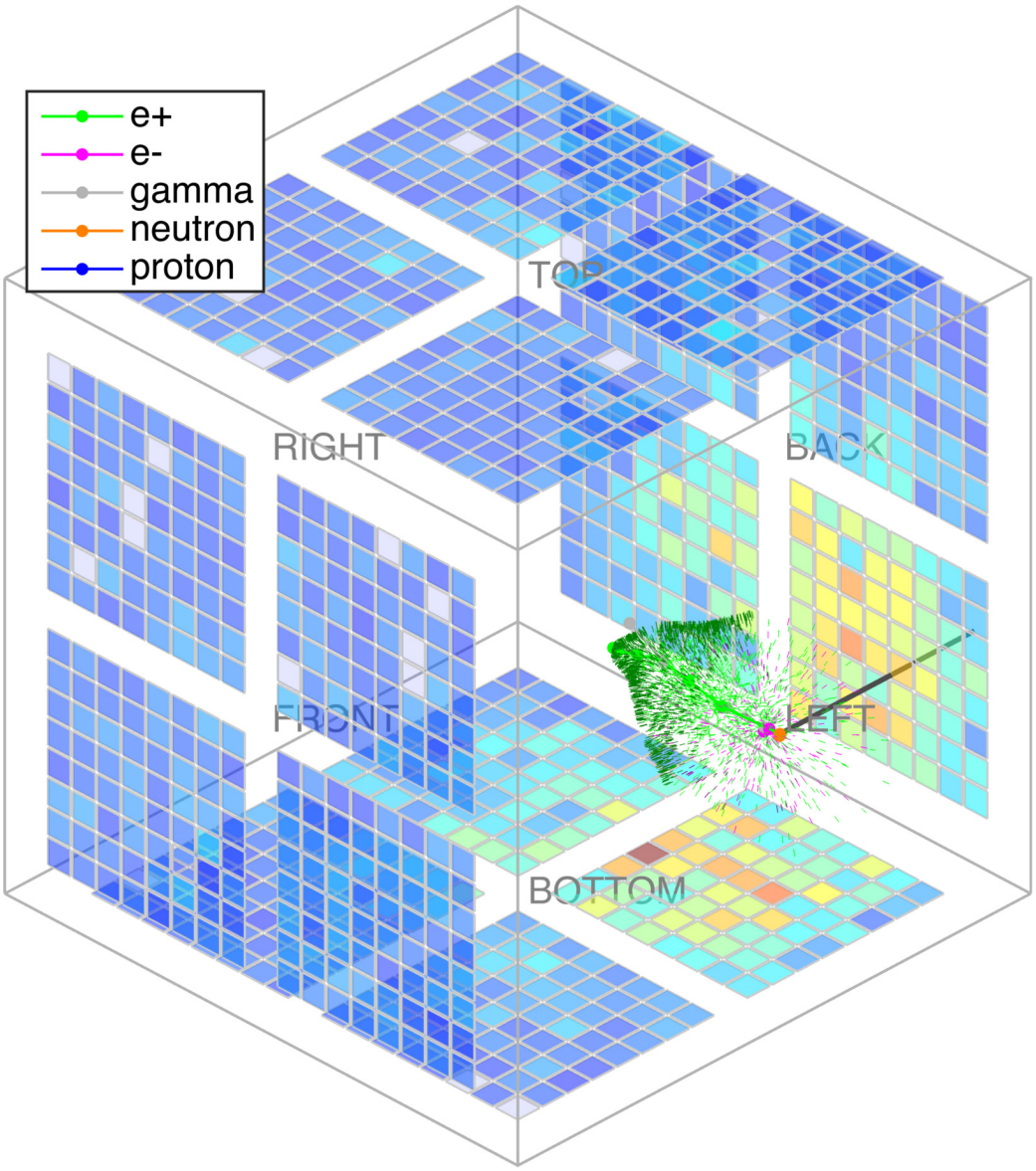

Figure 3.2: simulation of a 10 MeV $\overline{\nu}_e$ interaction in the 13 cm cubical mTC. Photons colored identically to parent particles. Image from our paper [4].

material along with densely packed fast timing instruments to improve upon these detectors. The mTC concept relies on reconstructing a Fermat surface

based on first time arrivals of photons, which leads to excellent spatial and timing angular resolutions that far exceed what one might expect with typical scintillator decay times [36].

The main reaction we are trying to detect is inverse beta decay which was introduced back in chapter 2. A diagram showing the reaction is given in figure 3.1. The prompt signal is comprised of a positron-electron annihilation which culminates in the production of two 511keV gammas, and the delayed signal is the neutron capture on boron which releases a 470keV gamma 94 percent of the time. We will discuss this more in chapter 5. In addition to detecting neutrinos, precise neutron scattering can offer us information on neutrino direction, thereby enhancing our depth of understanding of the data obtained. In the diagram the first two bounces of the outgoing neutron creates the $\overrightarrow{P_2 - P_1}$. Since a simple kinematic analysis shows that the neutron carries most of the momentum of the antineutrino while the positron carries most of the energy, if we gather enough statistics on these vectors we can make an estimate as to the direction of the incoming antineutrino. And in the absence of IBD, in which we try to detect a neutron source, the scheme is still the same for neutron directionality where we gather vector statistics based on the $\overrightarrow{P_2 - P_1}$ vectors.

Due to the small volume of the mTC, the detector requires excellent timing resolution which is used using commercial micro-channel plate photomultiplier tubes (MCPs) which have a timing resolution of $50ps$. Combined with our fast readout electronics we expect timing resolutions of $100ps$ which cor-

responds to about $2cm$ spatial resolution in the scintillator. We can achieve further improvements in resolution by having multiple pixels for light collection, which roughly scales as $1/\sqrt{N_{pe}}$. With its state of the art timing and spatial resolution we can expect to make many precise measurements. While its small size may prohibit some of the proposed applications it does serve as a proof of concept for future similarly constructed detectors such as Nulat [37].

The initial version of the detector, shown in FIG. 3.3, was finished in 2013 and was shipped off to the National Institute of Standards and Technologies (NIST). Testing and calibrations at NIST began in 2014 and upgrades to the system were made as were required. Full data runs were taken in front of the test reactor at NIST were initiated and completed in late 2015 and the results of those tests will be discussed in chapter 7.

3.2 The Design of the mTC

At the core of the mTC is a (13 cm)^3 cube of plastic scintillator (Eljen Technology EJ-254), doped with 1% natural boron (0.2% ^{10}B) and this material serves as the particle detector volume [5]. Coupled directly to the surface are 24 PLANACON MCP-PMTs (PHOTONIS XP85012), hereafter referred to as simply "MCPs," shown in figure 3.4 [38]. These are used to collect the photons emitted from the various particle interactions in the cube. The MCPs are clamped and 'glued' to the plastic surface using ELJEN Technol-

Figure 3.3: Photograph of mTC's mount-racks, light-tight aluminum enclosure, data acquisition system, and power supplies. Image from our paper [4].

ogy EJ-550 optical grease. The anode plane is segmented into 64 pixels and for 24 MCPs this totals 1536 channels surrounding the mTC. Clearly this is a dense spatial coverage for light collection for the system. The scintillation

and Cherenkov spectra for the EJ-254 is shown in figure 3.5. As can be seen from the figure, most of the light we will detect will be scintillation light in the UV range. The scintillation efficiency of the EJ-254 plastic is 9200 photons per MeV.

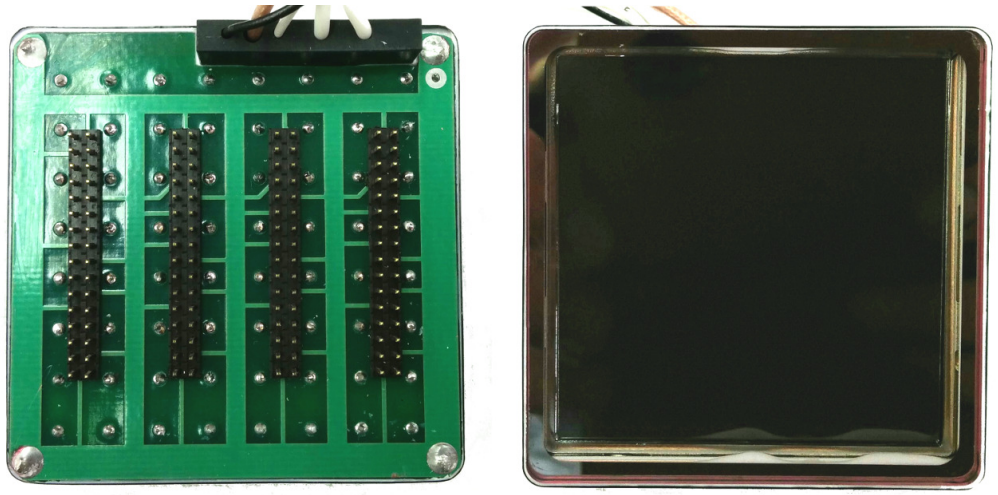

Figure 3.4: Photograph of the PLANACON MCP-PMT. 24 of these are used in the mTC.

The compact nature of our electronics, MCPs, and our scintillator allows for our detector to fit inside a volume of 1/8 m^3. A CAD drawing of our scintillator with only one side populated by 4 MCPs and our front end electronics is shown in figure 3.6.

The main detector, ancillary electronics, and power supplies fit in stacked plastic cases, with a clearance footprint of 0.75 m wide by 1.2 m deep by 2.5 m high, and requires only 115 VAC and a network connection for remote operation. The assembled and integrated mTC, including associated servers

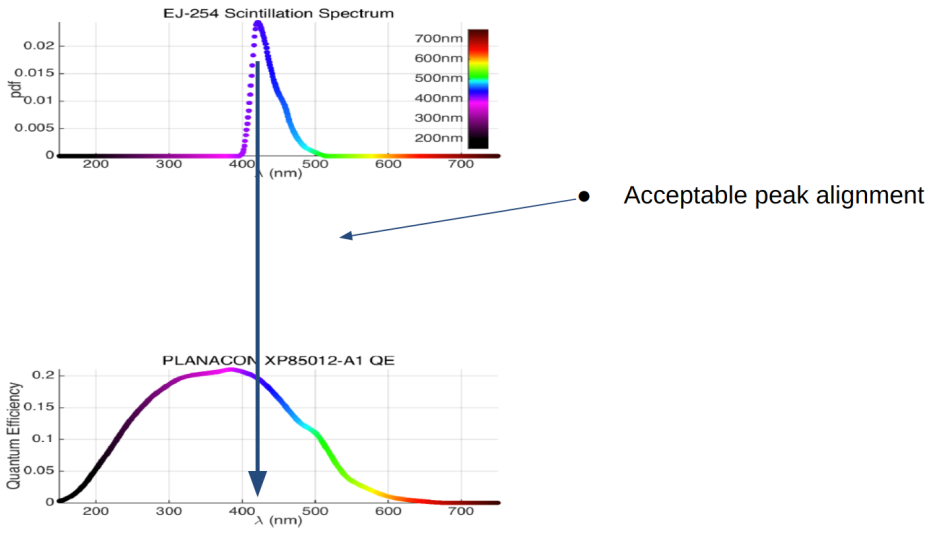

Figure 3.5: Scintillation vs quantum efficiency plots for the EJ-254 scintillator. Image taken from [5].

for data acquisition, is shown in figure 3.3. A water-based chiller, with flow around 8 LPM, provides cooling needed for operation in the shielded enclosure. The power consumption is roughly 2 kW, including $\sim$ 1 kW from the chiller itself. The size and power consumption make this a relatively portable detector, capable of being operated from a truck or a ship [4].

3.3 Electronics

The front end electronics for the mTC were all custom designed at UH with UH personnel. The heart of the front-end electronics is the IRSD [39] ASIC (Application Specific Integrated Circuit) chip. The IRS chips have been used in many projects that require fast sampling and a deep buffering system [40–

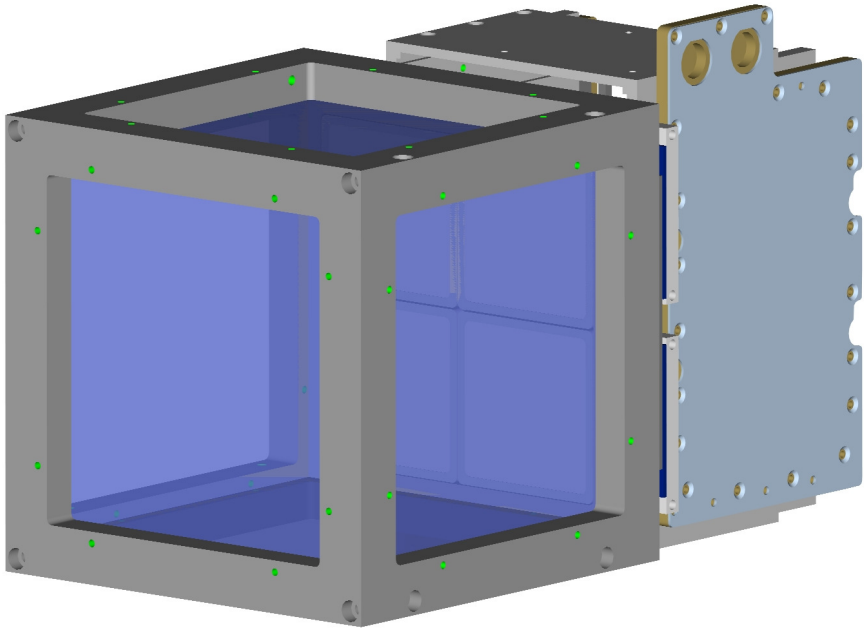

Figure 3.6: CAD Drawing
CAD drawing of the mTC with one face populated by MCPs and the front end electronics. Image from our paper [4].

42]. The ASIC is a waveform sampler and each chip has eight analog input channels. In addition, each channel has a sampling stage, an intermediate sampling stage proceeded by a deep buffering stage, on chip digitization and on channel threshold triggers. The deep buffering system of the ASIC allows for longer trigger windows and an overall larger time record per event. The sampling stage works much like other waveform samplers where a multi-GSa/s switched capacitor array (SCA) has a sampling clock propagate down a delay line. Buffer amplifiers are used to propagate the voltages from the intermediate stage to the final deep buffer storage. The intermediate stage is required for the buffer amplifiers to have enough time to settle in between

transfers. A block diagram showing the multiple stages of a single channel within the ASIC is shown in figure 3.7.

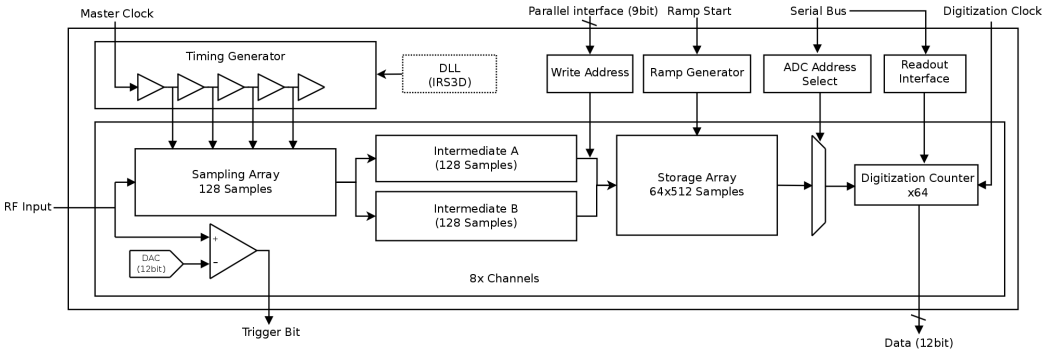

Figure 3.7: Block Diagram
Block diagram of the IRS ASIC architecture. Eight channels of analog input are received by a set of eight sampling arrays, with sampling timing based on a common timing generator, driven by an external clock. This timing generator also determines the timing of transfers from the sampling arrays to intermediate and storage arrays. The target location for the transfer from the intermediate to storage array is controlled by the user with a 9-bit parallel bus. The storage array consists of an impressive 32,768 capacitors which allows for a large window of time for recording an event. A separate pin is used to start an internal voltage ramp, used to digitize 64-samples of the storage array for all eight channels in parallel. Selection of the storage address to digitize is controlled through a serial interface. A clock for the Wilkinson digitization process is generated internally (IRS3B) or provided externally (IRS3D). Once data is digitized, the channel and sample to readout are controlled by a second independent serial interface. Digitized data is available on a parallel 12-bit bus. A number of DACs and internal timing parameters are controlled by a third serial register interface. Reference [4].

The IRS has an on chip Wilkinson ADC which digitizes a 64 sample block of data for all eight channels in parallel. This data is readout one sample at a time down a 12 bit parallel bus line. The analog channels are connected to a comparator and the digital bits inform the user of how many 'hits' the

ASIC has had. Adding these bits up across all the ASICS gives us our 'level A' trigger. From here we can do further investigations to see if the candidate event is of interest. We will discuss more about triggering in a later section. Some functional parameter information regarding the IRSD ASIC is given in table 3.1.

Our front end electronics are ultimately composed of 12 board stacks, one of which is shown in figure 3.8. Each boardstack contains 4 carrier boards and each carrier holds 4 ASIC chips and the amplifier chains that provide the RF inputs. In addition, there is a SCROD board (the control board) which holds the FPGA which provides the control signals needed to operate the ASICS. An interconnect board acts as an interface between the SCROD and the carriers.

The board stacks communicate with a custom PCB designated Clock and JTAG In PCI (hereby referred to as CAJIPCI). The communication is done via differential pairs of CAT7a cable. The low jitter clock ($\sigma_t < 2$ ps) is split 12 ways, one for each board stack. The front end modules in turn return a module level trigger back to the CAJIPCI (trigger A) and the CAJIPCI responds with a system wide trigger (trigger B) over another differential pair. We will discuss triggering in more detail in the next section.

Table 3.1: Statistics for the IRSD performance

Parameter	IRS Range	mTC Setting
Channels	8	
Sampling cells	128	
Storage depth	32,768	
Analog bandwidth	> 300 MHz	
Digitization	on-chip Wilkinson	
Quantization	12(9)-bits logged(effective)	
Dynamic range	~ 2 V	
Typical noise	~ 1 $\mathrm{mV_{RMS}}$	
Sampling rate	1–4 GSa/s	2.73 GSa/s
Master clock	8–31 MHz	21.3 MHz
Buffer time	$(8 - 32)\mu$s	12.0 μs
Conversion time	> 2 μs	6.2 μs

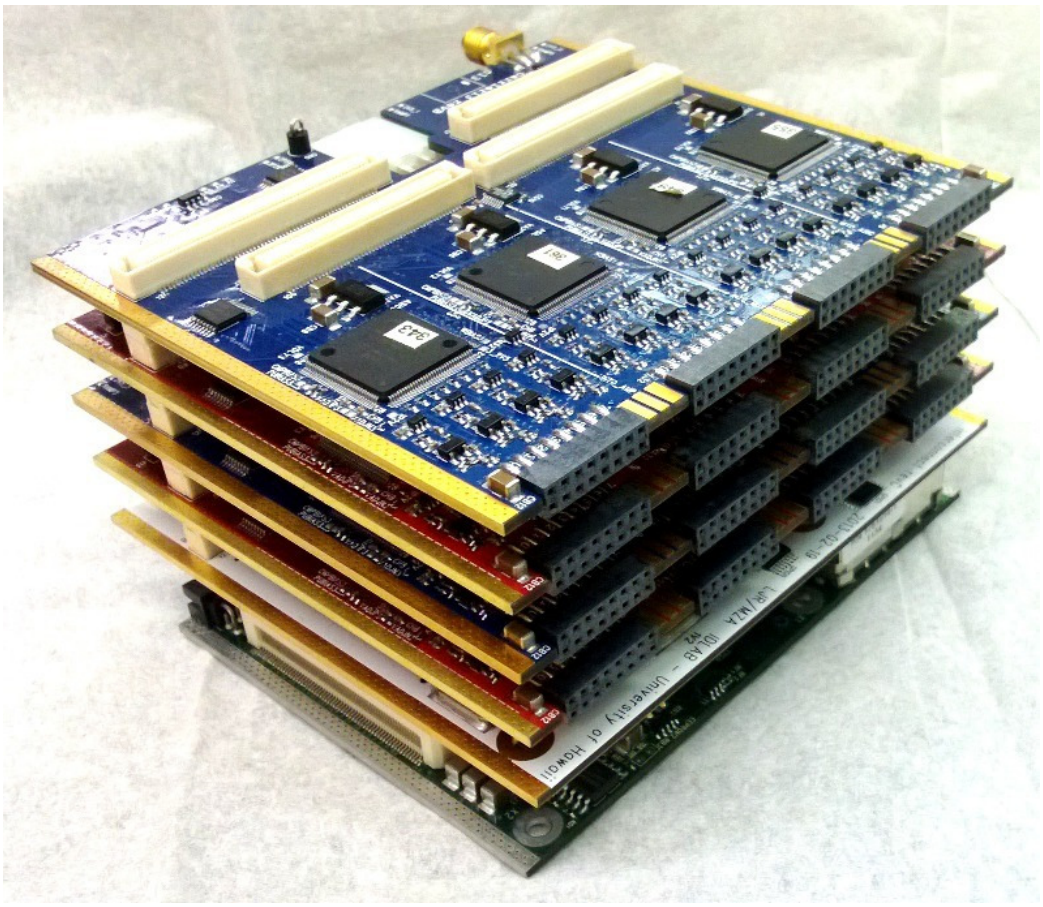

Figure 3.8: A single boardstack consisting of 4 carrier boards which house a total of 16 ASICs, an interconnector board, and the SCROD board (the control board) containing the FPGA. 12 of these stacks populate the mTC.

3.4 Triggering

There are three separate triggers available in our system. The L0 trigger is an ASIC specific threshold level which manifests as a single bit. It basically sets the level for a minimum voltage required for a signal to be counted per ASIC channel. These thresholds can be set on the on chip ADC via the FPGA and

it represents our lowest level trigger. The next Level trigger, the L1 trigger is a bit which counts the total number of L0 bits which have been collected in a a particular boardstack. If the number of L0 triggers fall into a user defined threshold, a signal is sent to the CAJIPCI for processing. Finally the CAJIPCI monitors the L1 triggers and if it lands in a user defined threshold the CAJIPCI sends a signal back (the L2 trigger) to the front end modules which initiates digitization. If all trigger thresholds are met we consider this to be an event of interest. However, we can operate on a simpler trigger design where we abolish the L1 trigger altogether. In this scheme we simply count the bits sent from each ASIC and when the sum surpasses a user defined threshold a signal we call the A trigger is sent to the cajipci. Depending on the interaction we are looking for, the cajipci can send a bit back to the FPGA to intitite digitization, or the system can wait for a second trigger (B trigger) to be sent to the cajipci to initiate data acquisition. In fact, an AB trigger was employed in our IBD detection setup and we illustrate this trigger scheme in figure 3.9.

3.5 Data Acquisition

Data digitization begins once a trigger is sent to the front end module from the cajipci. The data is sent down fibre optic cables in which a GB ethernet interface is used. The data is gathered by PCIe Ethernet cards which run on a rack mounted server. This process can be operated directly or remotely

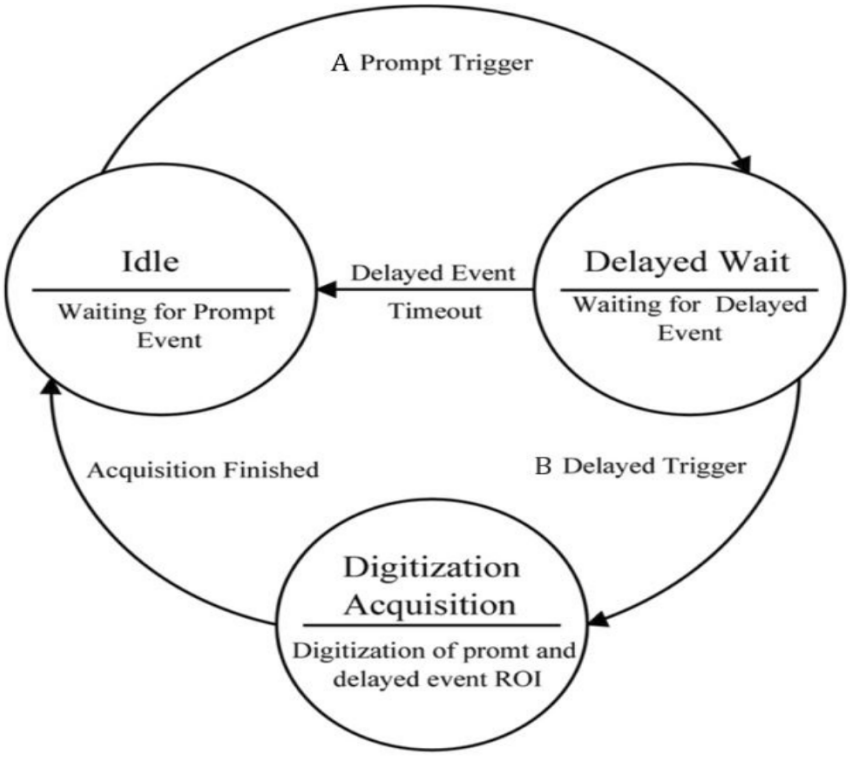

Figure 3.9: A flow chart describing our IBD scheme. Firstly the system sits in an idle state waiting for an A trigger (positron-electron annihilation). Once an A trigger has been sent to the cajipci the system has approximately 12 microseconds to detect the delayed event (boron capture). If the delayed event occurs a B trigger is sent and digitization ensues. If a delayed event is not detected in the 12 microsecond window the system goes back to idle mode and waits for an A trigger once again.

over this network. Several automated programs have been written to start the detector up and to allow the user to fine tune the detector response. Before data acquisition begins, pedestals are taken and timing parameters are scanned as well as thresholds. This is done to ensure optimum calibration.

3.6 Power

A low voltage (LV) and a high voltage (HV) commercial power supply are operated remotely and stored beneath the mTC's aluminum enclosure. Since the mTC is enclosed and the front end electronics consumes 330 watts, cooling of the system is of the utmost importance. A chiller is employed that pushes deionized water at 2GPM. The water is passed through hard drive chiller plates which are attached to the front end electronics card cages. The ASICs are maintained at a temperature of $30 - 35°C$ which is well within their operating limits.

3.7 Calibration

A number of calibrations were made to the system to ensure accurate amplitude and timing measurements. We will describe the main calibration techniques in detail in this section.

3.7.1 Electronics calibration

The calibration of the electronics is two-fold. Firstly due to fabrication differences in the deep storage capacitors there are slightly varying thresholds for the comparators to observe. This results in a fixed voltage pattern which differs for each capacitor and to remove this expected artifact we take what is known as pedestals. To calculate pedestals we can remove any signal from

the system and run a software trigger and record the results. We take over $50 * 10^6$ samples to cover all the storage cells of the ASICs in the system. For subsequent runs we subtract these pedestals to remove any systematic differences.

Fine timing calibrations are also an important part of our system readiness procedure. As in the case of the comparator thresholds, there are systematic differences in the timing between samples. A current starved inverter chain is what is used as our delay line for sampling data. The differences in the fabrication of the gates involved in this chain results in slightly differing responses to incoming signals. To correct for these effects we use a function generator to inject an MCP like pulse which has a known delay time with respect to the sampling clock. We alter this delay in small steps to map out the differences between our sampled signal to the known delay. A total of 128 samples for each ASIC must be taken, since the same delay line is used to time all 8 channels. This amounts to a total 24,576 samples for the entire detector.

In figure 3.10 we show the semi-raw signal digitized output for a muon event (code was written to organize for correct time windows and to subtract pedestals). This is a readout of all 1536 channels after ASIC-level calibrations are applied (without these calibrations the plot would be greatly misaligned with respect to time and amplitude). We describe the data as semi-raw because all waveforms are actually cut-off at 1500 ADC counts and this is due to limitations in the Wilkinson ramp digitizer as well as the the voltage

bias setting on the ASIC. Therefore, all pulses above 1500 ADC counts were estimated using a splining technique based on a cubic polynomial. While this technique is great for show and tell (and for less energetic pulses it can be quite accurate), it was our experience that for higher energy events the spline process sometimes exaggerated the peaks of the curves, which led to overestimating our photon counts. To consistently estimate the peak or amplitude of our curves we collected 1000s of pulses that were not saturated and found a vary consistent value of the ratio of the maximum peak over the minimum (the undershoot of the pulse). We then worked backwards using the often unsaturated undershoot of the pulse in conjunction with this ratio to estimate the missing peak value.

3.7.2 Calibration with Laser Source

A precision timing laser system (Advanced Laser Systems EIG1000D) was set up to operate inside a light tight box with a stepper motor which controlled the output location and could adjust the laser attenuation. Variable neutral density filters were used for the latter and light intensity was controllable to the single photo-electron (PE) level. This was important as single photon studies allow us to study the quantum efficiency of our system more accurately as well as giving us the opportunity to analyze single photon behaviour in our system. Laser studies allowed us to calibrate for variations in the electronics, amplifier chains, and differences in the gain of the MCPs. The laser was triggered by the CAJIPCI so as to allow the pulse to be ad-

justed relative to the master clock. A relative gain map is presented in figure 3.11.

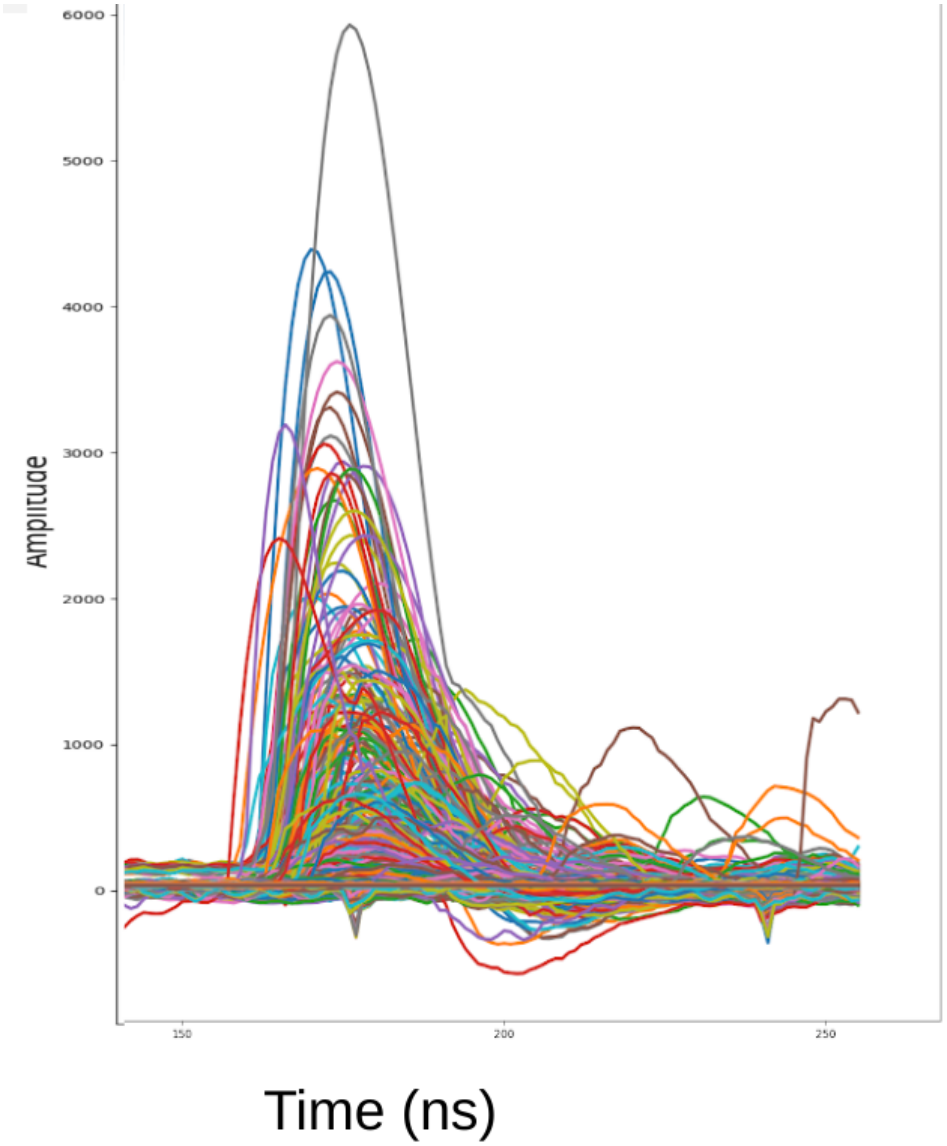

Figure 3.10: The readout of the 1536 channels of the mTC for a muon event after ASIC level calibrations are made.

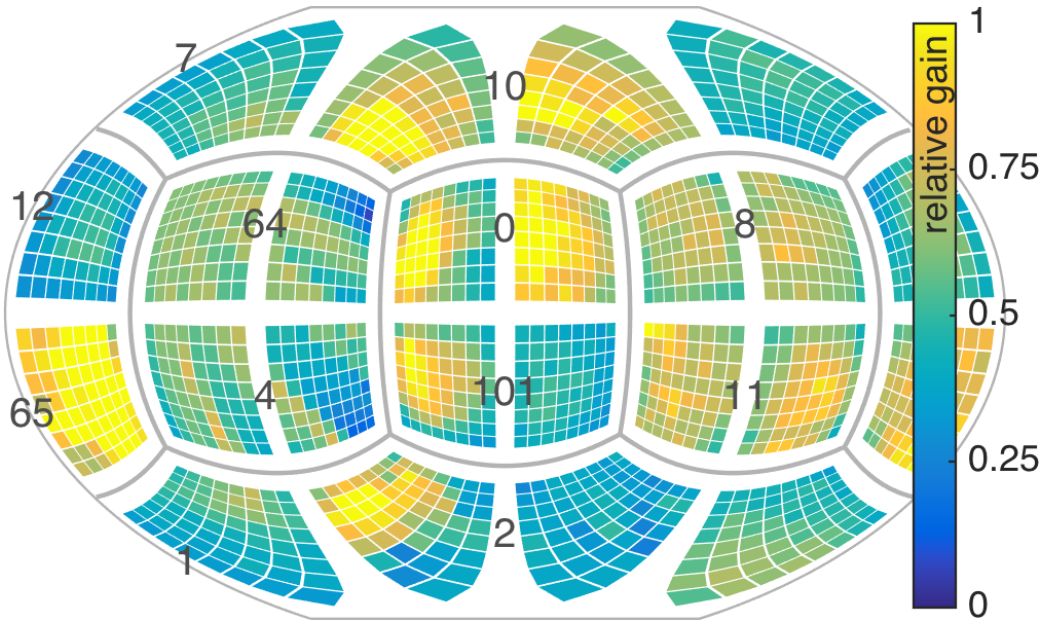

Figure 3.11: A relative gain map for a fully populated mTC obtained using laser data and the results are used for calibration on the software side. Image from our paper [4]

HV is separately controlled for each MCP which allows gain to be independently tuned for each module. The pixels for each MCP vary with respect to gain response to the voltage input. In conjunction with the laser source tuned to the single PE level, we can fine tune the HV for each PMT in order to create a flat field response with respect to gain across all PMTS. In fact this is done before we determine single PE thresholds for each pixel in the detector as this calibration helps to limit the variations that will remain among the pixels. These remaining differences are a result of intrinsic differences inherent in the electronics (trace differences, amplifier response variations, etc..). These final calibrations are made on the software side.

Cosmic ray muons provide us with a way to study our detector response. The cosmic muon flux peaks at an energy of 2 MeV and is peaked in the vertical direction and drops off with cos^2 of the zenith angle at sea level (approximately 1 Hz through the detector). With a stable flux we can use these particles to calibrate our detector. Operationally we want to lower the HV, as well as control our triggers to avoid saturating the electronics. The minimum ionizing energy loss rate for polyvinyltoluene (the plastic in the mTC's scintillator) is 1.956 MeV cm^2/g with density 1.02 g/cm^3, so the net (mean) energy loss rate in the cube should be about $dE/dx = 2.3$ MeV/cm [4] [43].

3.8 Remote Operation

Our team was able to implement remote operating capabilities in an impressive short period of time (about 6 months). As a result, we were able to operate the mTC at the reactor, or from Hawaii, or any place on Earth with a laptop and an internet connection. We were able to monitor the flow rate of the cooling system, temperatures of the ASICs, humidity, trigger rates, and other important run information. We also implemented an automatic shutdown feature if any guages read past certain user defined thresholds. For example if one or more temperatures gauges past the allowed threshold, or if the flow rate of our chiller dropped too low, an automatic shutdown would occur after a short countdown. This was crucial not just to protect expensive

equipment in our experiment, but also to prevent a potential disaster such as a massive water leak 5m from test reactor. An image of the remote desktop is given in figure 3.12.

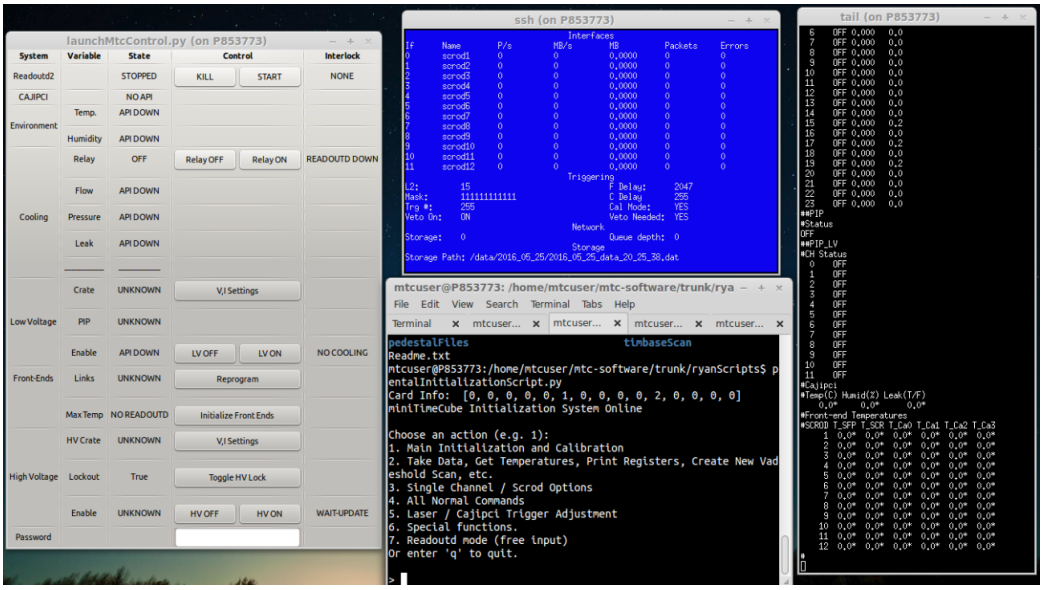

Figure 3.12: An image of the mTC workstation which is accessible by logging in with special permission laptops. On the left side of the screen is the main operating GUI which allows the user to turn the system on in segments. We can also use it to monitor a multitude of control items and to program different trigger schemes

Chapter 4

Reconstruction

Our reconstruction techniques are based off the estimation of a group of parameters which fully describe an event. These parameters can include location (x,y,z), the time of occurrence, the energy of the interaction, and the weight which will be discussed in the neutron recoil section. This set of parameters we will denote as α. We use a point fit technique inspired by the Double Chooz fitting technique [44] and modified for our purposes.

4.1 Probability for Single Photon Detection

In general we have that the probability for a single photon being detected in the ith channel is:

$$l(z_i|\alpha) = P_\Omega P_\gamma P_T \Lambda_t Q \tag{4.1}$$

where z_i is our measurement (a count of a single photon at a time t) and α is the set of parameters we are estimating. P_Ω is the solid angle probability, P_γ is the unattenuated energy probability, Λ_t is the temporal likelihood, and Q is the quantum efficiency. Each one of these factors are to be discussed next.

4.1.1 Solid Angle

The solid angle of a cone with half-angle θ is :

$$\Omega = 2\pi(1 - cos(\theta)) \tag{4.2}$$

We can approximate this formula for an arbitrary shape S as seen form a point θ_Ω:

$$P_\Omega = 2\pi\Big(1 - \frac{r}{\sqrt{r^2 + a^2}}\Big)\hat{r} \cdot \hat{n} \tag{4.3}$$

where $\vec{r} = \theta_\Omega - P_z$ is the vector pointing to the PMT location P_z on the surface to the point θ_Ω, $\hat{n}$ is the unit normal vector on the surface at the point P_z, a is the radius of the surface area subtended by the cone, and r is the norm of $\vec{r}$. Essentially if a certain PMT (or a group of channels) on the mTC wall observes a large percentage of the emitted photons, maximizing the solid angle probability will involve moving our point source estimation closer to that area. The approximation occurs in our case comes from substituting the half length of a side the square pixel for a in our equation. An illustration of

the solid angle is given in figure 4.1.

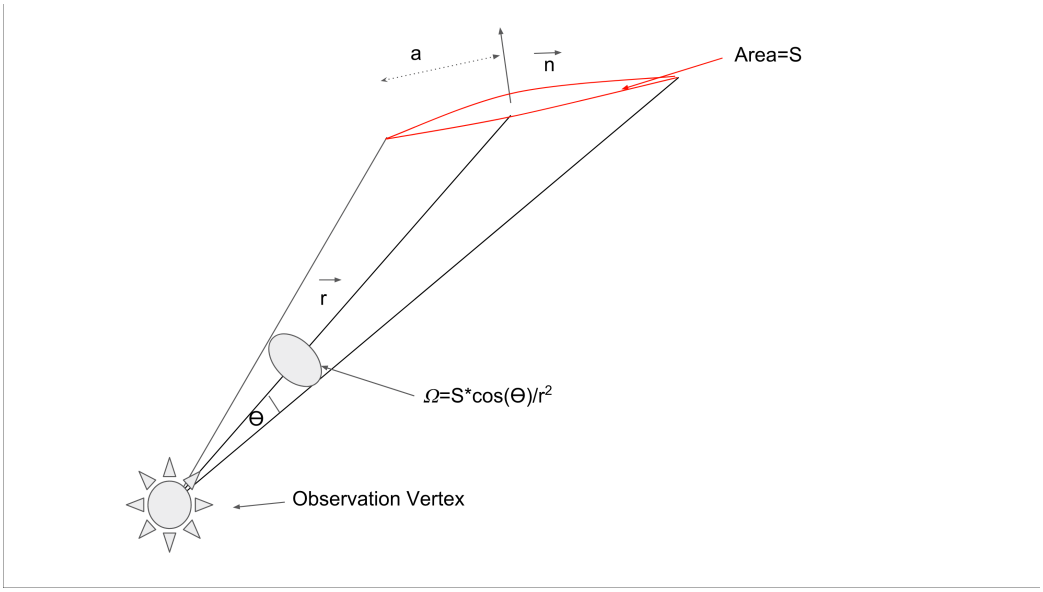

Figure 4.1: Illustration of the solid angle, the 3d angle enclosed by a conical surface from a vertex

.

4.1.2 Energy Attenuation

Photons can be reabsorbed and re-transmitted in a scintillating medium. The fraction of the energy that is attenuated after a photon has travelled a distance x is given by the Cumulative Distribution Function (cdf) as:

$$f(x, \lambda) = 1 - e^{-\lambda x} \tag{4.4}$$

where λ is the inverse of the attenuation length of the medium that is being transversed. The survival probability then is simply:

$$P_\gamma = 1 - f(x, \lambda) = e^{-\lambda x} \tag{4.5}$$

4.1.3 Reflection

When a light ray travels between two mediums which have different indexes of refraction (n) some combination of energy is transmitted and reflected. The equations that govern this phenomena is the Fresnel-Equations. These are some of the most fundamental equations derived from classical physics and were developed by Augustin-Jean Fresnel in the 1800s [45]. The equations are fully consistent with the theory of light in the Maxwell framework. Firstly the law of reflection states that the reflection angle θ_r is equal to the incident angle θ_i :

$$\theta_i = \theta_r \tag{4.6}$$

For the transmitted light, the transmission angle θ_t is given by Snell's Law as:

$$\theta_t = arcsin\Big(\frac{n1}{n2} sin(\theta_i)\Big) \tag{4.7}$$

For s-polarized light we have for the reflection coefficient:

$$R_s = \left| \frac{n_1 cos(\theta_i) - n_2 cos(\theta_t)}{n_1 cos(\theta_i) + n_2 cos(\theta_t)} \right|^2 \tag{4.8}$$

which can be written as:

$$R_s = \left| \frac{n_1 cos(\theta_i) - n_2 \sqrt{1 - \left(\frac{n1}{n2} sin(\theta_i)\right)^2}}{n_1 cos(\theta_i) + n_2 \sqrt{1 - \left(\frac{n1}{n2} sin(\theta_i)\right)^2}} \right|^2 \tag{4.9}$$

For p-polarized light we have for the reflection coefficient:

$$R_p = \left| \frac{n_1 cos(\theta_t) - n_2 cos(\theta_i)}{n_1 cos(\theta_t) + n_2 cos(\theta_i)} \right|^2 \tag{4.10}$$

which can be written as:

$$R_p = \left| \frac{n_1 \sqrt{1 - \left(\frac{n1}{n2} sin(\theta_i)\right)^2} - n_2 cos(\theta_i)}{n_1 \sqrt{1 - \left(\frac{n1}{n2} sin(\theta_i)\right)^2} + n_2 cos(\theta_i)} \right|^2 \tag{4.11}$$

For light that is not polarized we assume the light is equal proportions of p and s polarizations and we take the average:

$$R = \frac{R_p + R_s}{2} \tag{4.12}$$

and the transmission coefficient is simply:

$$T = R - 1 \tag{4.13}$$

4.1.4 Temporal Likelihood

We also would like to introduce a timing contribution to our fitter in the form of a temporal likelihood function. The probability density function (pdf) for

the temporal likelihood that we use is presented here:

$$\Lambda_t = e^{-(t-(\theta_t+r/v))/t_f} * (1 - e^{-(t-(\theta_t+r/v))/t_r}) \tag{4.14}$$

where t is the time of the first photon arrival in channel i, θ_t is the estimated time of interaction, r is the distance to the MCP channel i, v is the velocity of light in the medium, and t_f and t_r are the scintillator fall time and rise time respectively. The function acts as a prediction of measurement times for photons that propagate from a scintillation vertex.

4.1.5 Quantum Efficiency

The quantum efficiency (QE) is the probability that MCP will accept the photon upon an interaction. A plot of the photonis MCP QE was given in figure 3.5. However, as discussed earlier, we can calibrate for the differences in the individual modules using our laser and tuning the intensity to the single PE level. Once we make our quantum efficiency map we can apply it in the analysis.

4.2 Poisson Fitter

We use a poisson fit to estimate the energy of a particle interaction. The Poisson probability distribution [46] is given as:

$$f(k) = \frac{\lambda^k e^{-\lambda}}{k!} \tag{4.15}$$

where k is a discrete random variable, and λ is a parameter which happens to be equal to the mean and the variance and $k, \lambda > 0$. The Poisson model is useful for describing random variables that occur rarely in time and space and so they are widely used in physics and other experiments that involve the counting of scarce events. However, for our purposes we extend this discrete distribution to a continuous domain because the readout of photons in our experiment is not discrete. We can think of this new distribution as a type of gamma distribution however there is no perfect analog between a gamma distribution and a smooth Poisson distribution. By taking the logarithm of both sides and doing some rearranging we can extend our Poisson distribution to include continuous values:

$$f(k|\lambda) = e^{k*log(\lambda)-\lambda-log(\Gamma(k+1))} \tag{4.16}$$

Since the gamma function, $\Gamma(k+1) = k!$ can be interpolated between integers as:

$$\Gamma(k+1) = \int e^{-t} t^k dt \tag{4.17}$$

with which we were able to replace the $k!$ in equation 4.16.

Putting it all together we can interpret our Poisson fitter as follows. Our expected number of photons for one particular channel is:

$$\lambda_i = E * Y * l(z_i|\alpha)$$

or,

$$\lambda_i = E * Y * P_\Omega * P_\gamma * P_T * \Lambda_t * Q \tag{4.18}$$

and we let k_i equal the measured number of photons. E is the energy and is an additional parameter we need to fit for, and Y is the yield. For our particular scintillator the yield is 9200 photons/MeV (electron equivalent) [5]. A justification for using the continuous Poisson distribution is illustrated in figure 4.2.

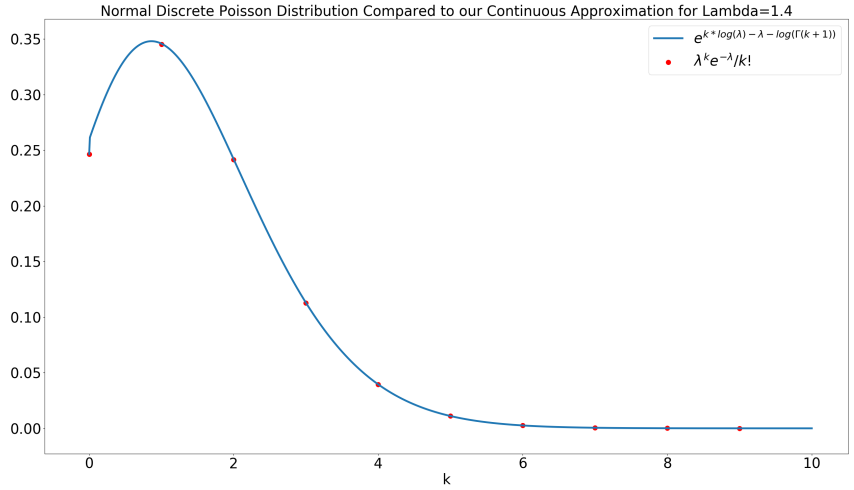

Figure 4.2: Comparison of the discrete Poisson distribution and the continuous version we use in our analysis. The continuous version is useful for us as our photon readout is given as fractional values

.

4.3 Cost Function

Our cost function is based on Bayes formula [47]:

$$p(\alpha|z) = \frac{p(z|\alpha)}{p(z)} p(\alpha) \tag{4.19}$$

where $p(\alpha)$ is the prior probability distribution or simply the 'prior'. The prior is a distribution that represents our belief of what a particular quantity is likely to be, in this case what the parameter space determining where, when, and with what energy an event will be. For our purposes we can consider the prior to be a limitation on the location (the dimensions of the cube), our energy estimate (PEs should be less than a thousand for the delayed signal for example), and the timing of our measurements (the timing of a single event should be of the order of a few nanoseconds at most). In addition, an antineutrino is just as likely to interact anywhere in the cube. In fact, we have found that locations of interaction points of almost any kind (aside from muons interacting in the medium which are usually leaving clear tracks entering from the top and exiting the bottom) to be randomly distributed in the medium. With these reasonable limits we can consider the prior to be a constant for antineutrino and neutron experiments. We measure p(z) directly (remember z represents our concrete measurements of time and location hits of photons) and each pixel is approximately identical (any differences arising from quantum efficiency is absorbed in equation). Therefore we can simply rewrite our cost function as:

$$p(\alpha|z) = \frac{1}{c}p(z|\alpha) \tag{4.20}$$

where c is a constant. Now that we have discussed the prior and defined all the necessary variables we can go ahead and define our cost function explicitly. The cost function we seek to maximize is a product of poisson likelihoods:

$$p(z|\alpha) = \prod_i f(k_i|\lambda_i) \tag{4.21}$$

where the product runs over all pixels or channels and z is the complete set of measurements and k_i and λ_i are the detected and expected number of photons respectively as described previously. The measurements (z) consist of the actual photon counts and photon arrival times for each pixel.

4.4 Mixed Probability Distribution

For the purposes of neutron recoil fitting we choose to used a mixed probability distribution. This is necessary due to the fact that the light from multiple neutron recoils off the protons in the scintillator produce mixed signals of light, where each flash of light is not well separated in time and space. So if our likelihood $p(z|\alpha)$ represents a mixed probability distribution we can write:

$$p(\alpha|z) = \prod_j \sum_i w_i p(z_j|\alpha_i) p(\alpha_i) \tag{4.22}$$

where the product is taken over all channels (1536 for a fully populated mTC), z_j is the measurement made at channel j, α_i is ith point source we are trying to estimate, w_i is the weight of the observed distribution component, and $p(\alpha_i)$ is the prior for the ith point source estimator which we can consider to be a constant for the same reasons given earlier. We leave the prior in the equation as a reminder that we enlist a uniform distribution for events in terms of location (must be within the cartesian coodinates of the cube) and energy (which depends on the interaction we are trying to observe). The weights have only one constraint which is that the must sum to unity:

$$\sum_i w_i = 1 \tag{4.23}$$

4.5 Bayesian Criteria Information

The Bayesian Criteria Information (BIC) is an extremely useful comparison method for statistics [48] . When we discuss neutron directionality analysis in our experiment we will make heavy use of the BIC. It is a method of normalizing two different models in terms of their different measurement spaces (or models that use a different number of parameters) in order to compare their relative likelihoods. In general, the BIC method penalizes likelihoods that contain a larger number of parameters. When a signal appears as a mixture

of a number of finer signals which we need to deconvolve, the method gives us a chance to compare similar models which vary in terms of the number of parameters (in our case the number of scintillation points). The BIC (which we seek to minimize) is given as:

$$BIC = -2 * ln(p_z|\alpha) + n_\alpha * ln(n_z) - n_\alpha * ln(2 * \pi) \tag{4.24}$$

where n_α is the number of parameters we need to estimate and n_z is the number of measurements. The BIC can be used to identify the number of recoils a neutron experiences as it traverses our scintillator. So we can in principle use the BIC to help identify neutrons that scatter at least twice in the medium from other particles and we will discuss this more in chapter 9. In practice, we assume that the neutron can 'bounce up to 5 times (a number based of Geant4 simulated data) and we fit for up to 5 bounces. We do this as it is important to isolate all bounces in order to maximize the resolution of the first two bounce locations. The BIC with the lowest minimum among the different models wins out and indicates how many actual recoils were best fit.

4.6 Some Verifications of Our Model

In this section we will provide some verifications of our reconstruction techniques. We will offer a couple of qualitative examples followed by a quantitative one. In the next chapter we will examine the model further with

an emphasis on the probability mixture technique used in our neutron recoil studies.

While the laser tests provide efficiency and gain information that we can employ, they also offer us an experimental verification of our reconstruction techniques. In figure 4.3 we see a reconstruction of actual laser pulses in the mTC. The pulses originate on the top side of the mTC face and the photons create scintillation light in the mTC. The laser light should behave as a point source emanating near the top face and our reconstruction effort shows agreement.

In figure 4.4 we see a simulated muon track on the left and the reconstructed track on the right. Clear entry and exit points are shown and the agreement is shown to be excellent.

As a quantitative example of our fitting model we present a cobalt-60 simulation (source placed on the middle of top surface of the cube) and reconstruction effort in figure 4.5. We see excellent agreement in the x,y,z positions and a linear relationship in the truth vs. fitted energies with resolution suffering at higher energies. This is due to the small volume of the cube where higher energy particles tend to leave the cube without depositing all their energy. We see that we can expect about 10-15% energy resolution in the range of 0-1.2MeV. A model based calibration was made using the bottom right plot (a 5th order polynomial relationship between E_{fit} and E_{true}) and applied to the energy error plot located in the top right. We see that after the calibration is applied the errors in energy are nicely centered

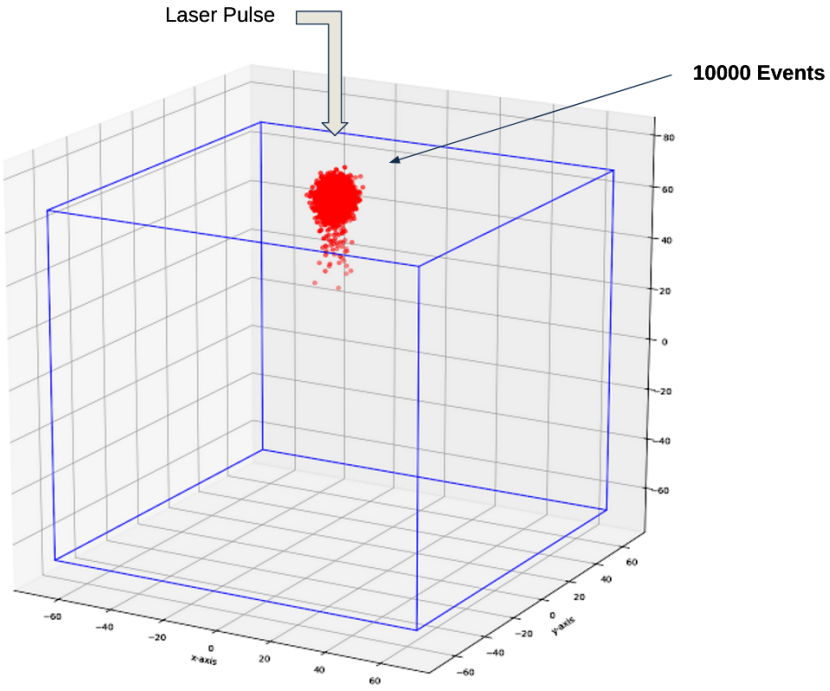

Figure 4.3: An experimental verification of our fitter model. Laser light is shown downward from the top face of the mTC creating scintillation light. Reconstruction of scintillation vertices show up in the logical location
.

around zero.

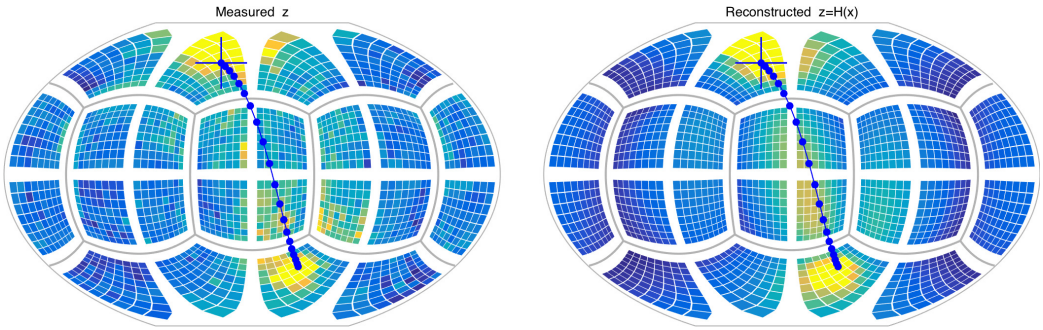

Figure 4.4: A muon track simulation and reconstruction comparison. On the left we have the simulated track and on the right is the reconstructed track showing excellent agreement. Image from our paper [4].

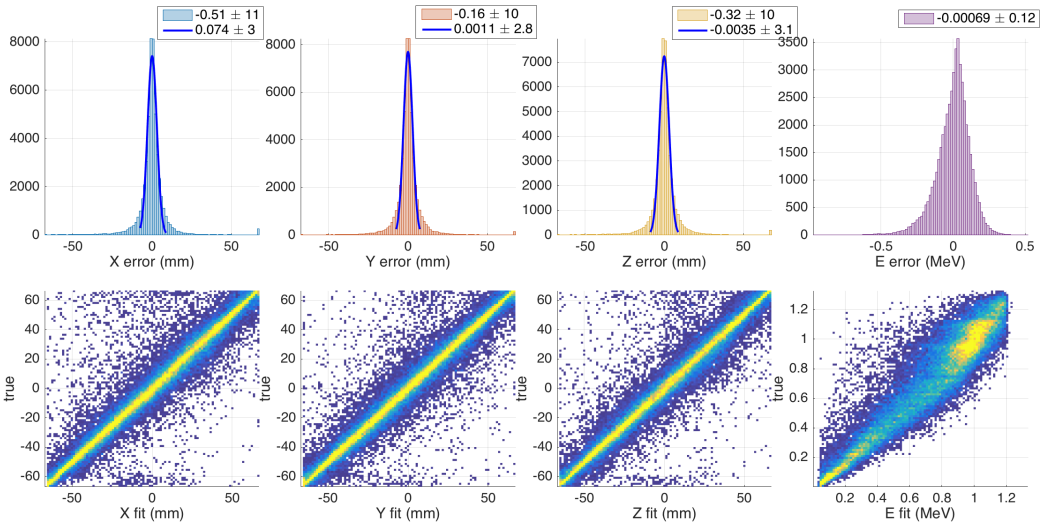

Figure 4.5: Fit of a simulated cobalt-60 source for position resolution, and energy resolution vs energy. Credit to [6]

.

Chapter 5

Simulations of Neutrinos and Neutrons in the mTC

In this section we display some of our simulations of IBD and neutron directionality in the mTC. The chapter aims to give us a feel for what to expect when we set up our experiment in front of the test reactor at NIST and an appreciation for what our ability will be to track neutron direction.

5.1 IBD Simulations

We are interested in detecting electron antineutrinos through inverse beta decay, shown again here for your convenience:

$$\overline{v}_e + p \rightarrow n + e^+$$

As noted in the second chapter, this is the same reaction used by the Reines and Cowan experiment in 1956 and many other experiments since then. An electron antineutrino emitted from a nuclear reactor interacts with a proton in our scintillator producing a neutron and a positron. The cross-section for this reaction is $\sigma_tot = 5 * 10^{-43} cm^2$ at a neutrino energy $E_v = 2.3MeV$ and an energy threshold of $E_v = 1.806$MeV in the lab frame where the proton is at rest [4]. There is a characteristic time between the prompt signal (positron and electron annihilation) and the delayed signal (neutron capture on Boron) which helps us select our windows of interest. The signature energy of the gamma that can result from the Boron capture also helps to identify the reaction. The positrons scatter isotropically and the neutron carries away majority of the neutrino energy while the positron carries the majority of the energy. This means that if we can identify the direction of the neutron by recording the neutron recoils we can identify the incoming neutrino direction. We will outline these procedures in the next sections. All simulations shown in this dissertation are combinations of Geant4 and self-built Monte-Carlos using either Matlab or Python and reconstructions are done in Matlab or Python.

5.1.1 Prompt Signal

As noted above, the prompt signal for our neutrino detection portion of our experiment is the positron annihilation. The energy of the signal is comprised of a short Cherenkov track (approximately 1cm), the two gammas

of $E_\gamma = 511$MeV each, and any other electrons the positron may interact with as it propagates. The prompt signal generates from around a several hundred photoelectrons anywhere upwards to a few thousand in the mTC as we can see in the top plot of figure 5.1. The long tail which increases with antineutrino energy is due to the high energy positrons leaving the mTC before they have deposited all their energy. Therefore our energy resolution suffers as the energy of the antineutrino energy increases. Again, our energy resolution is limited by the small size of the mTC. The length of the positron track is about 1cm but as noted, for higher energies (above the 1.8MeV threshold for production) the positron can leave the target thereby giving an underestimate of the true energy. Another problem is correctly estimating the energy of the two gammas (511 keV each). On average the gammas deposit about 1/3 of their energy into the scintillator but this energy varies greatly from event to event. Therefore any concept of a concrete prior for this event is not useful. In figure 5.2 we have a Monte-Carlo showing the photon yield vs vertex location showing that for the prompt and delayed signals we lose resolution near the walls of the cube. Again this is due to the small size of the mTC where the gammas tend to escape before depositing all their energy. This is where a detector such as Kamland can outperform us; Its large size circumvents this problem because the total energy of the gammas is consistently deposited in the scintillator.

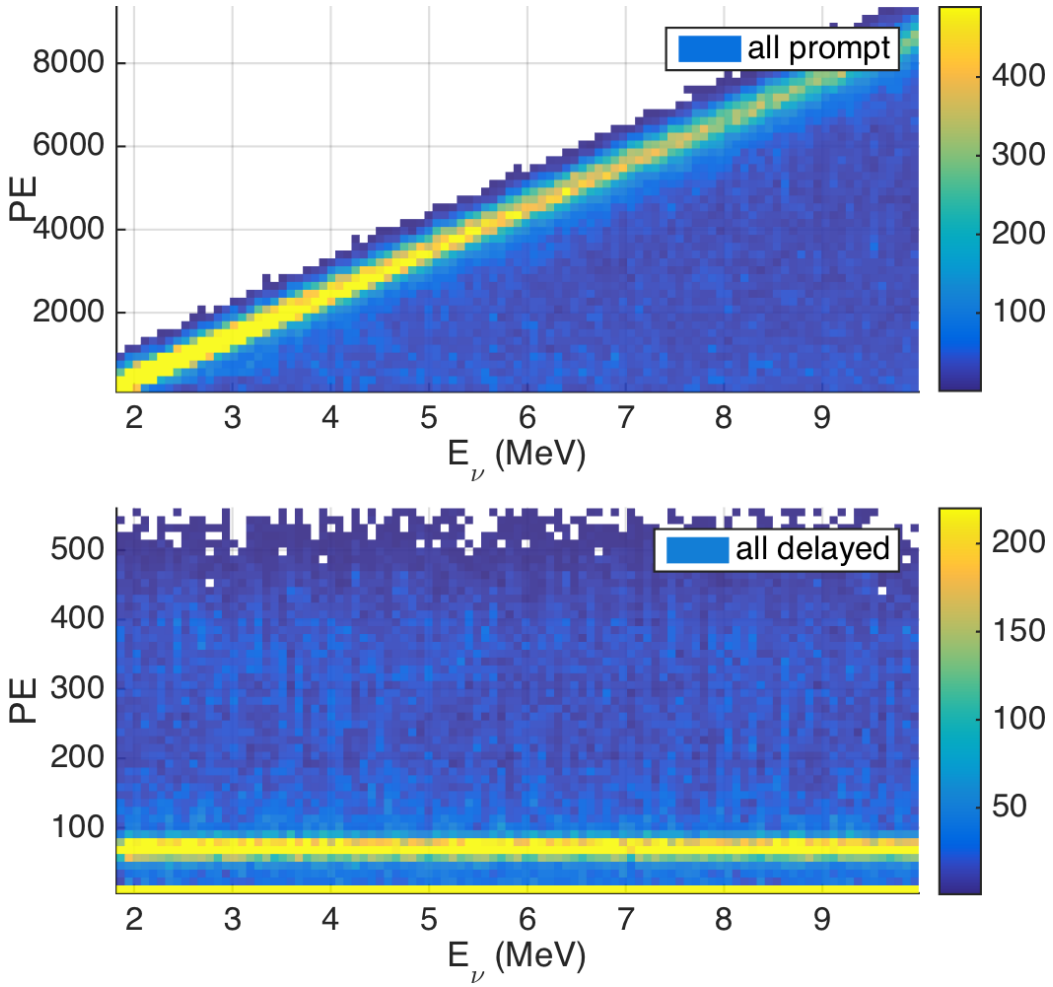

Figure 5.1: In the top figure we have a Monte-Carlo simulation of the photon yield for positron annihilation in the mTC (prompt event). The long tail that grows with increasing energy is due to the high energy positron leaving the mTC before all its energy can be deposited. The bottom figure is a simulation of the photon yield for the delayed event. The 478 keV gamma produced from the neutron capture produces on average about 90 photons. The long tail is due to random nature of the Compton scattering event. Image from our paper [4]

.

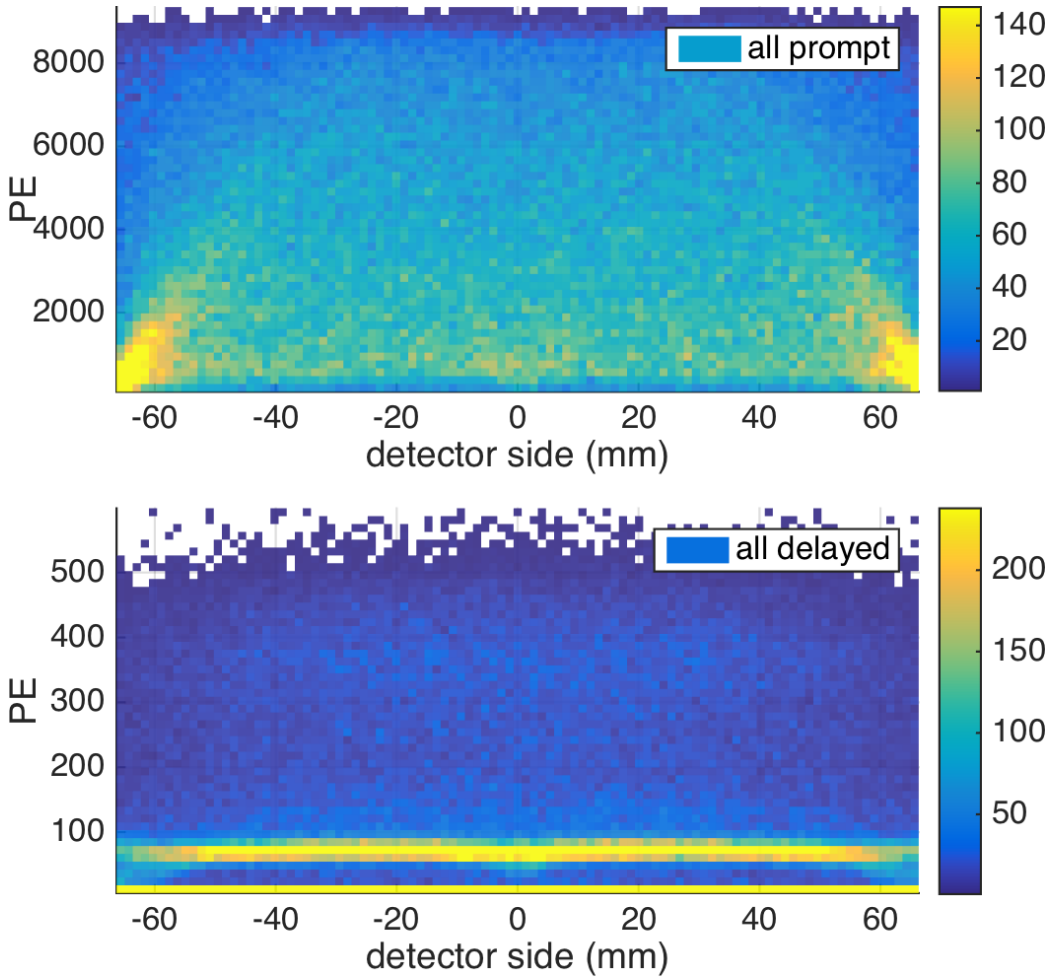

Figure 5.2: In the top figure we have a Monte-Carlo simulation of the photon yield for positron annihilation with respect to vertex location (prompt event). We notice a tendency for an underestimation of the energy as the vertex approaches the walls of the cube. The bottom figure is a simulation for the delayed event and it shows the same trend. Image from our paper [4] .

5.1.2 Delayed Signal

The neutron produced from the IBD event bounces elastically of the protons (and occasionally carbon) until it thermalizes and is captured by the boron

^{10}B embedded in the scintillator. The primary reaction for neutron capture is [49–51]:

$$\begin{aligned} n + {}^{10}\mathrm{B} \rightarrow {}^{7}\mathrm{Li}(1015\ \mathrm{keV}) + {}^{4}\mathrm{He}(1775\ \mathrm{keV}), \quad &\sim 6\% \\ \rightarrow {}^{7}\mathrm{Li}^{*} + {}^{4}\mathrm{He}(1471\ \mathrm{keV}), \quad &\sim 94\% \\ \hookrightarrow {}^{7}\mathrm{Li}^{*} \rightarrow {}^{7}\mathrm{Li}(839\ \mathrm{keV}) + \gamma(478\ \mathrm{keV}) & \end{aligned} \tag{5.1}$$

The cross-section for neutron capture on boron as well as the linear attenuation coefficient has been well studied and for a completely thermal neutron ($E = .025eV$) the cross section is 3836 barns [4]. The resulting gamma deposits its energy via Compton scattering. The average time for neutron capture (∼10µs) and distance travelled (∼4cm) is shown in figure 5.3 for a series of simulated IBD events. For an analytical explanation of the results shown in the figure please refer to our paper [4].

5.2 Simulations for Neutron Directionality

In chapter 4 we discussed the method of mixed distributions and the BIC used to distinguish the multiple neutron recoil points in the mTC. To illustrate this method for neutron tracking in a small single solid volume we present simulated data of a flux of neutrons through our scintillator and our reconstruction of these events. A flux of 50000 0-10 MeV neutrons were directed downward through the top face of the mTC and 11553 of those were

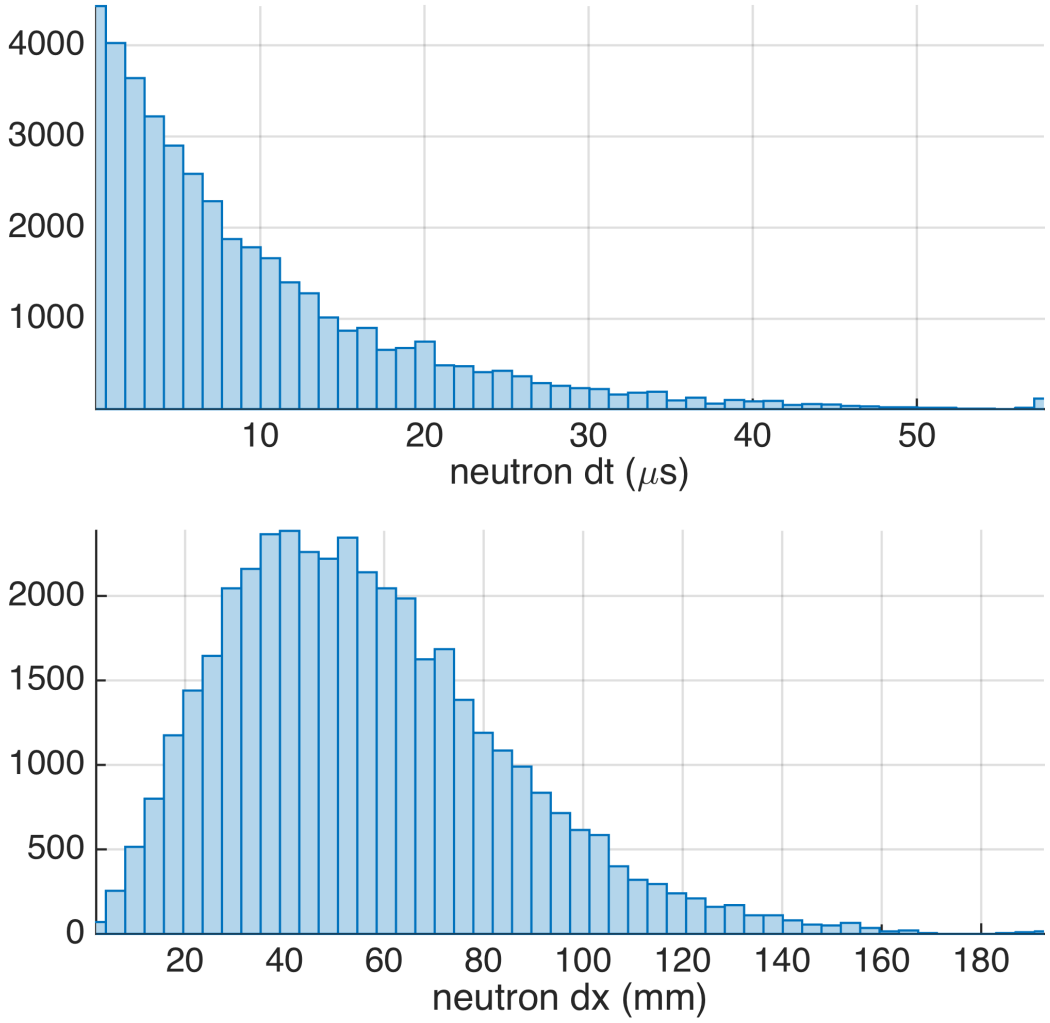

Figure 5.3: Shown here is a neutron distance and time frequency plot for IBD events. In the top figure we have a simulation of the production to the thermalization and capture time of the IBD neutron in the mTC. The bottom figure shows the distribution of travel distance for the neutron produced in the mTC. Image from our paper [4]

.

successfully fit. A timing histogram of a typical event is shown in figure 5.4.

The figure illustrates the difficulties of separating the neutron recoil signa-

tures with respect to time and energy. It is worthy to note that the image presented is a rare case where the two separate bounces are minimally visible to the naked eye. In most cases we would have a situation such as the one shown in figure 5.5, where the separation of the neutron recoils is not apparent and we must deconvolve the data using excellent time tracking and a clever analytic model. Again, multiple neutron scatters are typical and this can complicate our signal greater. As a consequence, even though we are only concerned with the first two bounces in order to determine the direction of the incoming neutron, it is important to isolate all bounces (up to 5) in order to maximize the resolution of the first two bounce locations.

5.3 Candidate Efficiency and ID

Due to the small size of the mTC, not all the neutrons deposit their entire energy inside the cube and capture on boron. Additionally, some lower energy neutrons will not give off enough light to track the recoils regardless of whether they capture on the boron. Another crucial matter is that gammas can mimic neutrons with respect to energy. With respect to the last point, fortunately the structure of our fitter has a built in rejection of gammas under circumstances that are beneficial to our purpose. When attempting to fit gammas, any attempt to include any more than a single point is rejected by the BIC comparison test. This can be explained by noting that gammas do not produce a burst of photons (first recoil) and then after a delay a second

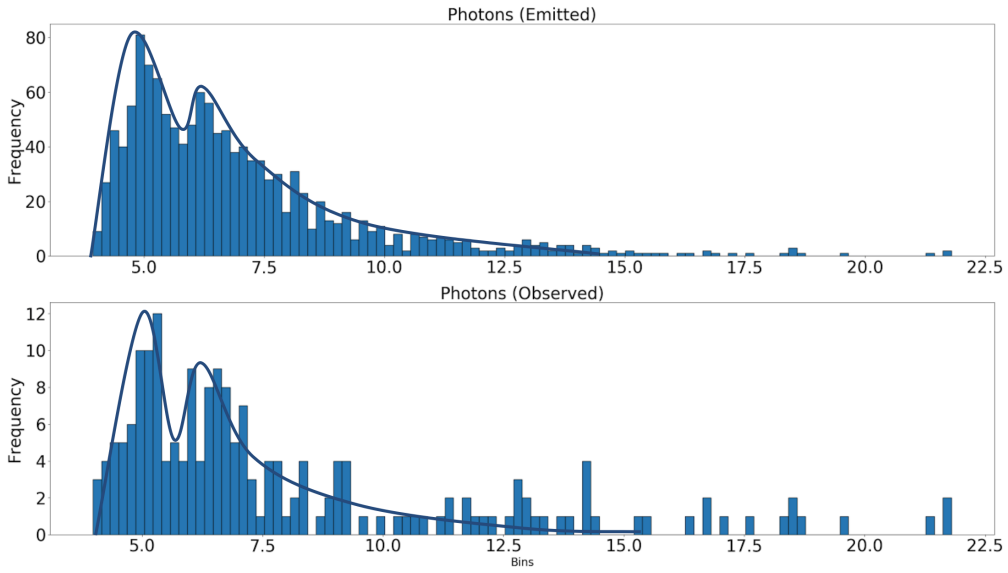

Figure 5.4: A simulation of a double neutron recoil event taking place in our scintillator. This particular event was chosen to illustrate the two recoils visually. Typically neutron recoils are not visible by the naked eye. The recoil shown here is approximately 2ns apart. We see that the light signals from both events overlap.

burst (second recoil). Rather, the gamma travels at the exact same speed of the photons produced via scintillation. An attempt to fit 50000 0-3 MeV gammas resulted in the BIC rejecting all fits involving any more than one single point source except for 3 accidentals which were rejected due to their unrealistic velocities. In addition, the laser fit shown back in chapter 4 in figure 4.3 utilized the BIC which only yielded single point sources for all 10000 events and rejected any fits for multiple recoils. This is a great experimental test as the laser acts as a point source maximally. Muons are also easy to reject as they have a high energy signature which make it easy to implement

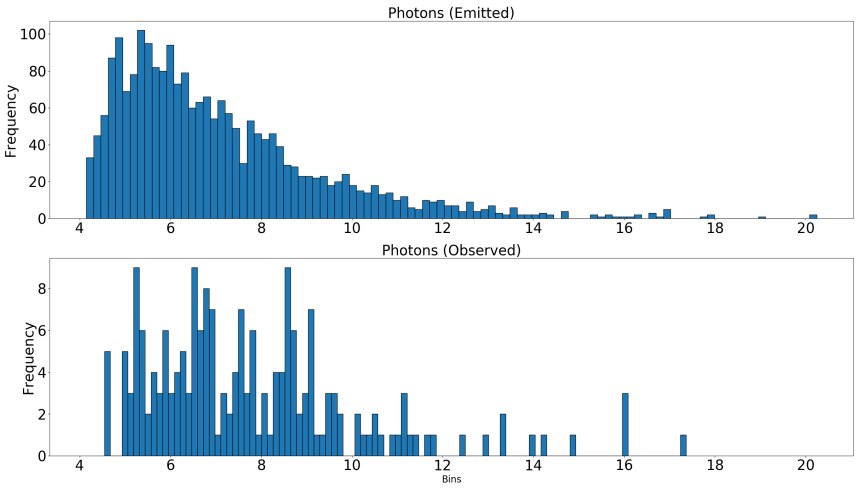

Figure 5.5: A simulation of a double neutron recoil event taking place in our scintillator. This is more representative event showing that the recoils are usually not clearly visible to the naked eye and must be resolved analytically.

cuts based on the photon yield. In order to maximize our angular resolution we implement the following candidate cuts shown in table 5.1.

A qualitative explanation of why our model rejects multiple scatters from gammas in our medium is given in figure 5.6. We see that the time between gamma scatters is too short for our detector and model to resolve. As a result the model will make a best guess as to the location in time, space and energy for a single scintillation vertex for gammas regardless of the amount of scatters that occur.

The results of our simulation and reconstruction neutron based work are given in the following figures. We fit approximately 20% of the 50000 simulated neutron events in the mTC. A simulated histogram of neutron speeds

Table 5.1: Table of Cuts

Only a limited number of cuts is required to get good resolution from our fitter and those cuts are listed here.

PE's	> 20
PE's	< 1000
$t_2 - t_1$	$> 1ns$
$\|P2 - P1\|$	$10mm$
$\|v\|$	$> 2mm/s$
$\|v\|$	$< 20mm/s$

for neutrons which recoil at last twice in the scintillator is shown in figure 5.7. An average speed between recoils is 7.5 mm/ns with a standard deviation of 6.8 mm/ns. This allows us to make reasonable cuts to our reconstructed data in terms of speed alone. In figure 5.8 we show the angular resolution based on a calculation of $cos(\theta)$ where θ makes the angle between the fitted $\overrightarrow{P_2 - P_1}$ vector and the true direction. We see in the figure a clear preference in the $cos(\theta) = 1$ direction. As plots of directionality based on $cos(\theta)$ can be deceiving we also include a plot of the angle θ itself in figure 5.9. In this plot we see an average calculated θ value of (1.3 +/- .7) radians. Clearly we are in the correct hemisphere based on the average however we can do alot better in analyzing directionality with our data by constructing the average directional vector. In figure 5.10 we see the reconstructed fits for the x,y,z points for both the 1st and second bounces. We see that the fits all centre around zero. In general the second bounce fits have a slightly larger standard deviation then the first bounce which is expected. Surprisingly the standard deviations are comparable. Part of the reason for this is that the fitting

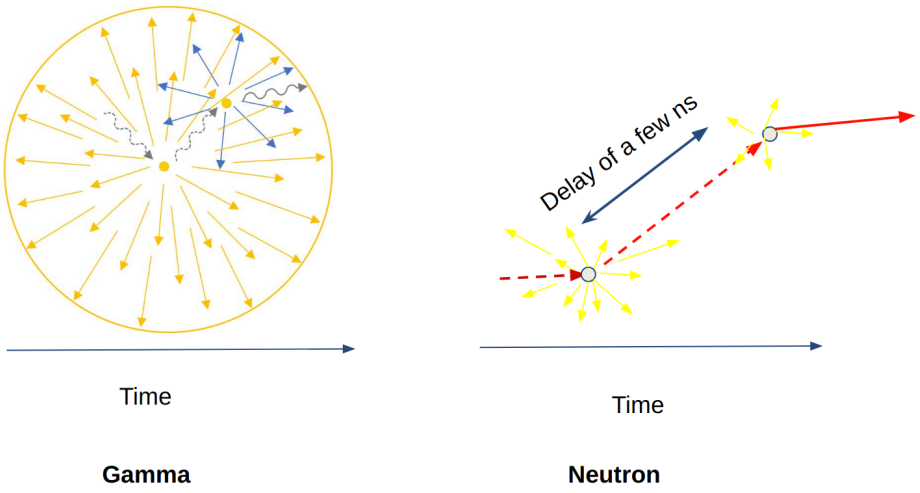

Figure 5.6: Shown here is a figure which qualitatively explains how our model rejects double scatter events for gammas. The gamma compton scatters twice creating two outgoing scintillation spheres. As light takes approximately a nanosecond to traverse the cube, the scatters are separated in time by only a fraction of a nanosecond. The gamma itself is travelling at the same speed as the photon sphere is expanding and our model will likely fit for a single recoil at a weighted average between the two scintillation points. For the neutron recoils the average time between bounces is approximately 2 nanoseconds. The slower moving neutron allows for the early light from the first recoil to reach the pmts before the first light produced from the second recoil. As shown in figures 5.4 and 5.5, the light arriving from both neutron recoils will always be mixed due to the scintillator decay time.

technique employed in our analysis is efficient, but another reason is that the fitter tends to prefer recoils which are comparable in energy. Fits for events where there is a large bounce followed by a small secondary bounce tend to be overlooked (but not always) by the fitter as a single recoil. In this case photons from the first high energy recoil 'blanket out' the small emission of light from the low energy recoil occurring a short while later.

Using our point fits for the x,y,z's for the first and second bounces we can construct the average directional vector and see how well the average direction lines up with the true average directional vector. In figure 5.11 we plot these two vectors and as one can see they line up very well. The cube is not to scale here and the vectors are magnified. The simulated vector in black has the coordinates [-.001,.194,-6.940]mm and the reconstructed vector in green has the coordinates [-.108,-.157,-5.138]mm. The overlap of the the two vectors is excellent and the angular resolution $cos(\theta)$ is .998 +/-.002 corresponding to an angle difference of (-.1,.13) radians or (-5.7,7.4) degrees at a 99.96 percent confidence limit.

point

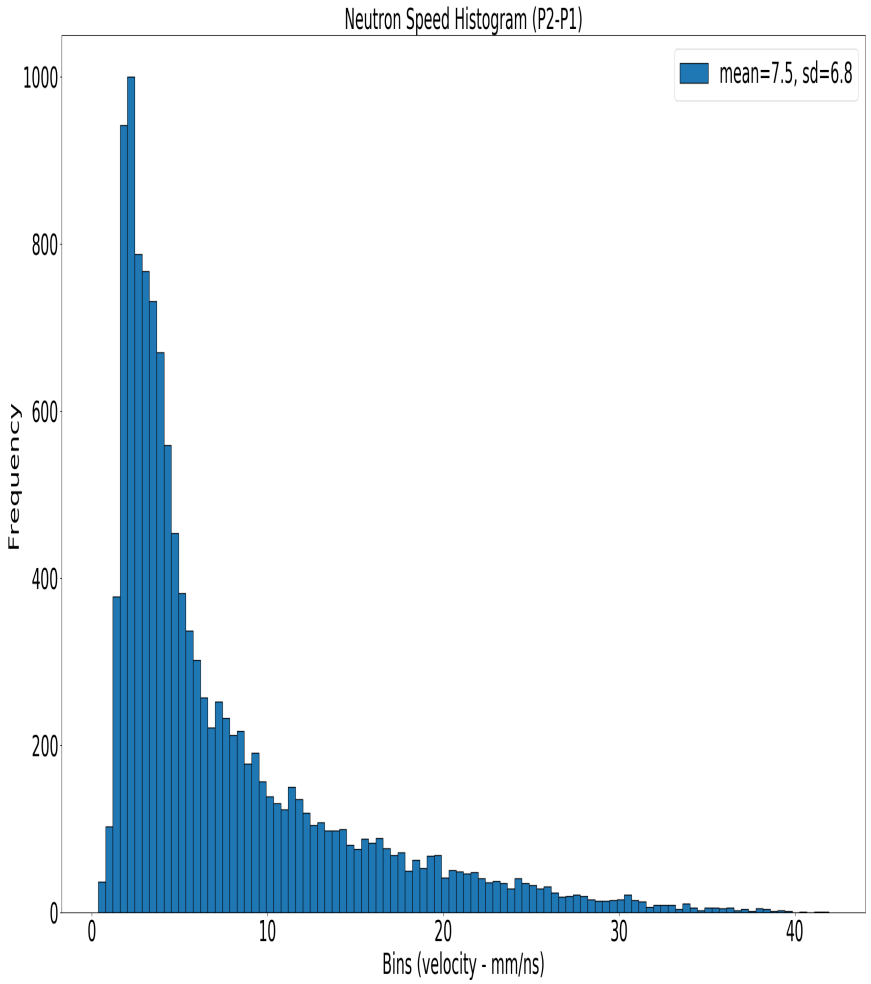

Figure 5.7: Shown here a simulated histogram of the neutron velocities between the first and second recoils. The data here allows us to make cuts in our fitting that will eliminate unreasonable velocities in our reconstruction.

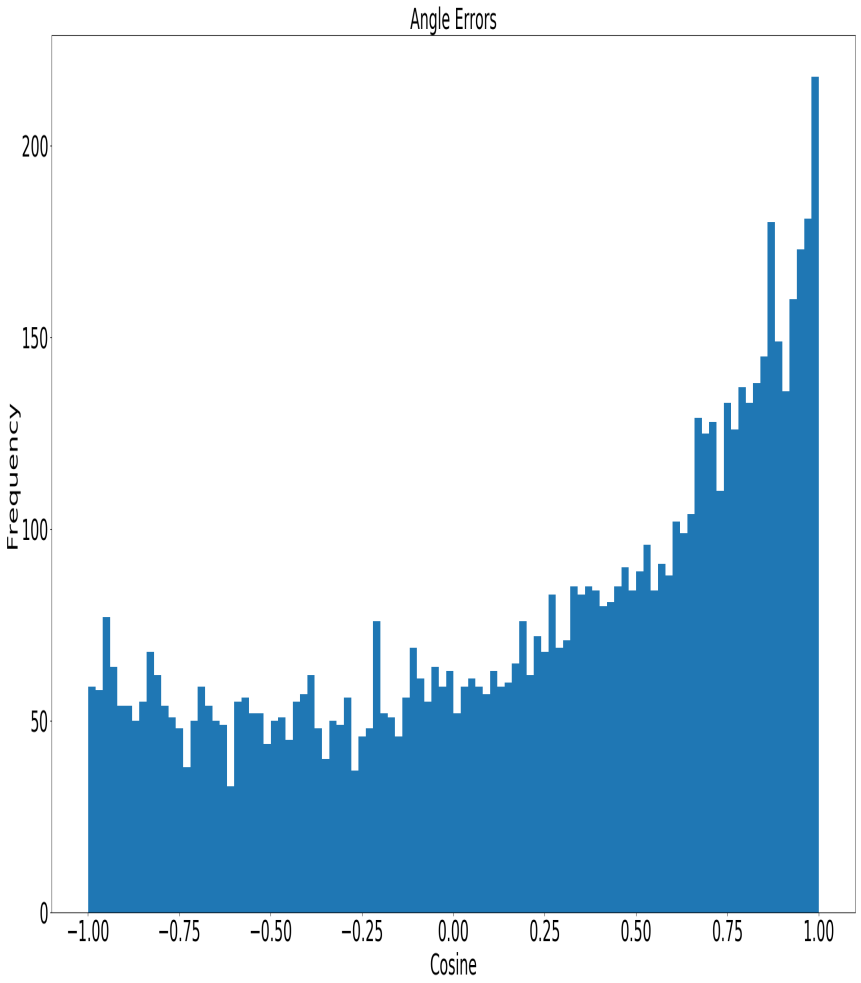

Figure 5.8: A histogram showing the angular errors with respect to $P_2 - P_1$ vectors. Angular resolution per event is understandably poor and a large amount of statistics is needed for accurate direction.

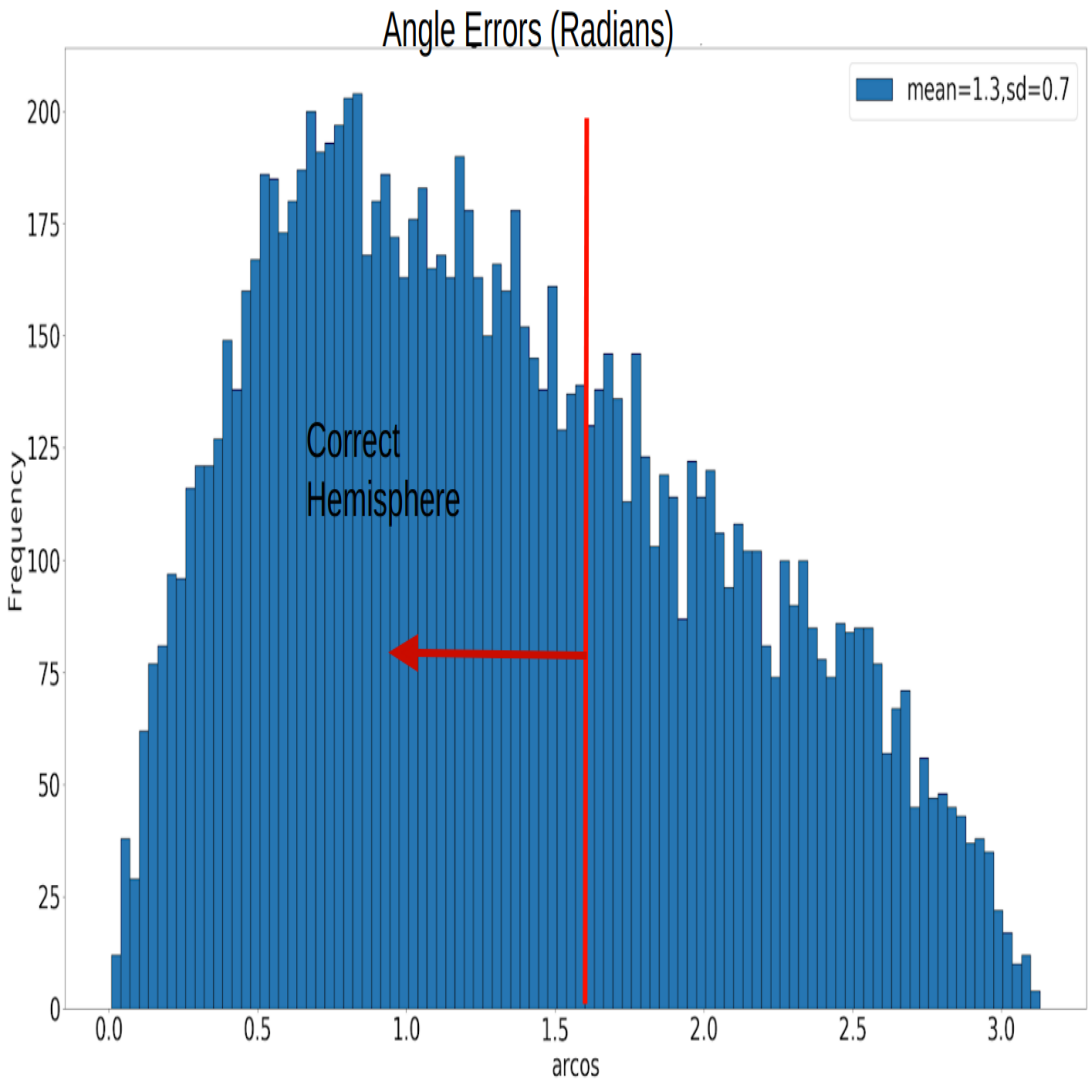

Figure 5.9: Shown is an angular resolution histogram for the angle θ. Clearly the distribution has a heavier presence in the correct hemisphere. Angular resolution per event is not great however and a large amount of statistics is needed.

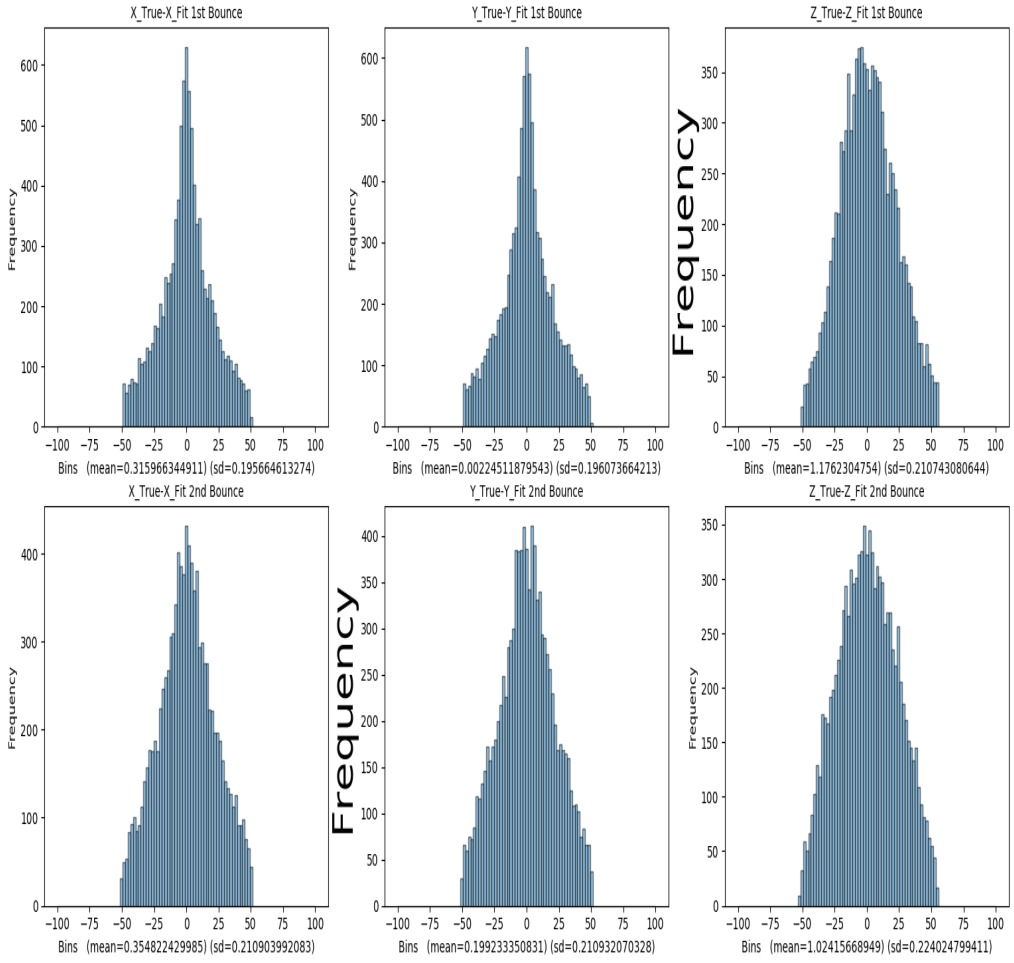

Figure 5.10: Plots of the 11553 successful reconstructed simulated data fits for the x,y,z positions of the first and second bounces. The data peaks nicely around zero in each plot.

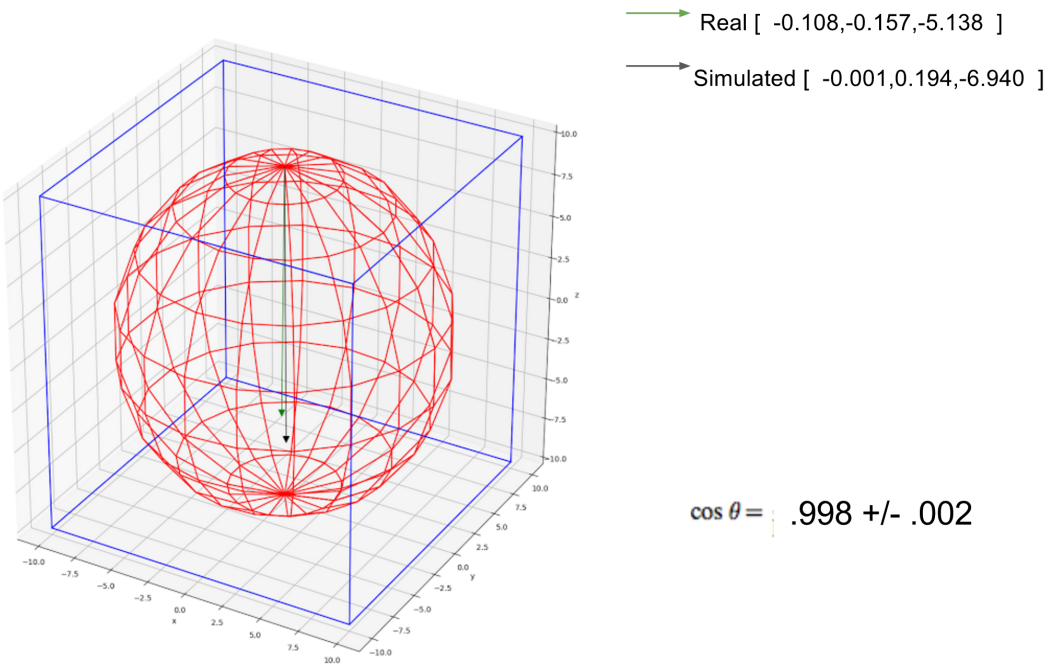

Figure 5.11: The simulated average directional vector (black) is plotted against the fitted average directional vector (green). The vectors are scaled to the average range between the first two recoils. Clearly there is excellent agreement between the two vectors. $cos(\theta)$ is .998 +/-.002 corresponding to an angle difference of (-.1,.13) radians or (-5.7,7.4) degrees at a 99.96 percent confidence limit.

Chapter 6

The mTC at NIST

In this chapter we will discuss our experimental setup for antineutrino detection at the NIST Centre of Neutron Research (NCNR).

6.1 The Setup

The mTC was deployed to the NIST NCNR in the summer of 2015 where it began taking data. The centre houses a 20 MW split-core test reactor. The core consists of 30 fuel elements which each contain two segments of highly enriched uranium U_3O_8/Al (^{235}U, 93% enrichment). The two segments, each of which are 27.9cm in height and 1.12m in diameter, are separated by a 17.8 cm air gap. This fuelless gap serves as a flux trap which minimizes fast neutrons and gammas from entering into the neutron beam lines and maximizes the collection of slow neutrons. The overall shape of the compact

core and the mTC set up relative to it is shown in figure 6.1.

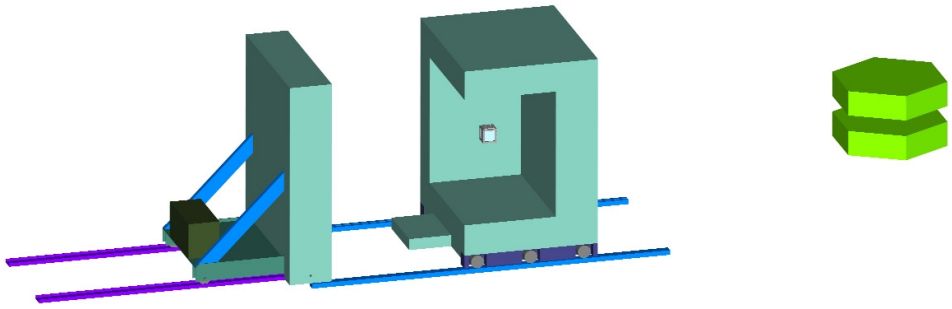

Figure 6.1: A CAD drawing of the mTC set up at NCNR. The split core is shown along with the mTC with shielding approximately 5m away. Image from our paper [4]

.

Full Monte Carlo N-particle (MCNP) simulations of the core are available to onsite collaborations. [4]. For a thermal power of 20 MW_{th}, we have an estimated number of 6 $\bar{\nu}_e$ produced per fission and $\sim$ 1.5 $\bar{\nu}_e$ are above IBD threshold. Knowing the energies released per fission of ^{235}U and ^{238}U we can estimate the total number of neutrinos produced at the reactor core to be $\sim 4 \times 10^{18}$ s^{-1} $\bar{\nu}_e$. This corresponds to an approximate flux of $\sim 1.1 \times 10^{12}$ cm^{-2} s^{-1} $\bar{\nu}_e$ at $\sim$ 5 m away from the center of the reactor core where the mTC was located. This corresponds to a few antineutrino IBD interactions in the mTC scintillator a day. Figure 6.2 shows the relative

antineutrino flux at baseline from the core.

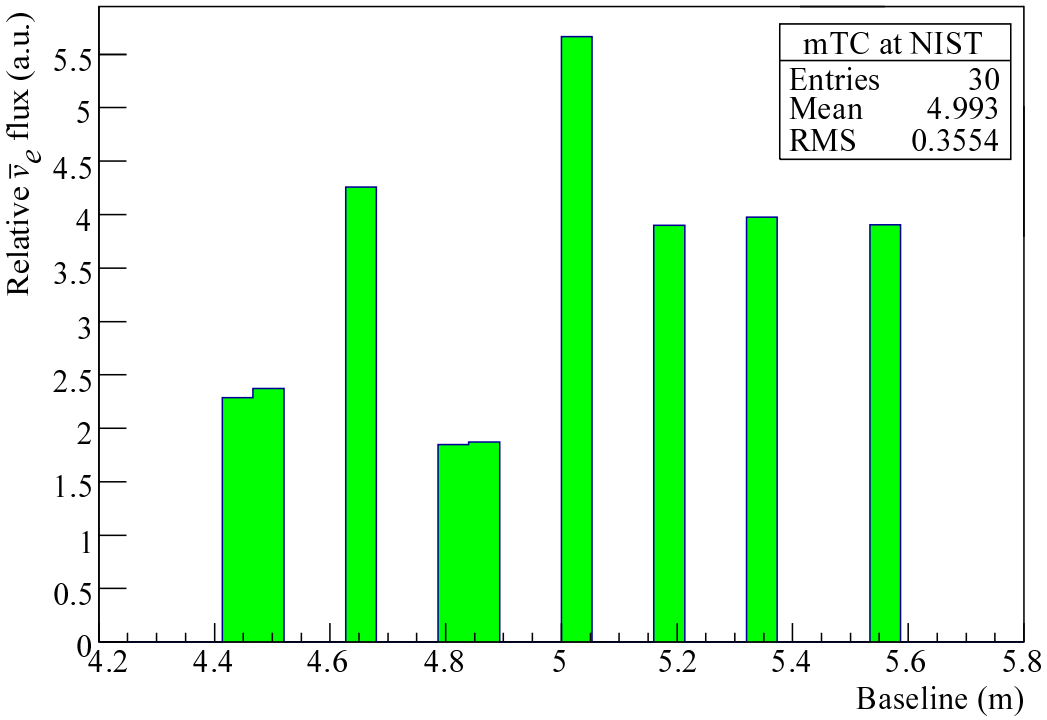

Figure 6.2: Relative distribution of $\bar{\nu}_e$ flux as a function of baseline from a nominal mTC position to each fuel element in the core. The mean source location of flux is at ~ 5 m and the effective spread is 0.36 m, or an inherent smearing of about 7 % on the baseline. Specifics of this distribution will vary by fuel loading conditions [4]

.

We can analytically arrive at the expected number of antineutrinos that will react with our scintillator using the following equation [4]:

$$N_{\bar{\nu}_e}^{\text{obs}} = \frac{N_p}{4\pi L^2} \int \epsilon_{det} P(\bar{\nu}_e \to \bar{\nu}_e) \frac{d\sigma(E_{e^+}, E_{\bar{\nu}_e})}{dE_{e^+}} \times \frac{d^2 N_{\bar{\nu}_e}(E_{\bar{\nu}_e}, t)}{dE_{\bar{\nu}_e} dt} dE_{e^+} dE_{\bar{\nu}_e} dt, \tag{6.1}$$

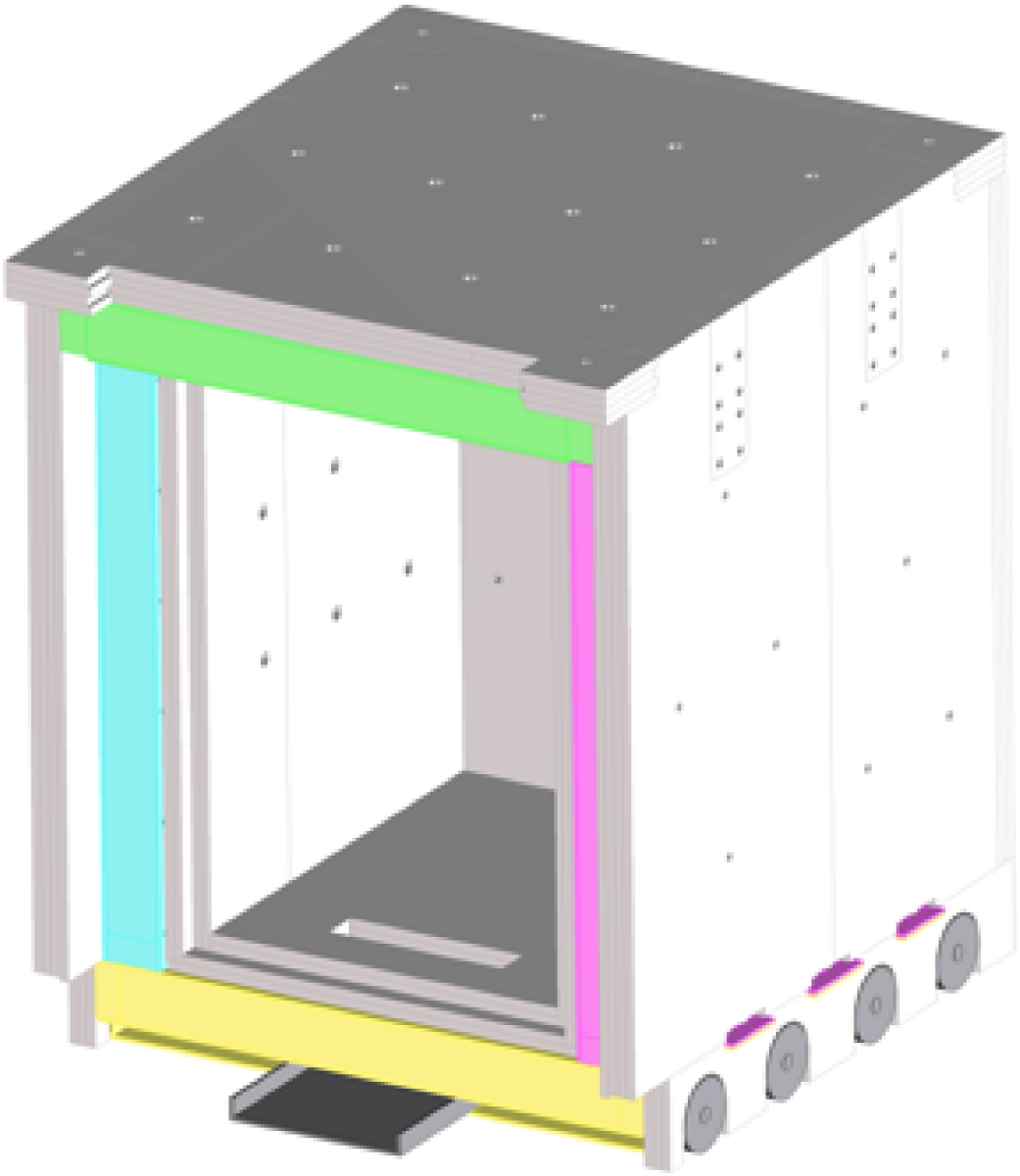

Figure 6.3: CAD drawing of the walk-in radiation shield used in our experiment. Image from our paper [4].

where N_p — number of hydrogen atoms in the scintillator ("free protons"); L — distance between production and detection points of the antineutrino, ϵ_{det}

— detector efficiency $\sim$ 30 % based on MC simulations for IBD detection in the mTC; $P(\bar{\nu}_e \rightarrow \bar{\nu}_e)$ — survival probability of electron antineutrino; [37, 43] and $\frac{d\sigma(E_{e^+}, E_{\bar{\nu}_e})}{dE_{e^+}}$ — differential cross-section of the IBD process as a function of positron energy E_{e^+} and antineutrino energy $E_{\bar{\nu}_e}$ [52]. The number of antineutrinos we expect to detect with 30% detector efficiency is approximately one per day [4].

6.2 Backgrounds

In this section we discuss the general background challenges the mTC faces. We discuss the general background problem first and then we will focus on the NIST specific problems.

6.2.1 Cosmic Ray Backgrounds

Comic rays produce inescapable hadron and lepton showers which interfere with IBD detectors. About 2 meters of water equivalent (2 mwe) is enough to reduce the most prominent hadron and electromagnetic components and luckily this is approximately the equivalent protection available for the reactor at NIST. High energy muons unfortunately have great penetrating depth and themselves can produce showers that mimic IBD events. Unfortunately muons also interact with the material used in our shielding which then can create hadron/lepton showers. Hence shielding is a double edged sword. The mean energy of muons at sea level is about 2GeV and we expect a muon rate

of 1Hz through the mTC. A muon can (about 10 percent of the time) create knock-on electrons which can create a mixture of scintillation and Cherenkov light. Products of cosmic ray muons can be a background for IBD events although most of these can be eliminated quite easily using various cuts based on time and energy. There are however two products that have shown themselves to be a nuisance and they are the isotopes ^{8}He and ^{9}Li. They have lifetimes on the order of one second and decay by beta emission into unstable-nucleon daughters which have the potential to mimic IBD events. Luckily our Geant4 simulations show that this will occur less than one time a year in our detector [4]. Figure 6.6 shows the cosmogenic isotope production yield due to muons passing through 10m of EJ-254 scintillator and figure 6.7 shows the average yield of all non-photon secondary products per unit muon track length per unit medium density versus energy. Figure 6.6 and Figure 6.7 show that ^{8}He and ^{9}Li will not be an issue in our experiment.

6.2.2 Backgrounds at NIST

Extensive background studies have been done at the NIST reactor location. The PROSPECT group did a background study at the precise location that the mTC was placed [53]. In figure 6.8 we see the gamma spectrum (reactor on and off) at the mTC location. Some of the higher energy gammas are mainly a result of neutron capture on shielding materials. We can see that careful shielding is of of the upmost importance for a sensitive IBD detection experiment.

6.2.3 The Cave

A multi-layered shield was built to encase the mTC and shield it from gammas and neutrons which will create backgrounds for our experiment. A CAD drawing is shown in figure 6.3 and the actual cave is shown in figure 6.4. The layers from outward to inward are listed as follows [4]:

1. 10 cm of 5% borated polyethylene sheet
2. 1 cm of A36 steel plate
3. 15 cm of steel shot and paraffin wax mixture
4. 1 cm of A36 steel plate
5. 10 cm of 5% borated polyethylene sheet
6. Interior cavity for housing the mTC and associated electronics (dimensions 1 m $\times$ 1.2 m $\times$ 1.5 m)

The borated polyethylene sheet acts as neutron absorber while steelshot and wax serves to absorb both gammas and neutrons. The multi-layer design was chosen as to remove potential line of sight and the isolated design helps to inhibit the transport of thermal neutrons which exhibit gas like properties. A Geant4 simulation was done to determine the effectiveness of the shield and these studies in turn helped us decide on the final layer design. A particle flux based on the best data available at the location of the mTC near the reactor, composed of muons, gammas and neutrons was incident on the shield and the flux inside the inner volume was calculated. The results are shown in Table 6.1. Unfortunately muons are not effectively negated by the shielding

but for neutrons and gammas the attenuation factor is agreeable. For more material regarding the cave, please refer to our paper [4]. Also a paper is being written at this time on the cave and will hopefully be published sometime in the next year.

Table 6.1: Particle fluxes through the mTC volume with and without the shielding cave present. The neutron flux is dominated by near-thermal neutrons hence the large attenuation factor. Muons are incident on the mTC at a rate of less than 3.5 Hz, and are not significantly affected by the shielding cave.

	normal	shielded	normal	shielded	attenuation
Type	#/mTC/s		#/cm^2/s		%
Neutron	3391	0.082	4.0	9.7×10^{-5}	99.9%
Gamma	169015	325	2.0×10^2	3.8×10^{-1}	99.8%

Figure 6.4: A photo taken of the mTC in its radiation shield and in its data taking position approximately 5m away from the core. Image from our paper [4]
.

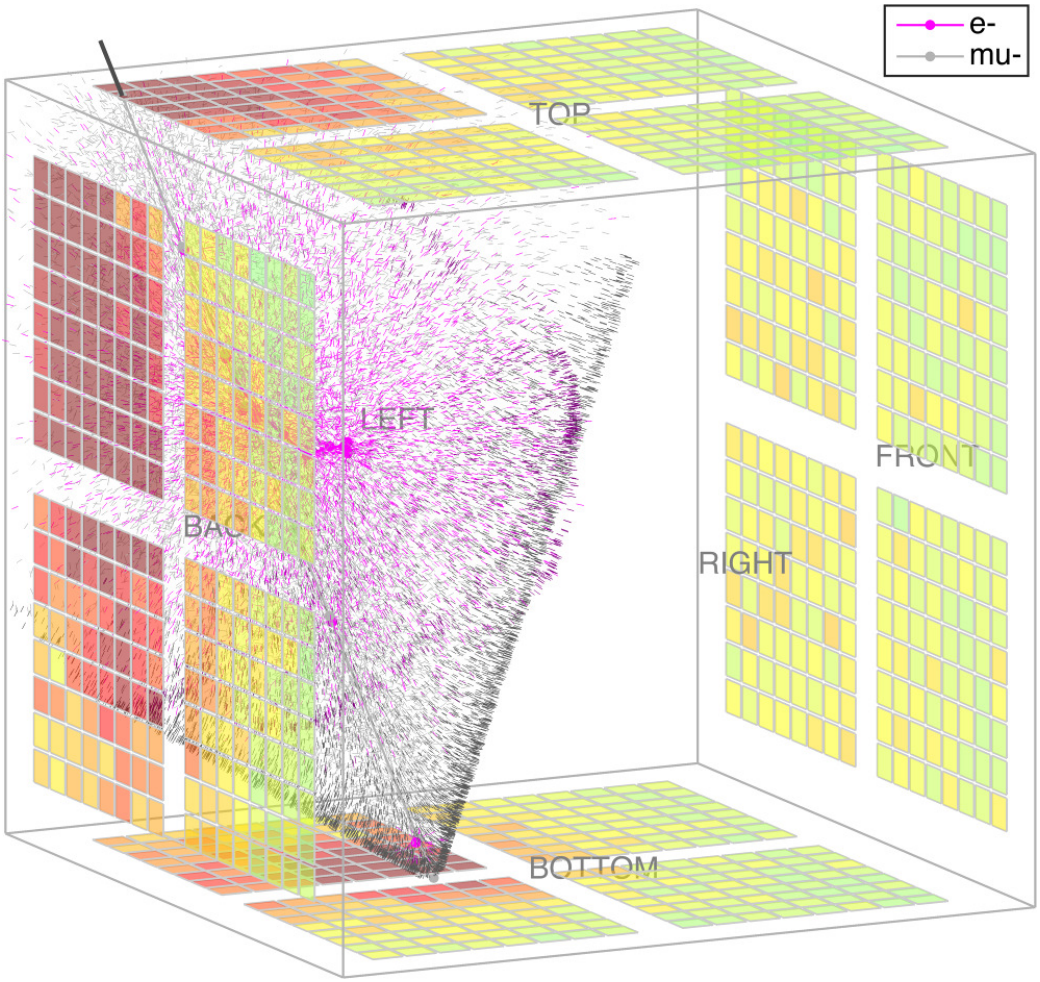

Figure 6.5: Simulated muon traversing the scintillator creating a mixture of cherenkov and scintillation light. Image from our paper [4]
.

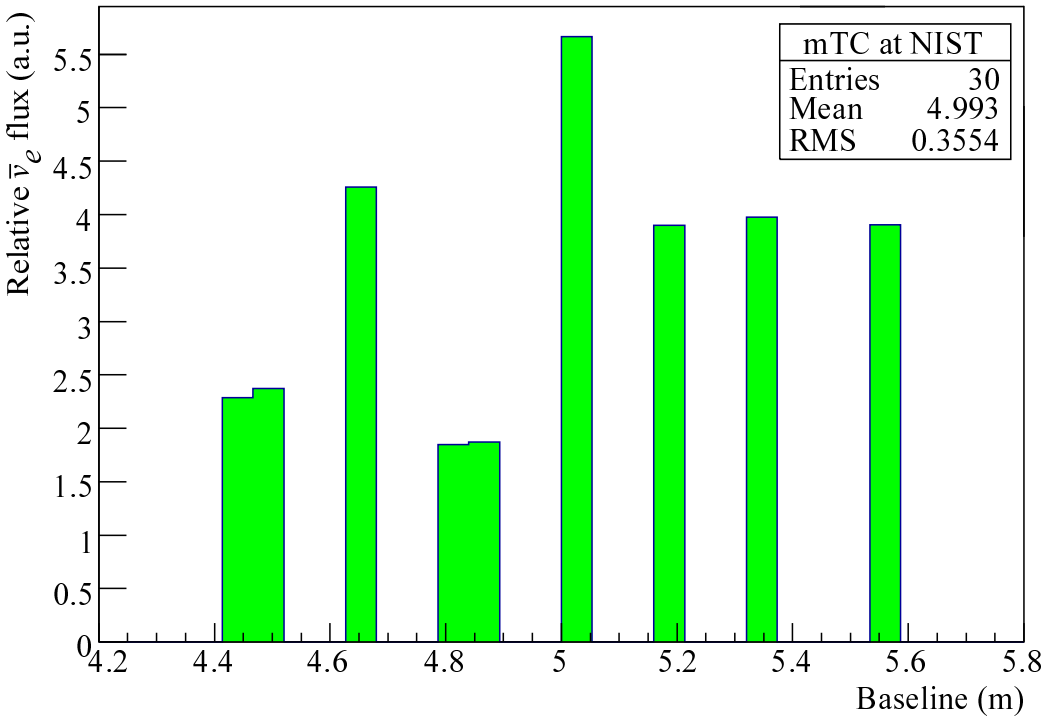

Figure 6.6: Cosmogenic isotope production yield due to sea-level spectrum muonss passing through 10 m of EJ-254 plastic. 10^4 events were simulated for this result. The number enclosed in brackets in the labels along the y-axis is the excitation energy of the isotope in units of keV. ^{9}Li and ^{8}He were not observed. Image from our paper [4].

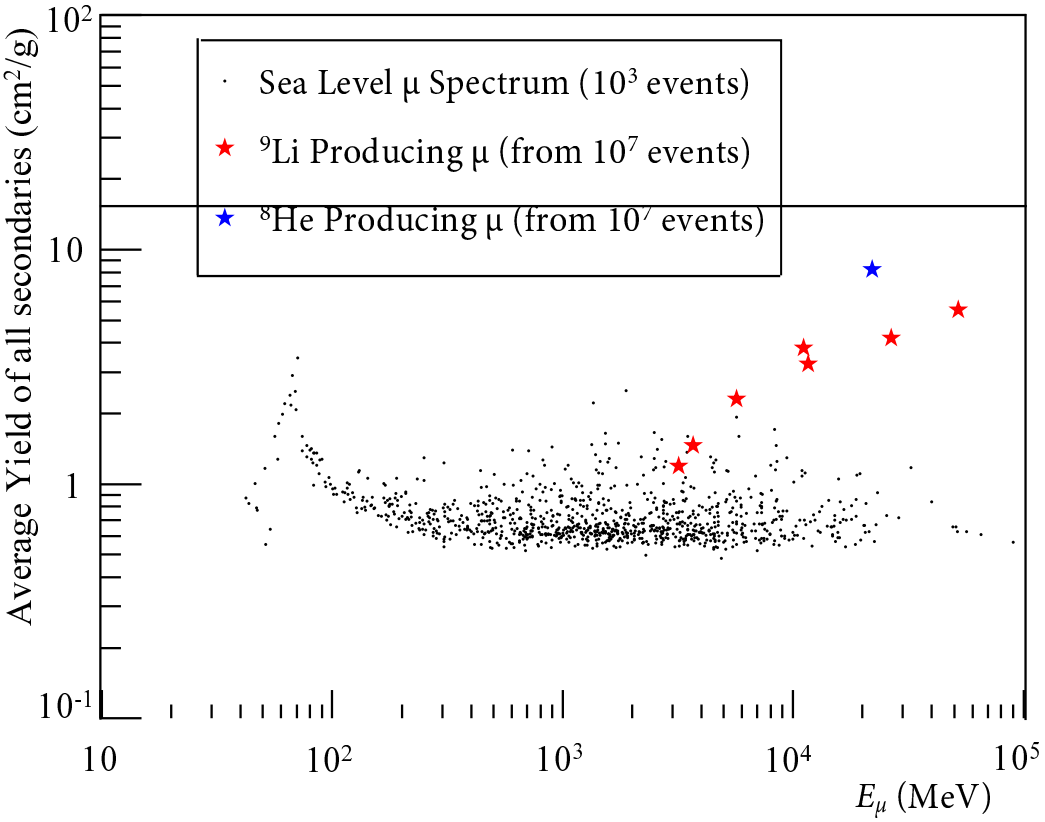

Figure 6.7: Average yield per unit muon track length per unit medium density of all non-photon secondary particles versus muon energy. The black points show the result of a run of 10^3 sea-level spectrum muons. Superimposed on the figure are eight specific muon events that had produced a ^{8}He or ^{9}Li daughter depicted by the colored stars. These eight events were extracted from a much larger ensemble with an increased statistics of 10^7 events in order to produce the rare events. Image from our paper [4].

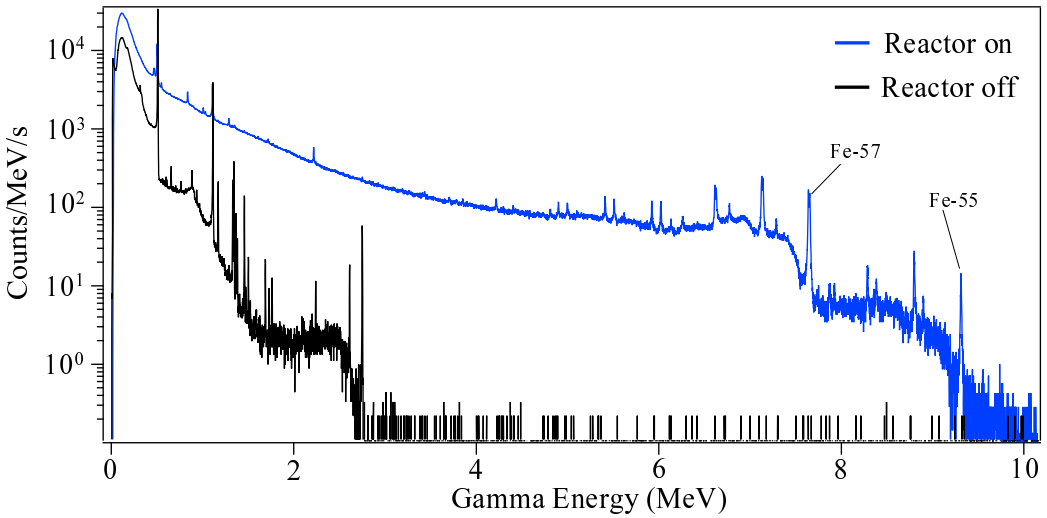

Figure 6.8: High Purity Germanium (HPGe) gamma-ray spectrometer response at the mTC location adjacent to the NIST reactor. HPGe spectrometer is 55 mm in length and 62.5 mm in diameter. The observed Fe lines are from neutron capture on surrounding shielding and structural materials. Image from our paper [4].

Chapter 7

Results from NIST and Neutron Directionality Experiments at UH Manoa

In this chapter we will discuss the results of our IBD run at the NIST NCNR. We will then discuss the results of our neutron source test that was conducted here at UH Manoa.

7.1 Run Details

The mTC collected data nearly continuously for 85 days at its position 5m from the split-core at the NCNR in the summer of 2015. During this run over a million events were recorded. Prior to this, remote operations were

set up in an impressive 6 months time frame. This enabled the personnel of this collaboration to take shifts from UH Manoa and elsewhere. Overall, we collected approximately 2400 GB of data under various conditions (reactor on/off, source testing, etc.). All the data was organized and analyzed during the fall of 2015 and the spring of 2016.

7.1.1 Reactor Background Issues

An enormous amount of data was gathered by the mTC during its short run. For some experiments this would be an advantage, however, the colossal amount of triggering the mTC experienced was a major issue, especially when considering the mTC had an expectation of approximately one event per day. An unexpected influx of gammas and neutrons were emitted from nearby experiments such as the The Multi Axis Crystal Spectrometer (MACS) and the BT-1 experiment (High Resolution Powder Diffractometer) which were running next door to our experiment. The effects on our trigger rates is shown in figure 7.1. As we can see there was a periodic interfering effect produced by the MACS experiment which greatly affected the trigger rate of our experiment.

7.1.2 Various Cuts

Various cuts to the data were made to remove invalid events which we will discuss in this section. These include removing data taken during the pre-

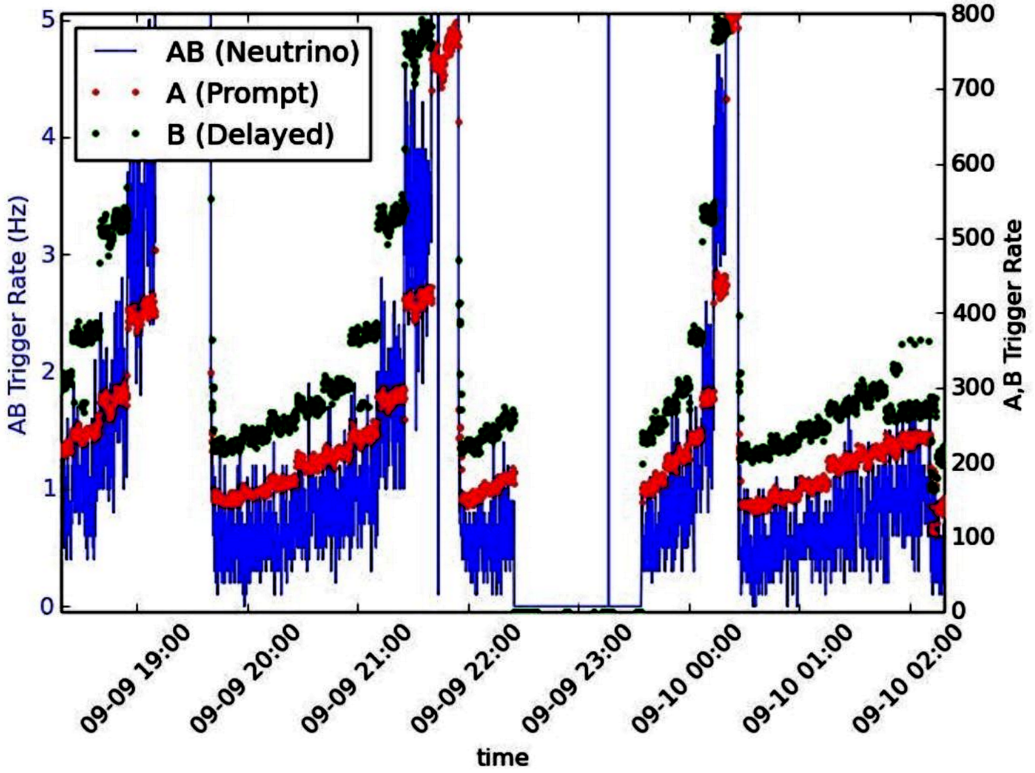

Figure 7.1: MACS Inteference
Shown here is a typical snapshot of our trigger rates while the MACS experiment was running. The unstable backgrounds helped make finding a neutrino event unmanageable.

viously discussed high background interference periods. We also removed signals that had a high rms (root mean square) with respect to timing. We believe many of these bad signals arose from the process of ion-feedback which seemed prevalent in our MCPs. An example of such an event contrasted with a good signal is given in figure 7.2.

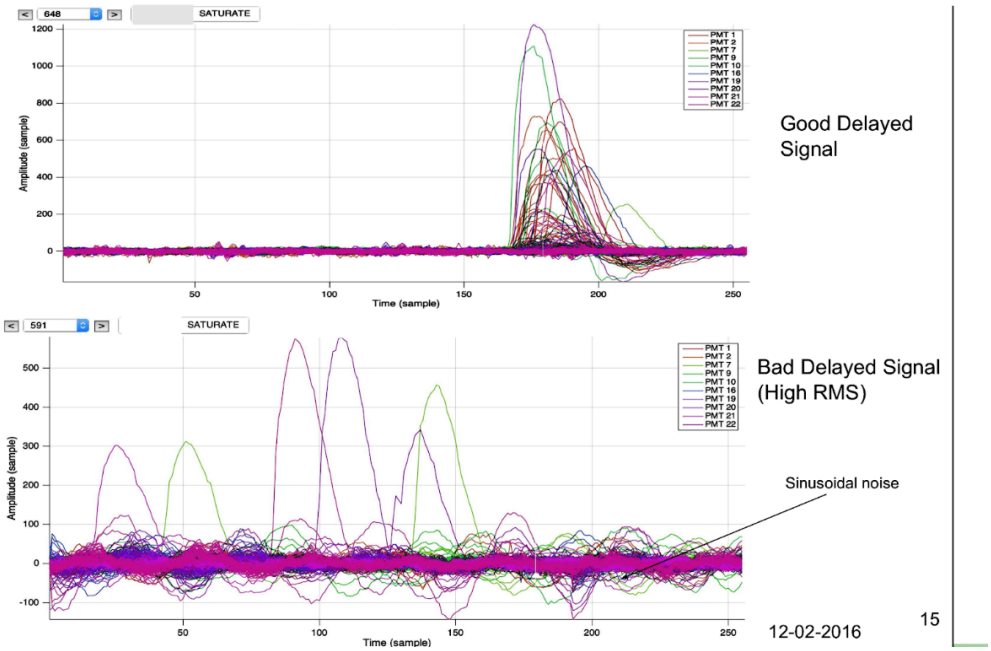

Figure 7.2: Prompt Data Taken From NIST Experiment
A good delayed signal is contrasted against a bad delayed signal. The rms for timing is clearly large in the bottom plot and a signal like this is removed as a candidate. Ion feedback is the likely the cause. Image credit [6].

7.2 Results after Cuts and Using Low Rate Only Runs

Evidently, the Macs experiment (and others) created backgrounds that helped make verifiable neutrino detection extremely difficult. After cleaning out muon events and signals plagued by high-rms values we were left with 495383 prompt and delayed events as shown in figures 7.3 and 7.4 respectively. As our experiment took approximately 60 days of total data we were expecting only 60 events. Clearly, we were having a serious background effect that was

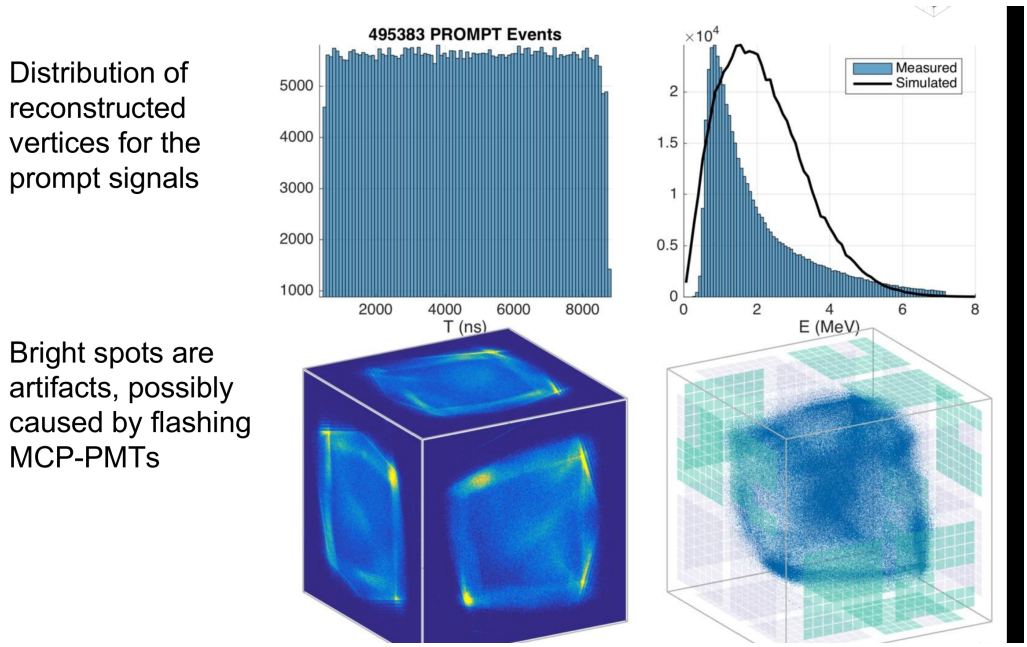

Figure 7.3: Shown here are 495383 Prompt Events from data taken at the NCNR. Bright spots are believed to be caused by flashing PMTs. Clearly there are far too many neutrino candidates for an 85 day run. Image credit [6].

affecting our trigger rates drastically. Our next task was to chart out the periods of low trigger rates during the short times where the MACS and BT-1 experiments were off. Figure 7.5 shows a plot of the mTC trigger rates when the reactor was on. A large cut from the 495383 remaining events was made by only focusing on data collected during 'quiet' periods when the neighboring experiments were not running. In fact, we learned that even when MACS and BTS-1 were 'off', only their outer shutters to the beam line were shut and not the inner shutter. Nonetheless, using the files stored during these quiet intervals we were able to analyze this lower rate data and the results are shown in figure 7.6. Unfortunately, we still were left with approximately

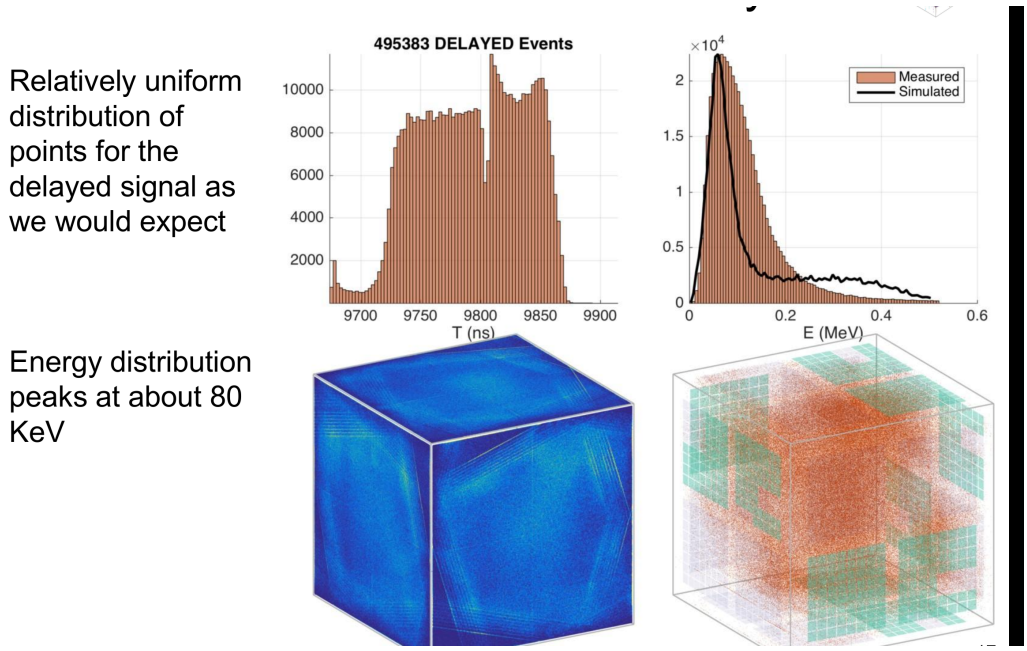

Figure 7.4: The 495383 delayed events that pair with the Prompt events in figure 7.3 Here the uniform distribution is as expected and we have an energy peak at about 80 keV as we would expect. Unfortunately, we have the larger issue of there being far too many neutrino candidates for our short 85 day run. Image credit [6].

20000 events which leaves us unable to identify a neutrino event among such a backdrop of activity. To make matters worse, the energy spectrum shows a peak around 80keV which is exactly the expected energy of the delayed event (although this is not entirely surprising as we set our triggers to seek such events). While the neighboring experiments cause many issues for our experiment, clearly the trigger level that was still too high in the 'quiet' periods. While the mTC has shown great abilities in particle imaging, the problems with the high trigger rates are a cause for concern, and since this experiment is a prototype for future detectors such as Nulat and the NTC, resolving this

issue is crucial. The reasons for these higher than expected rates are complicated and are not completely understood by our team. However, some of our recent experiments here at UH Manoa do shed some light on the issue. This will be the focus of chapter 9.

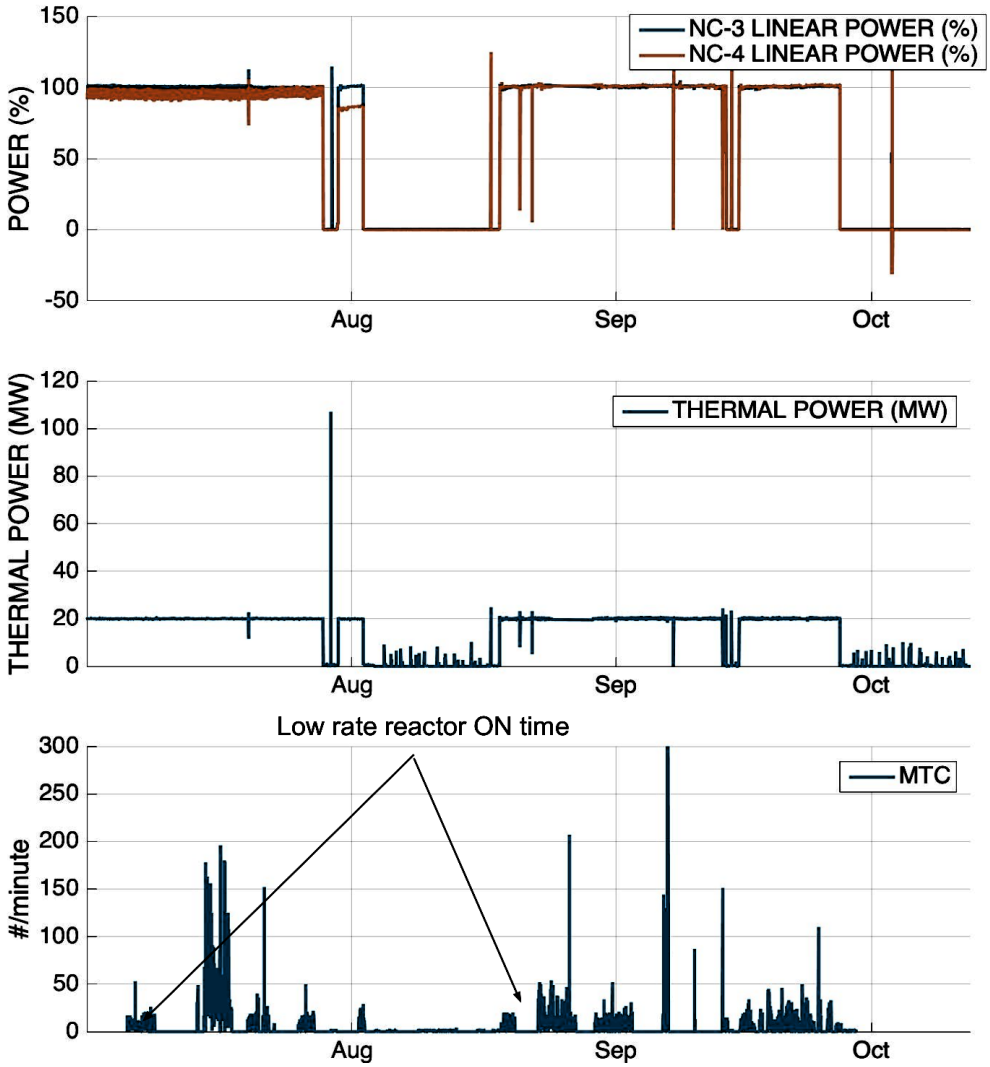

Figure 7.5: Periods of low rate activity were seldom, but careful monitoring of our trigger rates and data collection allowed us to isolate a few GBs of data for when the reactor was on and the neighboring experiments were off.

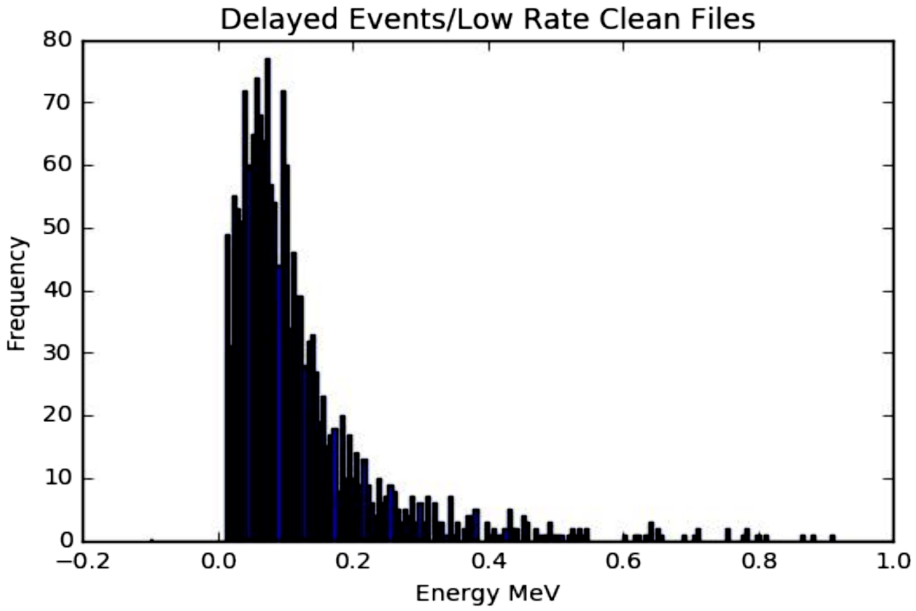

Figure 7.6: A massive cut from the 495383 delayed events was made by eliminating data taken with high backgrounds caused by neighboring experiments. Shown here is the energy spectrum of the delayed events which peaks at approximately 80 keV.

Chapter 8

Neutron Directionality Experimental Tests

After the neutrino tests at the NCNR were completed and the mTC was shipped back to UH Manoa and reassembled, we were ready to attempt neutron directionality tests using a neutron soure. We secured 1 μg of the radioactive isotope Californium (^{98}Cf). The neutron and gamma energy spectra are shown in figure 8.1 and figure 8.2 respectively [7].

While the kinetic energy of the outgoing neutrons are roughly one order larger than the energy of the gammas we are burdened by the quenching factor in our scintillator which is described by Birk's Law [54]:

$$\frac{dL}{dx} = S\frac{\frac{dE}{dx}}{1 + k_B\frac{dE}{dx}} \tag{8.1}$$

For a particle moving through a scintillator, the law describes the de-

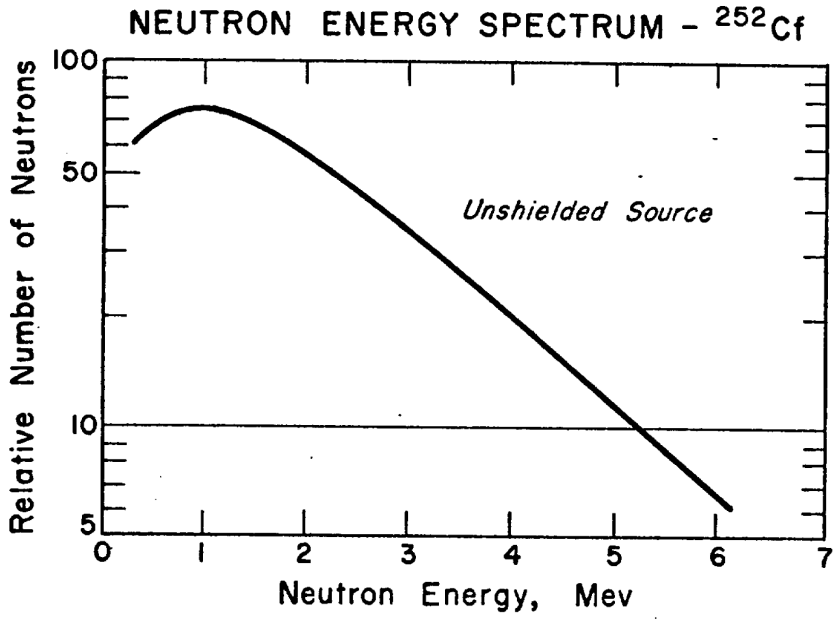

Figure 8.1: The energy spectrum for neutrons emitted from Californium showing a peak at approximately 1 MeV. Plot taken from [7]

parture from linearity for the light yield (L) per path length as a function of the energy loss per path length (k_B is approximately 0.126 mm/MeV for polystyrene-based scintillators) [55]. The linearity departure in Birk's Law presents complications in reconstructing the real energy deposited in a scintillator versus the effective energy. The overall effect of Birk's Law is that a heavier charged particle will emit less light than an electron equivalent charged particle. While Birk's law was applied in all simulations including our neutron recoil portion, accuracy in reconstructions will always be affected when the validity of its application is ambiguous. Thankfully, this loss in ac-

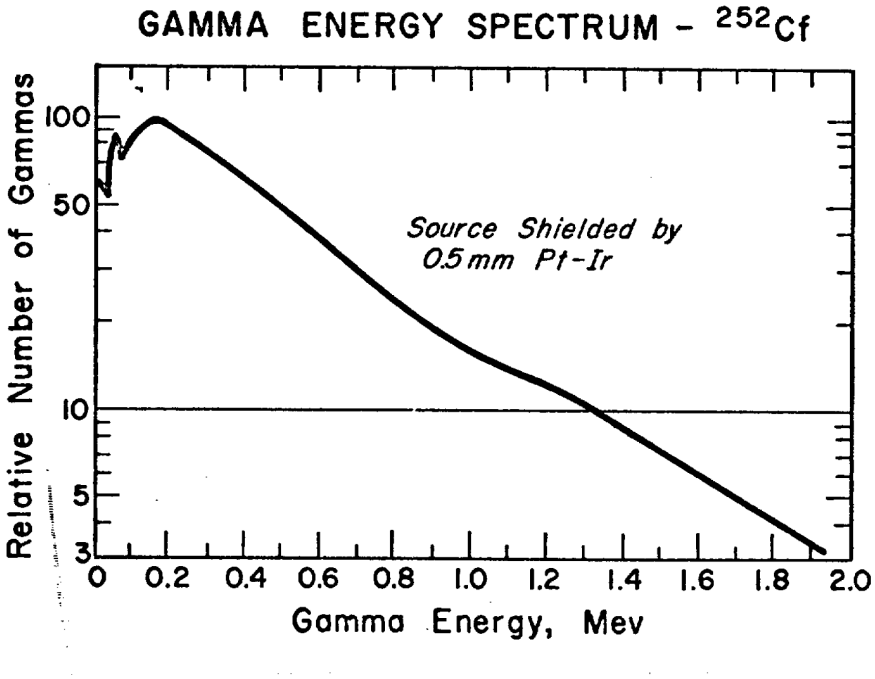

Figure 8.2: The energy spectrum for gammas emitted from Californium showing a peak at approximately .2 MeV. Plot taken from [7]

curacy can be overcome in the area of neutron directionality because our model should reject multiple recoil candidates for gammas. A consequence of Birk's Law is that a rough application of it means we need to scale the apparent energy response (the amount of electron-equivalent light produced) in our cube by about 1/10th for neutron recoils off carbon. The problem then is that the effective energy response of the scintillator for gammas and neutrons overlaps as seen in figures 8.1 and 8.2. This means that we will be relying heavily on our fitter to distinguish between the two responses, which

is an impossible task if there is only one recoil by a neutron.

The results of the californium tests failed to reveal directionality. Out of 10867 background events 128 were fit with the BIC as neutron recoil candidates, while out of 11677 californium events pointed at one face of the mTC 203 were successfully fit with the BIC. After subtracting the backgrounds our average directional vector did not match the expected direction. A test with the californium source pointed at face 5 fit 474 events out of 10900 events and the background subtracted average directional vector also did not match the expected direction. The next chapter is dedicated to discussing what problems may have contributed to produce these unfortunate results.

Chapter 9

Problems Illuminated

We need to explain the discrepancy between our excellent simulation/reconstruction results and our failed experimental results. We already discussed the background interference from nearby experiments at the NCNR, however, our analysis of the low rate periods still showed a far greater number of events then we expected for those intervals. Evidently, the background problem is not the sole issue. Fortunately, we are able to isolate some other issues that will provide some illumination.

9.1 Massive PMT Failure

During the month of June we had an unexpected failure in our cooling system while simultaneously our remote monitoring system failed. All in all, 12 of our 24 PMTs died all at once. The PMTs could not be replaced due to time and

financial issues in addition to the difficult labor job it presented. With half of our PMTs missing we lost 768 channels in an instant. Fortunately the PMTs were burnt out in a staggered pattern where there was 2 PMTs still working on each side. Nonetheless, losing half of our coverage created blind spots that lowered our particle imaging resolution significantly. The failure happened very early into our experiment and the extent of the damage the remaining PMTs endured was unknown to us at the time. However, it quickly became clear that the integrity of the PMTs was compromised as failing channels mounted and crosstalk amongst channels increased dramatically.

9.2 PMT Crosstalk

A perplexing module to module cross-talk phenomenon was discovered approximately a year before our neutrino run at NIST. Induced charges in one PMT spread to another, even to MCPs nearby that were powered off! These phantom pulses were recorded using an oscilloscope. While this phenomena was complicated to explain it was fixed by wrapping the PMT anodes in faraday cages using aluminum foil. What was unknown to our team before we took apart the mTC in Hawaii after our NIST run, was that a far more intricate type of channel to channel crosstalk was occurring within each module.

We removed one of the working Planacon PMTs from a side of the mTC and performed various tests on random channels using our precision timing

laser system. A diagram of the MCP is shown in figure 9.1. The PMT was connected to a carrier board so that the waveforms could be digitized. The laser was outputted directly into a channel and a few hundred events were recorded for several channels. For clarity we labelled the laser injected pixel the 'target' pixel and the the pulse in that cell the 'target' pulse.

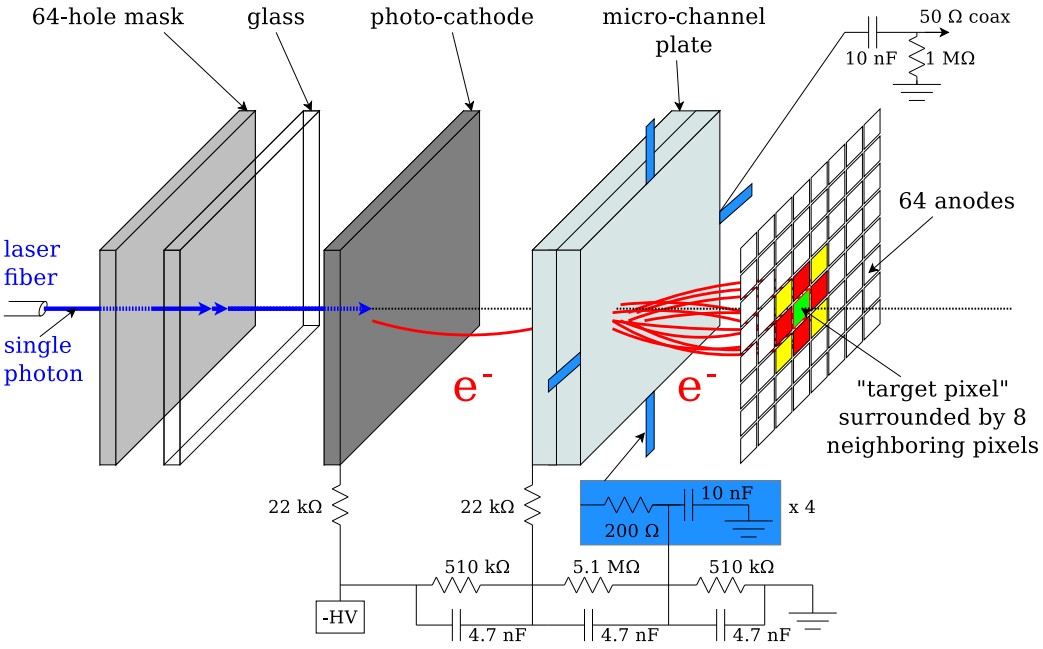

Figure 9.1: Artistic rendering of the Planacon MCPs in operation. This diagram depicts our understanding of how the large amount of cross-talk occurs via electrons being knocked off into adjacent cells. Credit to [8]
.

Figure 9.1 shows an artistic rendering of our test setup. The target pixel is shown in green and we call the the 8 surrounding pixels the 'neighbor' pixels. The neighbor pixels that form a cross (highlighted in red) around the target pixel on average experience more cross talk then corner adjacent

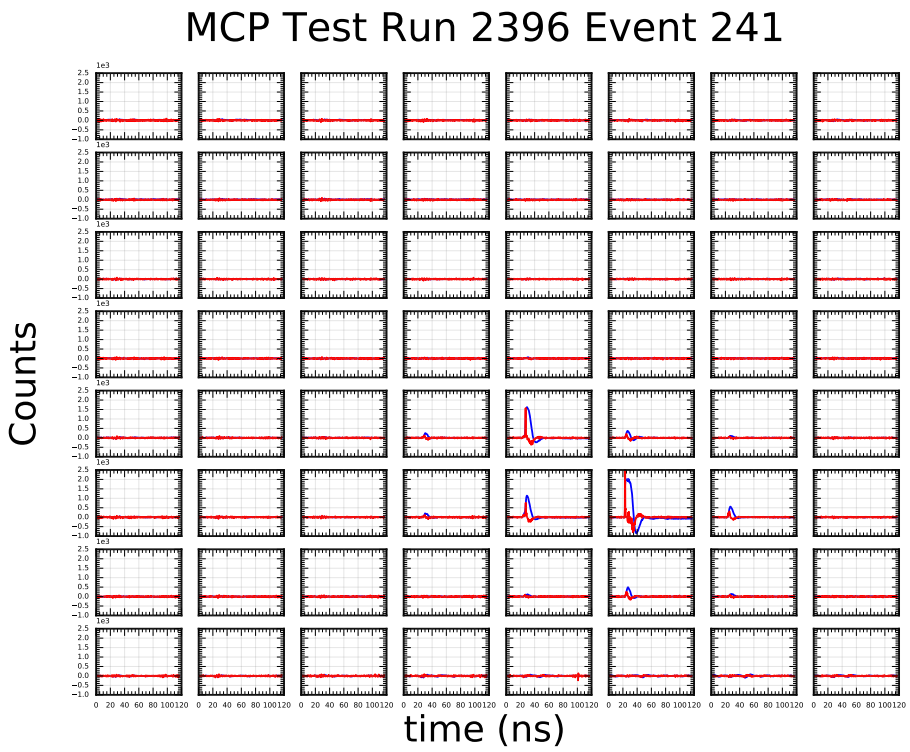

Figure 9.2: A typical MCP test event where the pixel with the largest waveform is the target pixel (the pixel that the laser pulse was injected) and the pixels around the target also show induced charge. We believe knock-off electrons pushed into neighboring cells are the cause of this. The curve in red is the calculated derivative. Credit to [9].

pixels (highlighted in yellow).

A typical event is shown here in figure 9.2. Here the laser injected pixel (target ixel) is the one showing the largest waveform in blue. The surrounding pixels exhibit cross-talk of varying degrees.

We determined that the likely culprit for this phenomena is electron knock-off into adjacent cells. We eliminated the theory of a capacitive trans-

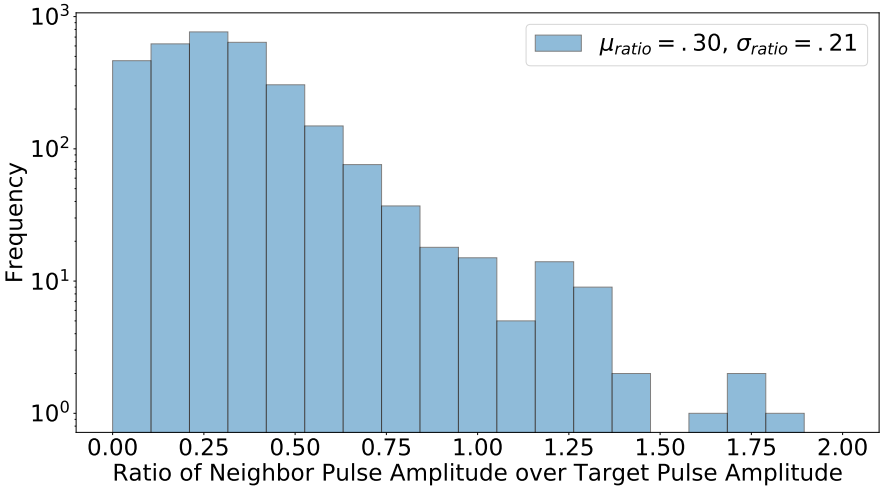

Figure 9.3: A plot of the relative amplitude ratio of an adjacent pixel over the main target pixel. For this plot we chose the pixel directly above the target pixel. The plot shows that occasionally the cross-talk can exceed the main or target pulse significantly.)

fer of energy from one cell to another due to the fact that the cross-talk pulses were clearly not proportional to the derivative of the target pulse.

So how do these new unexpected instrumental flaws factor in to our analysis? In figure 9.3 we see a plot of the relative amplitude of the neighbor pixel directly above the target pixel to the amplitude of the target pixel itself. Statistics of this ratio were recorded only when both pulses exceeded 150 ADC counts. We see that on average the cross-talk is approximately 30% of the target amplitude. Considering there are 7 other potential pixels that can simultaneously show cross-talk this is indeed significant. Clearly we were over counting photons and thereby over estimating the energy before. To correct for this we record statistics in a similar fashion to what is seen

in figure 9.3. In figure 9.4 we recorded statistics of the relative amplitude of the target amplitude to the total amplitude of the target and surrounding pixels (the 9 highlighted in figure 9.1). We found that the ratio was .575 +/- .270 and used this value to multiply our old photon counts by as a correction. The cross-talk is obviously highly inconsistent from event to event by, thereby significantly increasing our uncertainty in our energy reconstruction.

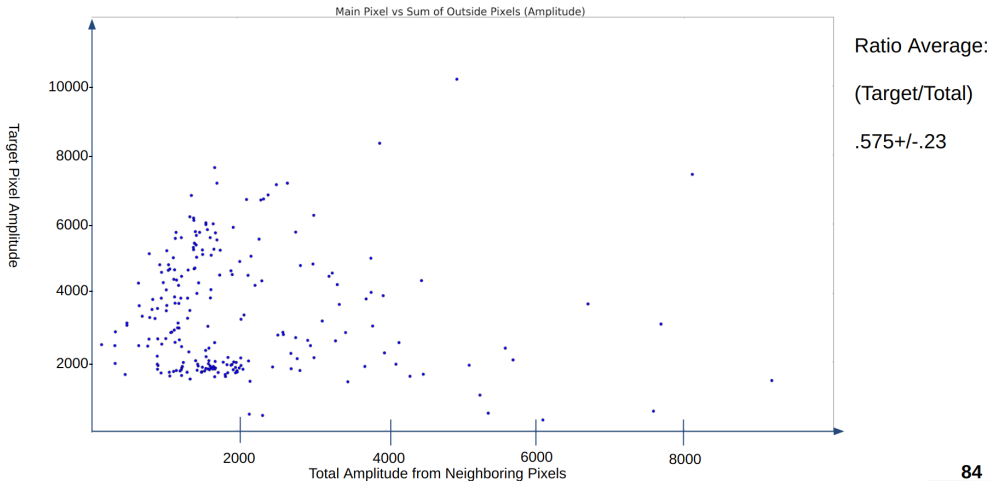

Figure 9.4: A scatter plot of the amplitude of the main pixel versus the total amplitudes of the surrounding pixels. The plot shows the wide varying response in the activity of the surrounding pixels to the charge placed in the target pixel. The ratio of the target pulse to the total amplitude of all 9 activated pixels produced a value of .575 +/- .270
.

Even more troubling are the results of figure 9.5 which is a plot of the relative time between the neighboring pulse relative and the target pulse. We find a significant delay between the target pulse and the cross-talk pulse. The mean delay is 1.76ns with a standard deviation of .70ns. This phenomenon

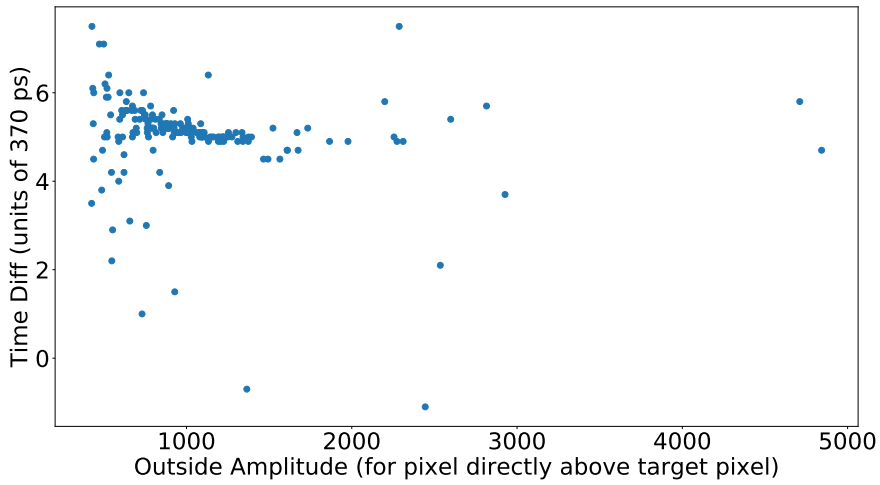

Figure 9.5: Using the same data used as in figure 9.3, we compare the relative timing between the target pulse and the adjacent pulse. We also plot the amplitude of the adjacent pixel. The average delay was 1.76ns with a standard deviation of .70ns. This is a cause of significant concern for our timing purposes.

affects our ability to accurately time-stamp events and degrades our ability to undertake neutron directionality which is an inherently time-sensitive measurement. This problem is not easily remedied by a statistically applied correction.

9.3 High Rates

An issue that is still unexplained is the higher than expected rates from the mTC. It will help the discussion if we divide the periods that tests were taken with the mTC into two categories. We will call the times that exper-

iment tests were made with the mTC before the PMT overheating incident as the 'pre-overheat period' and for the period tests were made after the incident we will refer to as the 'post-overheat period'. The high rates and erratic cross-talk (which itself will interfere with our trigger rates) became much worse during the post-overheat period. It is possible that the PMTs that survived the overheating incident acquired some structural damage, as their failure rate increased dramatically after the incident while at the same time our trigger rates were increasing. An interesting contrast was noticed early this year when we looked at newly acquired laser data and the readout from the remaining PMTs (7 remaining in working condition at this time) and the resulting fits were a stark contrast to the fits shown in figure 4.3. Whereas, the application of the BIC (neutron fitter) to the laser data in figure 4.3 (taken during the pre-overheat period) rejects multiple point fits and correctly identifies the event, application of the BIC to laser data in the post PMT overheating incident yields results that are not clean. Also, when taking backgrounds with normal triggering thresholds we would receive a trigger of around 100 Hz and this was puzzling. Worse is that these 'phantom' events of which the origin is uncertain, frequently fit for multiple recoils with our model which was not the case in the pre-overheat period. As we saw in figure 9.5, the spread in timing between the MCP crosstalk is on the order of a typical neutron double bounce and this can lead to false fits. So clearly a mixture of the cross-talk and a yet unexplained background phenomenon is affecting our trigger rates and our fit results, a phenomenon which had

always been present yet increased greatly in the post-overheat period. It was unfortunate that we did not undertake neutron directionality tests with californium earlier in the pre-overheat period.

9.4 Summary of Main Issues to Address for a Next-Gen mTC

Let us summarize the biggest areas we believe any future detector based on mTC style technology should address. While each problem we discuss affected all our experiments, some issues were more detrimental for IBD detection and some directly affected neutron directionality tests more so. We will divide the issues along these lines.

For success in anti-neutrino detection the two main issues that need addressing are better neutron capture times and a cleaner delayed signal for the IBD reaction. In fig 9.6 we see a simulated plot of the neutron capture time in a 1 percent boron doped scintillator and a 5 percent boron doped scintillator (Eljen Technology EJ-254). This is a timing histogram for thermalization to capture. We see there is a far greater likelihood of capture during our active recording window occurring in the 5 percent doped medium. If we integrate from 0 to 12 μs we capture approximately 40 percent of the neutrons for the 1 percent doped medium, and for the 5 percent medium we capture approximately twice that. In the end however, background rejection was our primary problem and not our capture metrics. The signal from boron capture was

just too weak and was impossible to distinguish from the background which was much greater than our team expected. A neutron capture signal with an energy signature in a quieter region of the spectrum is crucial for a next-gen version of the mTC.

While the neutron directional experiment is harder to have a fair discussion about since the mTC was in such poor shape at the time we did our tests, we can still discuss some definite improvements which would help the next-gen mTC be successful. The absolute main issue hurting our directional capabilities is the cross-talk and its inherent time spread that destroys the time sensitive fitting process required to track the recoils. Unfortunately, our PMTS were woefully inadequate. A method for distinguishing between gammas and neutrons that does not rely on only the model fit would be beneficial. A pulse shape discrimination (PSD) system (mostly needed to separate gammas and single neutron recoils) would help both the neutron directional ability and IBD detection of an mTC-like detector. Although PSD systems in general make a comparison between the long tail of a signal to the beginning of a signal with the total span being on the order of a microsecond. This would definitely make fast timing analysis unachievable with the technology as it stands.

Efforts such as Nulat have an important feature that is segmentation. With segmented scintillator blocks, interactions can be isolated and light mixing from cell to cell is limited. In the mTC all events, including coinci-

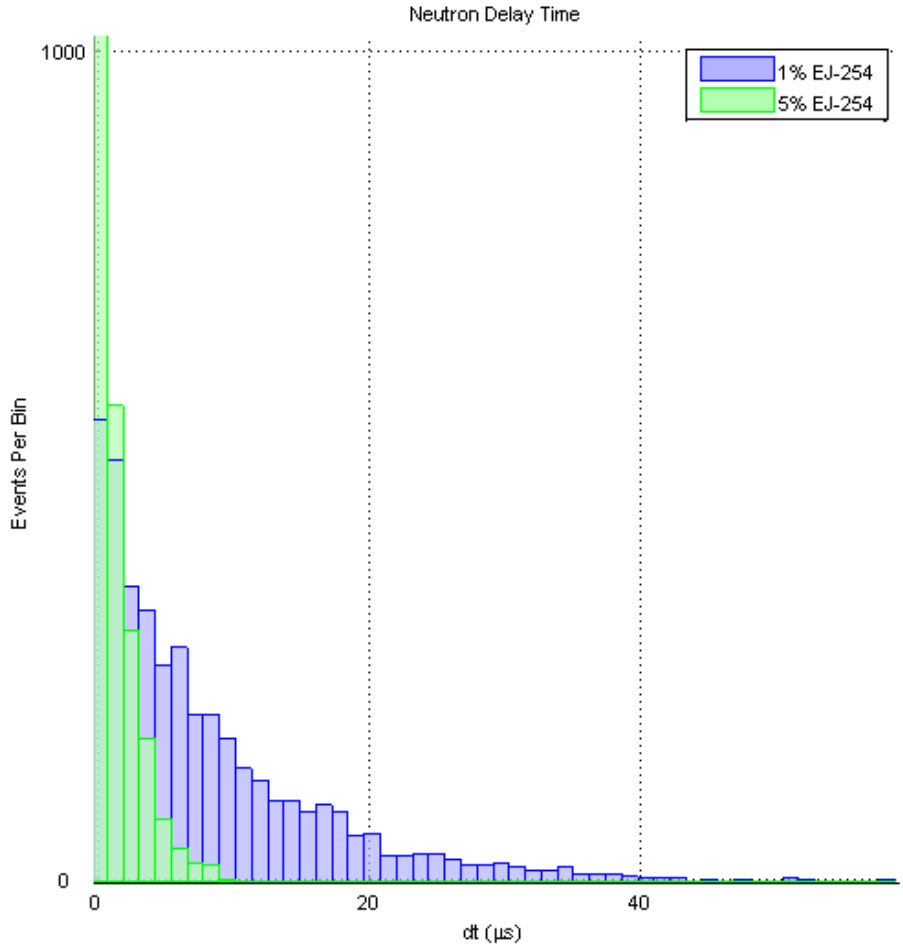

Figure 9.6: Simulation for the capture times of neutron in a 1 percent Boron doped scintillator and a 5 percent boron doped scintillator (Eljen Technology EJ-254). We see a far greater likelihood of capture during our active recording window occurring in the 5 percent doped medium. Credit to [6].

dental events will produce a light mixture that is hard to deconvolve and can only be addressed through applying a clever fitting model.

Finally, we need better shielding from backgrounds and this issue affects both of our experiments. Our group is still attempting to understand the attenuation of the cave and a paper should be published soon on the matter.

Chapter 10

Conclusion

The basic design of the mTC was received enthusiastically by the community of neutrino physicists. With continuously larger and more expensive neutrino experiments (such as DUNE) in the works a revolution in neutrino detectors is desireable. The mTC was a smaller, less expensive alternative to this trend. Of course ultimately long distance neutrino detection requires large instruments, but near reactor detectors can be small and prove out techniques for later larger applications. While the technology did not work as we had hoped, we believe that if our problems are addressed in next-gen mTC like projects (such as Nulat) the dream of having cheaper and better neutrino detectors may be within our technical grasp soon. With a cleaner delayed signal, a method for pulse shape discrimination, and actual timing/amplitude resolutions on order of what was expected, we believe we could achieve better results than our simulations had promised.

We are proud of building the very first attempt of a compact portable neutrino detector. We were the first to use compact pmt-mounted electronics other than an accelerator experiment (namely BELLE). We had the highest ever channel density (photon to waveform detection) on a neutrino target. In our neutron directionality simulations we found an angle error of 1.3 +/- 0.7 radians between our average truth and fitted neutron directional vectors, an impressive result considering neutron directionality has never been accomplished in a single solid volume. Our experiment was also elegant in it's makeup, having no huge bundle of cables and bulky electronic racks, and low power consumption. Reliable remote operation was implemented quickly and we could run our experiment smoothly from Hawaii to NIST in DC. We designed and built our own adjustable walk-in radiation cave with 1000x attenuation of neutrons and gammas. Most importantly, we set a precedent in the field with many competitors which have been directly inspired by our experiment, and have pointed our own way forward.

Bibliography

[1] D. Halliday, R. Resnick, and J. Walker. *Fundamentals of Physics Extended, 10th Edition*. Wiley, 2013.

[2] G. Danby, J-M. Gaillard, K. Goulianos, L. M. Lederman, N. Mistry, M. Schwartz, and J. Steinberger. Observation of high-energy neutrino reactions and the existence of two kinds of neutrinos. *Phys. Rev. Lett.*, 9:36–44, Jul 1962.

[3] David Griffiths. *Introduction to Elementary Particles*. WileyVCH Verlag GmbH, Weinheim, Germany, January 2008.

[4] V A Li, R Dorrill, M J Duvall, J Koblanski, S Negrashov, M Sakai, S A Wipperfurth, K Engel, G R Jocher, J G Learned, L Macchiarulo, S Matsuno, W F Mcdonough, H P Mumm, J Murillo, K Nishimura, M Rosen, S M Usman, and G S Varner. Invited article: minitimecube. *The Review of scientific instruments*, 87(2), February 2016.

[5] ELJEN. BORON LOADED EJ-254. 2016.

[6] Ultralytics Glenn Jocher.

[7] A.R. Boulogne and A.G. Evans. Californium-252 neutron sources for medical applications. *The International Journal of Applied Radiation and Isotopes*, 20(6):453 – 461, 1969.

[8] grad student Viaschlev Li and friend at UH Manoa.

[9] grad student Ryan Dorrill and friend at UH Manoa.

[10] Ernest Rutherford. Nuclear constitution of atoms. *Nature*, 105(2642):500–501, June 1920.

[11] W. Heisenberg. Über den anschaulichen Inhalt der quantentheoretischen Kinematik und Mechanik. *Zeitschrift fur Physik*, 43:172–198, March 1927.

[12] J. Chadwick. Possible Existence of a Neutron. *'Nature'*, 129:312, February 1932.

[13] W. Bothe and H. Becker. Künstliche Erregung von Kern-γ-Strahlen. *Zeitschrift fur Physik*, 66:289–306, May 1930.

[14] F.J. Curie I. Curie. mission de protons de grande vitesse par les substances hydrognes sous l'influence des rayons trs pntrants. 1932.

[15] James Byrne. *Neutrons, Nuclei and Matter: An Exploration of the Physics of Slow Neutrons*. Dover Books on Physics. Dover Publications, 2013.

[16] John L. Hubisz. Enrico fermi and the revolutions of modern physics , by dan cooper. *The Physics Teacher*, 37(6):370–370, September 1999.

[17] Luis W. Alvarez and F. Bloch. A quantitative determination of the neutron moment in absolute nuclear magnetons. *Phys. Rev.*, 57:111–122, Jan 1940.

[18] M. A. B. Bég, B. W. Lee, and A. Pais. Su(6) and electromagnetic interactions. *Phys. Rev. Lett.*, 13:650–650, Nov 1964.

[19] Peter J. Mohr, Barry N. Taylor, and David B. Newell. Codata recommended values of the fundamental physical constants: 2010. *Rev. Mod. Phys.*, 84:1527–1605, Nov 2012.

[20] D. J. Hughes and M. T. Burgy. Reflection and polarization of neutrons by magnetized mirrors. *Physical Review*, 76(9):1413–1414, November 1949.

[21] J.E. Sherwood, T.E. Stephenson, and S. Bernstein. Stern-gerlach experiment on polarized neutrons. *Physical Review Superseded in part by Phys. Rev. A, Phys. Rev. B: Solid State, Phys. Rev. C, and Phys. Rev. D*, 96, 1954.

[22] Gerald A. Miller. Charge densities of the neutron and proton. *Phys. Rev. Lett.*, 99:112001, Sep 2007.

[23] A. Serebrov, E. Kolomenskiy, A. Pirozhkov, I. Krasnoschekova, A. Vassiljev, A. Polushkin, M. Lasakov, A. Fomin, I. Shoka, V. Solovey,

O. Zherebtsov, P. Geltenbort, S. Ivanov, O. Zimmer, E. Alexandrov, S. Dmitriev, and N. Dovator. New measurements of the neutron electric dipole moment. *JETP Letters*, 99(1):4–8, March 2014.

[24] K Nakamura. Review of particle physics. *Journal of Physics G: Nuclear and Particle Physics*, 37(7A), July 2010.

[25] Fred L. Wilson. Fermi's theory of beta decay. *American Journal of Physics*, 36(12):1150–1160, 1968.

[26] K. C. Wang. A Suggestion on the Detection of the Neutrino. *Physical Review*, 61:97–97, January 1942.

[27] C. L. Cowan, F. Reines, F. B. Harrison, H. W. Kruse, and A. D. McGuire. Detection of the free neutrino: a confirmation. *Science*, 124(3212):103–104, 1956.

[28] K. Kodama et al. Observation of tau neutrino interactions. *Phys. Lett.*, B504:218–224, 2001.

[29] B. Pontecorvo. Neutrino Experiments and the Problem of Conservation of Leptonic Charge. *Sov. Phys. JETP*, 26:984–988, 1968. [Zh. Eksp. Teor. Fiz.53,1717(1967)].

[30] R. Davis, D. S. Harmer, and K. C. Hoffman. Search for Neutrinos from the Sun. *Physical Review Letters*, 20:1205–1209, May 1968.

[31] A.B. Mcdonald. Solar neutrino measurements. *Nuclear Physics B (Proceedings Supplements)*, 110:219–225, 2002.

[32] Jiajie Ling and Jiajie Daya Bay Collaboration. Observation of electron-antineutrino disappearance at daya bay. In *AIP Conference Proceedings*, volume 1560, pages 206–210. American Institute of Physics, October 2013.

[33] F. P. An, A. B. Balantekin, H. R. Band, M. Bishai, S. Blyth, D. Cao, G. F. Cao, J. Cao, Y. L. Chan, J. F. Chang, Y. Chang, H. S. Chen, Q. Y. Chen, S. M. Chen, Y. X. Chen, Y. Chen, J. Cheng, Z. K. Cheng, J. J. Cherwinka, M. C. Chu, A. Chukanov, J. P. Cummings, Y. Y. Ding, M. V. Diwan, M. Dolgareva, J. Dove, D. A. Dwyer, W. R. Edwards, R. Gill, M. Gonchar, G. H. Gong, H. Gong, M. Grassi, W. Q. Gu, L. Guo, X. H. Guo, Y. H. Guo, Z. Guo, R. W. Hackenburg, S. Hans, M. He, K. M. Heeger, Y. K. Heng, A. Higuera, Y. B. Hsiung, B. Z. Hu, T. Hu, E. C. Huang, H. X. Huang, X. T. Huang, Y. B. Huang, P. Huber, W. Huo, G. Hussain, D. E. Jaffe, K. L. Jen, X. P. Ji, X. L. Ji, J. B. Jiao, R. A. Johnson, D. Jones, L. Kang, S. H. Kettell, A. Khan, S. Kohn, M. Kramer, K. K. Kwan, M. W. Kwok, T. J. Langford, K. Lau, L. Lebanowski, J. Lee, J. H. C. Lee, R. T. Lei, R. Leitner, J. K. C. Leung, C. Li, D. J. Li, F. Li, G. S. Li, Q. J. Li, S. Li, S. C. Li, W. D. Li, X. N. Li, X. Q. Li, Y. F. Li, Z. B. Li, H. Liang, C. J. Lin, G. L. Lin, S. Lin, S. K. Lin, Y. C. Lin, J. J. Ling, J. M. Link, L. Littenberg, B. R. Littlejohn,

J. L. Liu, J. C. Liu, C. W. Loh, C. Lu, H. Q. Lu, J. S. Lu, K. B. Luk, X. Y. Ma, X. B. Ma, Y. Q. Ma, Y. Malyshkin, D. A. Martinez Caicedo, K. T. McDonald, R. D. McKeown, I. Mitchell, Y. Nakajima, J. Napolitano, D. Naumov, E. Naumova, H. Y. Ngai, J. P. Ochoa-Ricoux, A. Olshevskiy, H. R. Pan, J. Park, S. Patton, V. Pec, J. C. Peng, L. Pinsky, C. S. J. Pun, F. Z. Qi, M. Qi, X. Qian, R. M. Qiu, N. Raper, J. Ren, R. Rosero, B. Roskovec, X. C. Ruan, H. Steiner, P. Stoler, J. L. Sun, W. Tang, D. Taychenachev, K. Treskov, K. V. Tsang, C. E. Tull, N. Viaux, B. Viren, V. Vorobel, C. H. Wang, M. Wang, N. Y. Wang, R. G. Wang, W. Wang, X. Wang, Y. F. Wang, Z. Wang, Z. Wang, Z. M. Wang, H. Y. Wei, L. J. Wen, K. Whisnant, C. G. White, L. Whitehead, T. Wise, H. L. H. Wong, S. C. F. Wong, E. Worcester, C.-H. Wu, Q. Wu, W. J. Wu, D. M. Xia, J. K. Xia, Z. Z. Xing, J. L. Xu, Y. Xu, T. Xue, C. G. Yang, H. Yang, L. Yang, M. S. Yang, M. T. Yang, Y. Z. Yang, M. Ye, Z. Ye, M. Yeh, B. L. Young, Z. Y. Yu, S. Zeng, L. Zhan, C. Zhang, C. C. Zhang, H. H. Zhang, J. W. Zhang, Q. M. Zhang, R. Zhang, X. T. Zhang, Y. M. Zhang, Y. X. Zhang, Y. M. Zhang, Z. J. Zhang, Z. Y. Zhang, Z. P. Zhang, J. Zhao, L. Zhou, H. L. Zhuang, and J. H. Zou. Evolution of the reactor antineutrino flux and spectrum at daya bay. *Phys. Rev. Lett.*, 118:251801, Jun 2017.

[34] John G. Learned. KamLand internal memo. 2009.

[35] H. Watanabe. Neutrino Geoscience Italy. 2010.

[36] John G. Learned. High Energy Neutrino Physics with Liquid Scintillation Detectors. 2009.

[37] C. Lane et al. A new type of Neutrino Detector for Sterile Neutrino Search at Nuclear Reactors and Nuclear Nonproliferation Applications. 2015.

[38] PHOTONIS. PLANACON XP85012 data sheet. 2017.

[39] G. Varner, L. Ruckman, and A. Wong. The first version buffered large analog bandwidth (blab1) asic for high luminosity collider and extensive radio neutrino detectors. *Nuclear Instruments and Methods in Physics Research Section A: Accelerators, Spectrometers, Detectors and Associated Equipment*, 591(3):534 – 545, 2008.

[40] K. Bechtol, S. Funk, A. Okumura, L.L. Ruckman, A. Simons, H. Tajima, J. Vandenbroucke, and G.S. Varner. Target: A multi-channel digitizer chip for very-high-energy gamma-ray telescopes. *Astroparticle Physics*, 36(1):156 – 165, 2012.

[41] Timothy Miller, Robert Schaefer, and H. Brian Sequeira. Pride (passive radio [frequency] ice depth experiment): An instrument to passively measure ice depth from a europan orbiter using neutrinos. *Icarus*, 220(2):877 – 888, 2012.

[42] B. Dey, M. Borsato, N. Arnaud, D.W.G.S. Leith, K. Nishimura, D.A. Roberts, B.N. Ratcliff, G. Varner, and J. Vavra. Design and performance

of the focusing {DIRC} detector. *Nuclear Instruments and Methods in Physics Research Section A: Accelerators, Spectrometers, Detectors and Associated Equipment*, 775:112 – 131, 2015.

[43] K.A. Olive and Particle Data Group. Review of particle physics. *Chinese Physics C*, 38(9):090001, 2014.

[44] F. Ardellier et al. Double Chooz: A Search for the neutrino mixing angle theta(13). 2006.

[45] Miles V. Klein. Optics, 1986.

[46] D. Wackerly, W. Mendenhall, and R.L. Scheaffer. *Mathematical Statistics with Applications*. Cengage Learning, 2014.

[47] William Mendenhall. Mathematical statistics with applications, 1986.

[48] *Bayesian Information Criteria*. Springer New York, New York, NY, 2008.

[49] G.F. Knoll. *Radiation Detection and Measurement*. John Wiley & Sons, 2010.

[50] I.A. Paweczak, A.M. Glenn, H.P. Martinez, M.L. Carman, N.P. Zaitseva, and S.A. Payne. Boron-loaded plastic scintillator with neutron- pulse shape discrimination capability. *Nuclear Instruments and Methods in Physics Research Section A: Accelerators, Spectrometers, Detectors and Associated Equipment*, 751(Supplement C):62 – 69, 2014.

[51] Alex Wright, Pablo Mosteiro, Ben Loer, and Frank Calaprice. A highly efficient neutron veto for dark matter experiments. *Nuclear Instruments and Methods in Physics Research Section A: Accelerators, Spectrometers, Detectors and Associated Equipment*, 644(1):18 – 26, 2011.

[52] P. Vogel and J. F. Beacom. Angular distribution of neutron inverse beta decay, $\overline{\nu}_e + \vec{p} \; e^+ + n$. *Phys. Rev. D*, 60:053003, Jul 1999.

[53] J. Ashenfelter, B. Balantekin, C.X. Baldenegro, H.R. Band, G. Barclay, C.D. Bass, D. Berish, N.S. Bowden, C.D. Bryan, J.J. Cherwinka, R. Chu, T. Classen, D. Davee, D. Dean, G. Deichert, M.J. Dolinski, J. Dolph, D.A. Dwyer, S. Fan, J.K. Gaison, A. Galindo-Uribarri, K. Gilje, A. Glenn, M. Green, K. Han, S. Hans, K.M. Heeger, B. Heffron, D.E. Jaffe, S. Kettell, T.J. Langford, B.R. Littlejohn, D. Martinez, R.D. McKeown, S. Morrell, P.E. Mueller, H.P. Mumm, J. Napolitano, D. Norcini, D. Pushin, E. Romero, R. Rosero, L. Saldana, B.S. Seilhan, R. Sharma, N.T. Stemen, P.T. Surukuchi, S.J. Thompson, R.L. Varner, W. Wang, S.M. Watson, B. White, C. White, J. Wilhelmi, C. Williams, T. Wise, H. Yao, M. Yeh, Y.-R. Yen, C. Zhang, and X. Zhang. Background radiation measurements at high power research reactors. *Nuclear Instruments and Methods in Physics Research Section A: Accelerators, Spectrometers, Detectors and Associated Equipment*, 806:401 – 419, 2016.

[54] J B Birks. Scintillations from organic crystals: Specific fluorescence

and relative response to different radiations. *Proceedings of the Physical Society. Section A*, 64(10):874, 1951.

[55] B. D. Leverington, M. Anelli, P. Campana, and R. Rosellini. A 1 mm Scintillating Fibre Tracker Readout by a Multi-anode Photomultiplier. 2011.